Field Evaluation of Interlayer-Reinforced Asphalt Overlay Performance

NCDOT Project 2021-07
FHWA/NC/2021-07
June 2024

Y. Richard Kim, Ph.D., P.E., F. ASCE. et al.
Department of Civil, Construction, &
Environmental Engineering
North Carolina State University

RESEARCH &
DEVELOPMENT

Field Evaluation of Interlayer-Reinforced Asphalt Overlay Performance

FINAL REPORT

Submitted to:
North Carolina Department of Transportation
Office of Research
(Research Project No. RP2021-07)

Submitted by

Y. Richard Kim, Ph.D., P.E., F.ASCE
Jimmy D. Clark Distinguished University Professor
Campus Box 7908
Department of Civil, Construction & Environmental Engineering
North Carolina State University
Raleigh, NC 27695-7908
Tel: 919-515-7758, Fax: 919-515-7908
kim@ncsu.edu

Nithin Sudarsanan, Ph. D.
Research Associate

Department of Civil, Construction & Environmental Engineering
North Carolina State University
Raleigh, NC

June 2024

Technical Report Documentation Page

1. Report No. FHWA/NC/2021-07	2. Government Accession No.	3. Recipient's Catalog No.
4. Title and Subtitle Field Evaluation of Interlayer-Reinforced Asphalt Overlay Performance		5. Report Date June 2024 6. Performing Organization Code
7. Author(s) Y. Richard Kim, Nithin Sudarsanan		8. Performing Organization Report No.
9. Performing Organization Name and Address Campus Box 7908, Dept. of Civil, Construction, & Environmental Engrg. NCSU, Raleigh, NC 27695-7908		10. Work Unit No. (TRAIS) 11. Contract or Grant No.
12. Sponsoring Agency Name and Address NC Department of Transportation Research and Development 1549 Mail Service Center Raleigh, NC 27699-1549		13. Type of Report and Period Covered Final Report August 2018– March 2024 14. Sponsoring Agency Code RP2021-07
15. Supplementary Notes		

16. Abstract

Reflective cracking remains a significant challenge in asphalt overlays, leading to premature pavement failure. The previous study, RP 2019-19, successfully ranked geosynthetic materials in mitigating reflective cracking based on laboratory performance. The primary objective of this study is to evaluate the field performance of geosynthetic interlayers and compare the field performance against laboratory test results. Research efforts to accomplish this objective resulted in a step-by-step procedure for predicting life of geosynthetic-reinforced pavements under real-life conditions using existing pavement condition data, such as falling weight deflectometer (FWD) and crack survey data. Several methodologies were developed to support this prediction procedure, including:

- laboratory measurement of crack resistance of geosynthetic-reinforced asphalt beam specimens using the four-point bending notched beam fatigue test,
- determination of dynamic modulus of damaged asphalt layers in existing pavements,
- prediction of tensile strain at the bottom of asphalt overlay using simulated FWD deflection parameters, and
- prediction of damage index for the traffic and environmental conditions of the project in question.

The developed procedure was calibrated using Pavement Management System data from five routes selected among NCDOT's interlayer projects. The calibrated procedure was verified using the pavement design and condition survey data from the US 1 sections at Moore County near Aberdeen.

The findings from this study contribute to the prediction of field-verified performance of pavements reinforced with different geosynthetic products under realistic loading and environmental conditions. Life-cycle cost analysis using the predicted performance allows the selection of proper geosynthetic products for a given project. These results will support NCDOT engineers in making informed decisions for pavement maintenance applications, thereby enhancing the durability and cost-effectiveness of asphalt overlays in North Carolina.

17. Keywords Geosynthetics, tack coat, overlay, reflective cracking, debonding, bond strength, shear strength, tensile strain, digital image correlation (DIC), FlexPAVE™, EverStressFE, falling weight deflectometer (FWD), deflection basin parameter	18. Distribution Statement		
19. Security Classif. (of this report) Unclassified	20. Security Classif. (of this page) Unclassified	21. No. of Pages 154	22. Price

Form DOT F 1700.7 (8-72) **Reproduction of completed page authorized**

DISCLAIMER

ACKNOWLEDGEMENTS

This research was sponsored by the North Carolina Department of Transportation. The Steering and Implementation Committee was comprised of Shihai Zhang, P.E. (Chair); Josh Holland, PE.; Wiley Jones, P.E.; Clark Morrison, Ph.D., PE.; James B. Phillips, P.E.; Andrew D. Wargo, Ph.D., PE.; Todd W. Whittington, P.E.; Randy Finger; Doug McNeal; and Mustan Kadibhai, P.E. These advisors have given invaluable direction and support to the North Carolina State University research team throughout the project.

TABLE OF CONTENTS

LIST OF FIGURES

LIST OF TABLES

Chapter 1. Introduction

1.1 Background

Asphalt concrete (AC) overlays are a common, quick, and reliable method for treating pavement distress. However, the phenomenon of crack propagation through a new overlay from the underlying pavement structure, known as reflective cracking, presents significant challenges. Geosynthetic products are increasingly being used to mitigate reflective cracking due to their ease of installation, low cost, and wide availability. The primary functions of geosynthetics include reinforcement, stress relief, and waterproofing.

The reinforcing function requires geosynthetic material with a significantly higher modulus value than the surrounding asphalt. This reinforcement redirects cracking at the interlayer, thereby delaying or mitigating reflective cracking indefinitely. Stress-relieving geosynthetic products have low stiffness values, allowing them to store strain at low-stress levels. When a crack penetrates through the overlay, the geosynthetic acts as a barrier to prevent water infiltration, thus protecting the underlying structure. A geosynthetic product impregnated by the tack coat significantly reduces water permeability. Achieving the primary geosynthetic functions requires proper installation, control of the overlay thickness, and oversight of the compaction quality.

Ensuring a proper bond between adjacent asphalt layers is crucial for solid pavement performance. A weak bond between the layers and the geosynthetic product leads to premature failure due to debonding and reduces the service life of the asphalt pavement. Therefore, proper selection criteria are needed for geosynthetic products to meet varying pavement conditions. Although numerous types of geosynthetic products are available, limited studies have established selection guidelines based on field conditions. The primary goal of each product is to control reflective cracking and improve pavement longevity.

Recognizing the importance of geosynthetic interlay systems in mitigating reflective cracking in asphalt overlays, NCDOT has funded three research projects. Findings from these three projects are summarized below.

1. **NCDOT HWY-2012-02:** Both laboratory and field studies were undertaken in this project to investigate the ability of geosynthetic interlayer products to mitigate reflective cracking. A flexible pavement section of US 1 in Moore County was selected for field trials that incorporated various geosynthetic products, a chip seal, and a control segment. Cores obtained from the field pavements and laboratory-fabricated specimens were tested using direct shear tests. Also, four-point bending notched beam fatigue tests (NBFTs) were conducted on laboratory-fabricated beam specimens with geosynthetic reinforcement. The results demonstrated the benefits of geosynthetics in mitigating reflective cracking, only if the bond between the geosynthetic product and surrounding AC was strong enough to resist shear stress at the layer interface.

2. **NCDOT HWY-2013-04:** A computational and experimental methodology was developed in this project to determine shear failure in asphalt overlays reinforced by interlayer systems. The findings were used to develop shear strength threshold values applicable for accepting or rejecting asphalt overlays reinforced by interlayer systems.

3. **NCDOT RP 2019-19:** Guidelines for selecting geosynthetic pavement interlayer products and tack coats, based on six predictive models, were developed in this project. The six models were used respectively to estimate fatigue life, tensile strain, temperature-corrected falling weight deflectometer (FWD) deflections, interface shear strength (ISS), bitumen bond strength (BBS), and maximum shear ratio (MSR) versus BBS relationship as functions of various parameters to ensure the optimal performance and reliability of the reinforced asphalt overlays.

Although findings from these projects significantly improve the NCDOT's ability to determine the benefits of geosynthetic-reinforced asphalt specimens in the laboratory setting, additional research was needed to enable NCDOT engineers to select appropriate geosynthetic pavement interlayer products based on field-verified performance data. This report documents the findings from such a study.

1.2 Research Objective and Scope

The primary objective of this research is to develop a field-calibrated and verified performance prediction procedure for asphalt overlays reinforced with different geosynthetic interlayer systems. This objective is accomplished by incorporating field data, additional laboratory tests, and mechanistic models to the data from the previous NCDOT research projects.

The NCSU research team evaluated five geosynthetic products referred to as paving composite #1 (PC#1), paving composite #2 (PC#2), paving grid (PaG), paving mat (PM), and paving fabric (PF). Additionally, the study considers geosynthetic applications for asphalt overlays over damaged AC pavements, with geosynthetic systems placed about one-third from the bottom of the asphalt overlay.

Double-layered geosynthetic-reinforced and unreinforced specimens were fabricated using a slab compactor. The AC mixture used, classified as RS9.5C with 40% reclaimed asphalt pavement (RAP), was sandwiched between the layers with a tack coat (PG 64-22) applied at the manufacturer's recommended rates.

1.3 Research Approach

Specific work elements that were conducted in the project include:

- laboratory measurement of crack resistance capacity of geosynthetic-reinforced asphalt beam specimens using the four-point bending notched beam fatigue test,
- determination of dynamic modulus of damaged asphalt layers in existing pavements,
- prediction of tensile strain at the bottom of asphalt overlay using simulated FWD deflection parameters,
- prediction of damage index for the traffic and environmental conditions of the project in question,
- development of a comprehensive procedure for performance prediction of geosynthetic-reinforced asphalt pavements using site-specific conditions,
- calibration of the developed procedure using Pavement Management System (PMS) data, and

- verification of the calibrated procedure using the pavement design and condition survey data from the US 1 sections at Moore County near Aberdeen.

Figure 1-1 presents a flow chart of the research approach taken to develop a comprehensive procedure for predicting the performance of geosynthetic-reinforced pavements based on project site conditions. The outcomes of this research approach can be used to select proper geosynthetic interlayer products for a specific project. Field calibration factors that correlate laboratory and field performance of reinforced pavements are determined, aided by the field performance data of different reinforcement types. The five-phase research effort to develop the performance prediction procedure for geosynthetic-reinforced pavements is described briefly below.

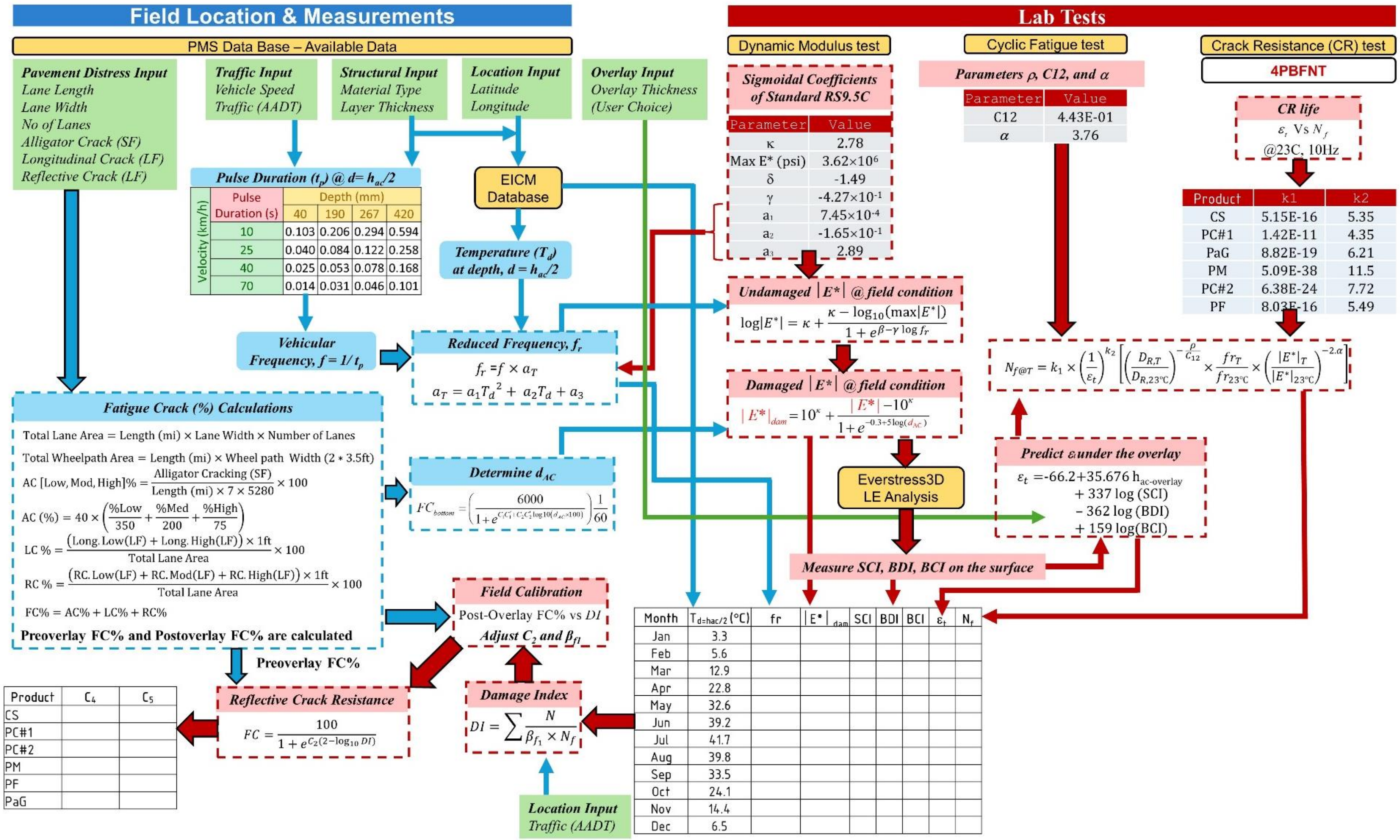

Pulse Duration (s)	40	190	267	420
Velocity (km/h) 10	0.103	0.206	0.294	0.594
25	0.040	0.084	0.122	0.258
40	0.025	0.053	0.078	0.168
70	0.014	0.031	0.046	0.101

Parameter	Value
κ	2.78
Max E* (psi)	3.62×10^6
δ	-1.49
γ	-4.27×10^{-1}
a_1	7.45×10^{-4}
a_2	-1.65×10^{-1}
a_3	2.89

Parameter	Value
C12	4.43E-01
α	3.76

Product	k1	k2
CS	5.15E-16	5.35
PC#1	1.42E-11	4.35
PaG	8.82E-19	6.21
PM	5.09E-38	11.5
PC#2	6.38E-24	7.72
PF	8.03E-16	5.49

$$f_r = f \times a_T$$
$$a_T = a_1 T_d^2 + a_2 T_d + a_3$$
$$\log|E^*| = \kappa + \frac{\kappa - \log_{10}(\max|E^*|)}{1+e^{\beta-\gamma \log f_r}}$$
$$|E^*|_{dam} = 10^{\kappa} + \frac{|E^*| - 10^{\kappa}}{1+e^{-0.3+5\log(d_{AC})}}$$
$$N_{f@T} = k_1 \times \left(\frac{1}{\varepsilon_t}\right)^{k_2}\left[\left(\frac{D_{R,T}}{D_{R,23°C}}\right)^{-\frac{\rho}{C_{12}}} \times \frac{fr_T}{fr_{23°C}} \times \left(\frac{|E^*|_T}{|E^*|_{23°C}}\right)^{-2\cdot\alpha}\right]$$
$$\varepsilon_t = -66.2 + 35.676\, h_{ac\text{-}overlay} + 337\log(SCI) - 362\log(BDI) + 159\log(BCI)$$

Total Lane Area = Length (mi) × Lane Width × Number of Lanes

Total Wheelpath Area = Length (mi) × Wheel path Width (2 * 3.5ft)

$$AC\,[\text{Low, Mod, High}]\% = \frac{\text{Alligator Cracking (SF)}}{\text{Length (mi)} \times 7 \times 5280} \times 100$$
$$AC\,(\%) = 40 \times \left(\frac{\%Low}{350} + \frac{\%Med}{200} + \frac{\%High}{75}\right)$$
$$LC\,\% = \frac{(\text{Long.Low(LF)} + \text{Long.High(LF)}) \times 1\text{ft}}{\text{Total Lane Area}} \times 100$$
$$RC\,\% = \frac{(\text{RC.Low(LF)} + \text{RC.Mod(LF)} + \text{RC.High(LF)}) \times 1\text{ft}}{\text{Total Lane Area}} \times 100$$

FC% = AC% + LC% + RC%

$$FC_{bottom} = \left(\frac{6000}{1+e^{C_1C_1'+C_2C_2'\log 10(d_{AC}\times 100)}}\right)\frac{1}{60}$$
$$DI = \sum \frac{N}{\beta_{f_1} \times N_f}$$
$$FC = \frac{100}{1+e^{C_2(2-\log_{10} DI)}}$$

Product	C_4	C_5
CS		
PC#1		
PC#2		
PM		
PF		
PaG		

Month	$T_{d=hac/2}$ (°C)	fr	$\|E^*\|_{dam}$	SCI	BDI	BCI	ε_t	N_f
Jan	3.3							
Feb	5.6							
Mar	12.9							
Apr	22.8							
May	32.6							
Jun	39.2							
Jul	41.7							
Aug	39.8							
Sep	33.5							
Oct	24.1							
Nov	14.4							
Dec	6.5							

Figure 1-1. Flow chart of research approach taken to develop and predict the field performance of geosynthetic-reinforced pavements.

Phase 1: Evaluation of Current Field Conditions Based on Pavement Management System Data

In this initial phase, the current conditions of pavements are assessed using PMS data. This evaluation provides a baseline understanding of existing pavement performance, distress types, and severity levels. The collected data are crucial for investigating the effectiveness of geosynthetic interlayers in mitigating reflective cracking and for setting up the field data for the calibration of laboratory-based performance prediction methodology.

Phase 2: Evaluation of Crack Resistance

The crack resistance and failure modes of various geosynthetic-reinforced specimens are evaluated using laboratory tests. The number of cycles to failure (N_f) and the modes of failure, including debonding and vertical cracking, are determined. This phase involves conducting NBFTs at different tensile strain levels and employing DIC to analyze crack propagation patterns and strain distributions. This detailed analysis helps identify the macro-crack development and corresponding failure modes of the specimens.

Phase 3: Numerical Simulations of Pavement Responses

Building on the laboratory test results, numerical simulations are performed to predict pavement responses under various conditions. These simulations help develop predictive equations for key parameters, such as the tensile strain at the bottom of asphalt overlays, as a function of surface deflections measured from FWD tests. These predictive models are essential for selecting appropriate geosynthetic interlayer products tailored to specific pavement conditions.

Phase 4: Damage Index and Field Calibration

This phase focuses on correlating laboratory results with field performance data to establish reliable calibration factors. A damage index is developed to quantify the extent of pavement deterioration and to validate the predictive models. Field calibration involves collecting data from geosynthetic-reinforced pavements under real-world conditions to ensure the accuracy and applicability of the developed models and performance prediction procedure.

Phase 5: Procedure Development and Validation

The final phase involves developing a comprehensive step-by-step procedure for predicting the performance of geosynthetic-reinforced pavements based on site-specific conditions. This procedure is verified through additional field tests to ensure their robustness and effectiveness. This phase ensures that the developed procedure can be seamlessly integrated into routine practice by the NCDOT.

This comprehensive five-phase approach is designed to ensure that the developed procedure for the prediction of reflective cracking performance of geosynthetic-reinforced pavements is robust, reliable, and tailored to the specific needs and conditions of different pavement projects. The integration of PMS data, rigorous laboratory testing, advanced numerical simulations, and field calibration provide a solid foundation for enhancing the performance and longevity of asphalt overlays.

1.4 Report Organization

Chapter 1 introduces the research objectives, background information on the research needs, and various tasks involved in accomplishing the research objectives. Chapter 2 describes the materials and their properties used in the current study. This includes details about the asphalt concrete mixture, dynamic modulus tests on the asphalt mixture, tack coat application rates, dynamic shear rheometer tests on tack coat binders, and the geosynthetic products evaluated. Chapter 3 discusses the test methodologies and experimental programs employed in this research. It covers crack resistance tests, including the laboratory fabrication of beam specimens, air void studies, and four-point bending beam fatigue tests. Additionally, it explains the calibration procedures for measurement systems, DIC techniques, and deflection calibration for notched beam fatigue testing. Chapter 4 presents the numerical simulations of pavement responses. It details the parameters used in the EverstressFE simulations, such as structure information, material parameters, climate data, tire load and configuration, and the analysis output obtained. Chapter 5 evaluates field distress data, focusing on NCDOT interlayer projects and providing an overview of the PMS database. It also discusses various fatigue cracking percentage calculation methods, including the NCDOT Crack Percentage - Corley Method, the Federal Highway Administration's Performance-Related Specifications (FHWA-PRS) Method, the Kansas Department of Transportation (KSDOT) Method, and the Pavement ME Method. Chapter 6 presents the results and discussion of the NBFTs. It covers fatigue models and failure criteria, including basic fatigue models and different types of failure criteria. Additionally, it examines the crack resistance capacity of geosynthetic-reinforced beam specimens. Chapter 7 focuses on the development of field calibration guidelines for geosynthetic products. It outlines the steps involved in developing predictive models for crack resistance and tensile strain, temperature correction models for FWD deflections, calculation of pulse duration for dynamic modulus analysis, determination of damaged dynamic modulus, and the calculation of the Damage Index. Furthermore, it explains the process of translating the Damage Index to fatigue cracking percentages and discusses the limitations and future work. Chapter 8 presents the conclusions and recommendations for future work based on the findings of this research. The report also includes several appendices that provide supplementary information and supporting details. Appendix A offers a literature review on reflective cracking, the functions of geosynthetics, debonding problems, factors influencing bonding, and test methods. Appendix B covers beam bending theory and four-point beam bending stress/strain calculations. Appendix C describes the sinusoidal fitting procedure for tensile strain, and Appendix D provides details on the laboratory fabrication of beam specimens.

Chapter 2. Materials and Properties

2.1 Asphalt Concrete Mixture

The AC used in this study to fabricate the NBFT specimens was obtained as a loose mix from Lane Construction, Inc. in Raleigh, North Carolina. The NCDOT categorizes the procured loose hot-mix as RS9.5C, where the letter ‘R’ indicates the presence of RAP, ‘S’ stands for the surface mixture on the pavement, 9.5 reflects the nominal maximum aggregate size (mm), and ‘C’ represents the middle level of traffic (3-30 million equivalent single axle loads, or ESALs). The RS9.5C mix contains 40% fractionated RAP (hereafter referred to as the RAP-40 mixture). The virgin binder used for the RAP-40 mixture is PG 58-22. The total binder content in this mixture is 6.0 percent. The material characterization and verification of the reported parameters in the job mix formula were carried out as the initial step prior to performance testing. Figure 2-1 presents the aggregate gradation of the RAP-40 mix. Considering the high RAP content in RAP-40, the compaction temperature was selected as 145°C.

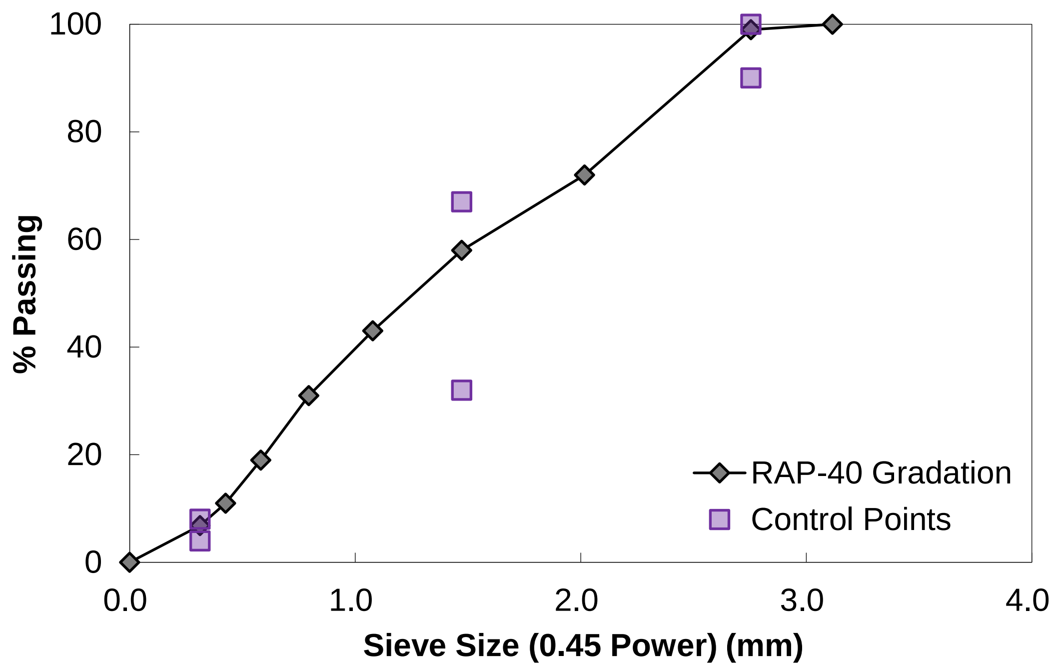

Figure 2-1. Aggregate gradation of RAP-40 mixture.

Even though the loose mix was collected from a hot mix asphalt plant, the need to separate the fine and coarse particles was anticipated while shoveling the AC mix into collection buckets. Hence, a homogenization process was undertaken in the laboratory before fabricating any samples using the loose mix. First, the loose mix was collected in cloth bags and plastic buckets. Figure 2-2 (a) shows the removal of a cloth bag of loose mix from a plastic bucket as a single unit. Then, Figure 2-2 (b) shows the careful removal of the cloth bag from the mix, achieving minimal loss of loose mix. Figure 2-2 (c) shows the obtained single lump of AC mix that has been transferred to a metal bucket.

Figure 2-2. (a) Removing asphalt concrete loose mix in a cloth bag from a collection bucket, (b) removing loose mix from the cloth bag, and (c) loose mix inside a metal bucket.

For the separation process, one batch utilizes four five-gallon buckets, with the total AC mix weighing more than 100 kg (200 pounds). The metal buckets with the loose mix are heated to a temperature of 10°C less than the compaction temperature for two hours. Next, a one-fourth portion from each bucket is poured into four separation pans, and each pan is further divided into 12 small boxes. This procedure aids in producing a well-mixed asphalt mix. The four buckets of the loose mix are divided into 12 cloth bags for easy storage (three bags per bucket). A storage bag consists of four small boxes, each randomly selected from the four separation pans. Figure 2-3 (a) and (b) respectively show the separation pans and cloth bags used for storage. These separated mixes in the cloth bags are used later for sample fabrication and the material characterization study. Depending on the material requirements, this separation process could be repeated.

(a) (b)

Figure 2-3. (a) Separation pans and (b) cloth bags for preparing a well-mixed asphalt mixture.

The theoretical specific gravity and the bulk specific gravity of the loose mix with 40% RAP were measured as per AASHTO T 209-20 (AASHTO 2020a) and AASHTO T 331-17 (AASHTO 2017a), respectively. The maximum specific gravity for the AC mix was found to be 2.44 g/cm^3.

2.2 Dynamic Modulus (|*E**|) Tests of Asphalt Mixture

The linear viscoelastic properties of AC mixtures can be determined via dynamic modulus (|*E**|) tests that measure a specimen's stress-strain relationship under continuous sinusoidal loading. The parameters obtained are the complex modulus values and time-temperature (t-T) shift factors. The shift factor (a_T) aids in representing the effects of time and temperature via a unique parameter referred to as 'reduced time/frequency', f_R , defined here as Equation (2-1).

$$f_R = f \times a_T \tag{2-1}$$

where

f_R	=	reduced frequency, Hz,
f	=	loading frequency, Hz, and
a_T	=	time-temperature shift factor.

Figure 2-4 explains the linear relationship between the air void content and weight of gyratory-compacted samples. The test specimens are cylindrical specimens 38 mm in diameter and 110 mm in height, cored and cut from a gyratory-compacted sample of 180-mm height. The air void content of each specimen obtained from the gyratory-compacted samples should be maintained at 6 percent. In order to prepare 38-mm cylindrical specimens for dynamic modulus tests with 6% air void contents, an air void study of the gyratory-compacted samples was carried out as per AASHTO R 83-17 (AASHTO 2021). The gyratory-compacted samples with different weights of AC mix were compacted to a consistent height of 180 mm. Then, the air void contents were measured for the four 38-mm diameter cylindrical specimens that were cored from each gyratory-compacted sample. Figure 2-4 presents the results of the air void study. A linear relationship is established between the weight of the gyratory-compacted sample and the air void content. This relationship helps to predict the exact weight required for a 180-mm tall gyratory sample to produce four 38-mm diameter and 110-mm tall cylindrical samples with 6% air void content. Figure 2-5 presents the dynamic modulus test results for three replicates of each sample made of the RS9.5C RAP-40 mixture at different temperature/frequency combinations conducted as per AASHTO TP 132-19 (AASHTO 2019).

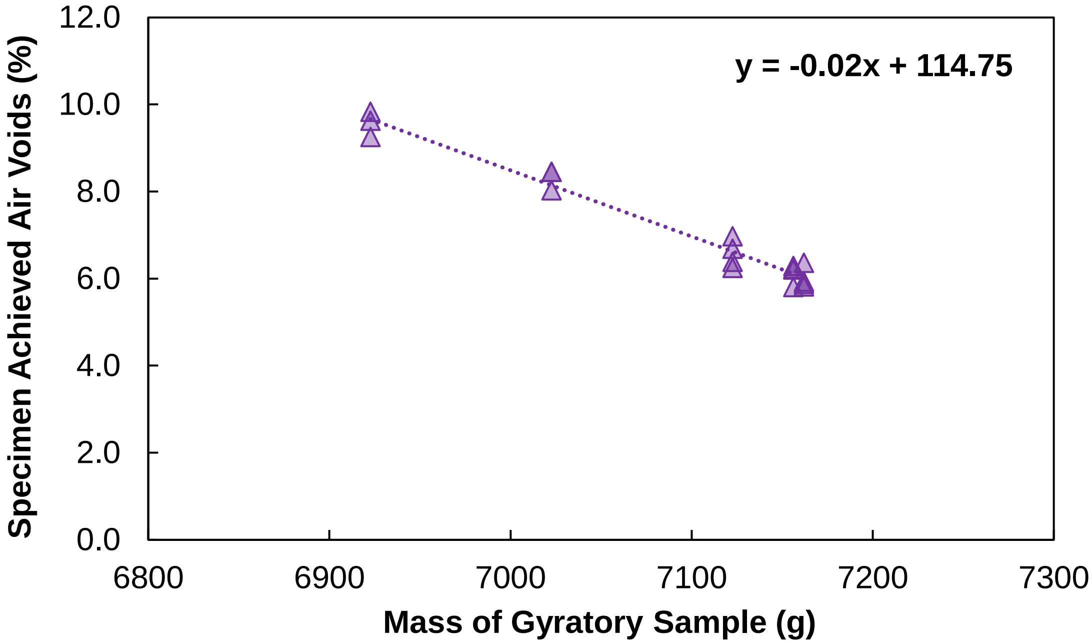

Figure 2-4. Linear relationship between air void content and weight of gyratory-compacted samples.

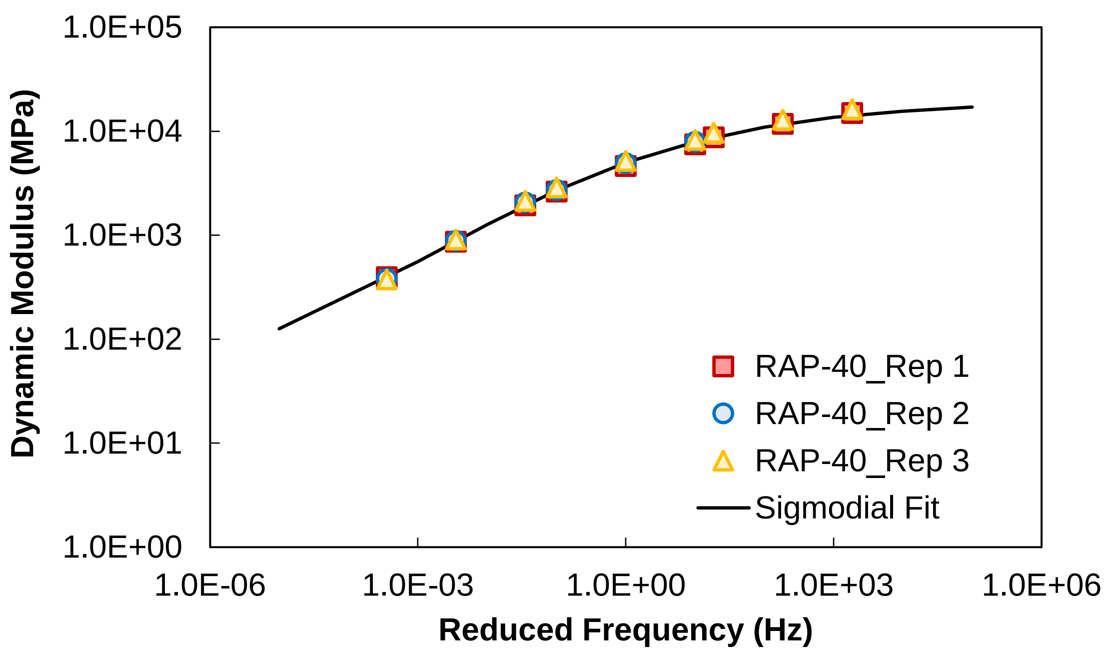

Figure 2-5. Dynamic modulus mastercurve for RS9.5C RAP-40.

An Asphalt Mixture Performance Tester (AMPT) Pro was used as the testing device, and the tests were performed at three temperatures, 4°C, 20°C, and 40°C, and six frequencies, 25 Hz, 10 Hz, 5 Hz, 1 Hz, 0.5 Hz, and 0.1 Hz. A mastercurve was developed by shifting the data points of each replicate horizontally at an arbitrarily selected reference temperature, in this case, 20°C. Equation (2-2) is the sigmoidal function used to fit the dynamic modulus mastercurve. Equation (2-3) represents the t-T shift factor in a quadratic function. The Prony series coefficients are obtained by fitting the storage modulus with the function shown in Equation (2-4) using the collocation method (Park et al. 1996; Schapery 1962).

$$\log\left|E^*\right| = \delta + \frac{\alpha}{1+\dfrac{1}{e^{\beta+\gamma\log(f_R)}}} \tag{2-2}$$

$$\log(a_T) = a_1T^2 + a_2T + a_3 \tag{2-3}$$

$$E(t) = E_\infty + \sum_{i=1}^{m} E_i e^{-t/\rho_i} \tag{2-4}$$

where

a_1, a_2, a_3	=	regression coefficients,
$\|E^*\|$	=	dynamic modulus, MPa,
δ	=	minimum value of dynamic modulus,
$\delta+\alpha$	=	maximum value of dynamic modulus,
β, γ	=	material constants describing the shape of the sigmoidal function,
$E(t)$	=	relaxation modulus, MPa,
E_∞	=	equilibrium modulus, MPa,
E_i	=	relaxation strength, MPa,
ρ_i	=	relaxation times, s,
m	=	number of Maxwell elements, and
t	=	time, s.

An Excel solver developed at NCSU, named FlexMAT™, was used to automate the above steps and provide the Prony series representation of the relaxation modulus. The output parameters obtained were used as material model property inputs for the numerical modeling software, FlexPAVE™ 1.1. Table 2-1 presents the t-T shift factor function coefficients for the mixture obtained while fitting Equation (2-2).

Table 2-1. Shift Factor Coefficients of RS9.5C RAP-40 Study Mixture

Shift Factor Coefficient	Value
a_1	9.63×10^{-4}
a_2	-0.167
a_3	3.084

2.3 Geosynthetic Products

Five different geosynthetic reinforcements were used as interlayers in this project. Figure 2-6 presents images of these five different geosynthetic products, and Table 2-2 presents the nomenclature details for each geosynthetic product type and the properties of each geosynthetic product supplied by the manufacturer.

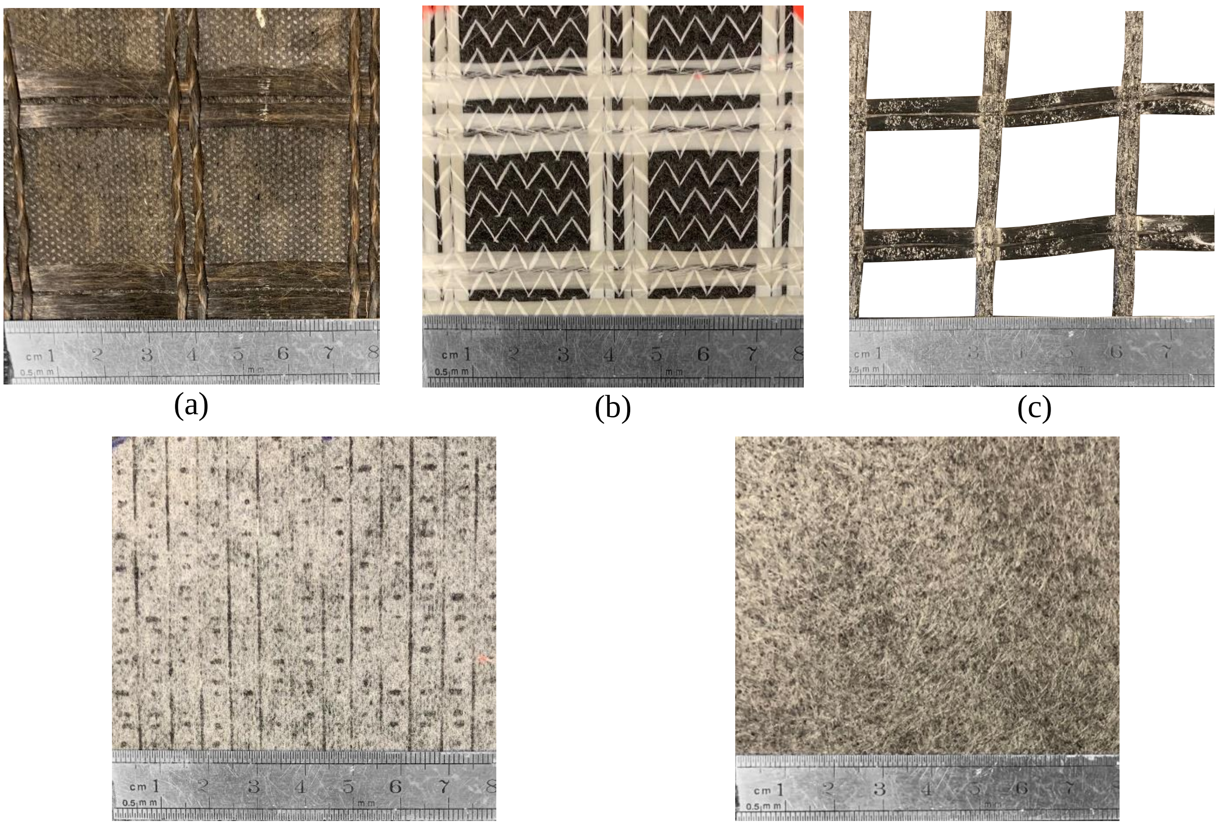

(a) (b) (c)

(d) (e)

Figure 2-6. Geosynthetic samples: (a) PC#1, (b) PC#2, (c) PaG, (d) PM, and (e) PF.

Table 2-2. Properties of Study Geosynthetic Products

Physical Properties			Mass/unit area	Tensile strength (kN/m)	Strip tensile strength (N/50 mm)	Grab tensile strength	Tensile elongation	Melting point	Asphalt retention
Units	Metric		g/m²	kN/m	N/50 mm	N	%	°C	L/m²
	Imperial		oz/yd²	lb/in.	lb/2 in.	lb	%	°F	gal/yd²
Paving Composite	PC#1	Metric	270	50	-	-	≤ 3%	255	(Bitumen coated > 60%)
		Imperial	8	285	-	-	≤ 3%	490	
	PC#2	Metric	678	115	-	-	≤ 3%	800	1.2
		Imperial	20	655	-	-	≤ 3%	1472	0.27
Paving Mat	PM	Metric	237	50			<5	>232	0.47
		Imperial	7	280			<5	>450	0.1
Paving Grid	PaG	Metric	405	100			≤ 3%	> 232/>820	Pressure-sensitive adhesive backing
		Imperial	12	571			≤ 3%	>450/>1508	
Paving Fabric	PF	Metric	139	-	-	449	50%	160	0.91
		Imperial	4.1	-	-	101	50%	320	0.2

2.4 Tack Coat Application Rates

The NCDOT Quality Management Service manual (NCDOT 2018), Table 605-1, stipulates an optimal application rate of 0.181 L/m^2 (0.04 gal/yd^2) for emulsified tack coats, which eventually leaves a residue of 0.03 gal/yd^2. Emulsified tack coats generally are not recommended for geosynthetics applications. The optimal tack coat application rate for geosynthetic-reinforced pavements ranges from 12 to 50 times more than the optimal residual application rate of unreinforced pavements depending on the selected geosynthetic product. Such an increase in the tack coat does not allow the emulsion to cure effectively due to the thick emulsion layer formed on the pavement surface. Although there are cases where emulsified asphalt has been used successfully as a tack coat, in those cases the bond strength has developed more slowly than when using a hot binder. Moreover, sufficient time should be provided for emulsions to break and set before the geosynthetic product is placed (Button and Lytton 2007). In addition, an increased tack coat application rate during the geosynthetic application facilitates emulsion runoff, leading to the non-uniform distribution of the tack coat and the potential for debonding. Hence, PG 64-22 hot binder was selected as the tack coat for this study.

Earlier studies have reported that the variability in the target and achieved application rates of tack coats in the field ranges from 4% to 106% (Al-Qadi et al. 2008; Mohammad et al. 2012). Based on such variability, the dry and wet conditions in the field can be mimicked by varying the residual application rate by ± 66% of the optimal residual application rate for unreinforced sections, i.e., ± 0.091 L/m^2 (0.02 gal/yd^2). Hence, for the unreinforced control specimen (CS) in this study, three residual application rates of PG 64-22 asphalt binder, 0.045 L/m^2 (0.01 gal/yd^2), 0.136 L/m^2 (0.03 gal/yd^2), and 0.226 L/m^2 (0.05 gal/yd^2), were used. The optimal application rates used for the geosynthetic-reinforced specimens follow the manufacturers' recommendations. The dry and wet application rate conditions were determined by adding and reducing 0.091 L/m^2 (0.02 gal/yd^2) from the manufacturer's optimal application rate, respectively. Table 2-3 provides a summary of the tack coat application rates used in this project.

Table 2-3. Summary of Tack Coat Application Rates for Geosynthetic Products Used in Study

Geosynthetic type	**CS**	**PC#1**	**PC#2**	**PM**	**PF**	**PaG**
Tack coat type	PG 64-22					
Application rate, gal/yd^2 (L/m^2)	0.03 (0.14)	0.14 (0.63)	0.33 (1.49)	0.12 (0.59)	0.08 (0.36)	0.23 (1.04)

2.5 Dynamic Shear Rheometer (|*G**|) Tests of Tack Coat Binder

Cho and Kim (2016) verified the application of the t-T superposition principle to determine the ISS and interface shear stiffness of geosynthetic-reinforced AC. In that study, GlasGrid-reinforced AC cored specimens were sheared in a Modified Asphalt Shear Tester (MAST) under constant displacement to measure the ISS at different test temperatures. The t-T shift factors (a_T) of the AC mixture measured via dynamic modulus testing were used initially to verify the t-T superposition principle for the MAST test outcomes. The MAST test results obtained from the unreinforced specimens were used to create a mastercurve with the aid of the mixture's a_T. However, the MAST tests of the geosynthetic-reinforced specimens demonstrated spurious results using the same mixture's a_T. Therefore, using a dynamic shear rheometer (DSR), frequency sweep tests were conducted using a tack coat asphalt binder to obtain the asphalt binder a_T (Cho et al. 2017b). The asphalt binder a_T was used successfully to construct an ISS mastercurve for the geosynthetic-reinforced specimens. Thus, the conclusion drawn from the Cho et al. (2017b) study is that the mixture a_T applies to unreinforced MAST test specimens, whereas the asphalt binder a_T is applicable for geosynthetic-reinforced specimens.

In this study, the NCSU research team conducted the DSR testing to determine the tack coat a_T. The DSR measures the dynamic shear modulus ($|G^*|$) and determines the t-T shift factors of the asphalt binder. The DSR used in this study, Anton Paar MCR 302, is a user-friendly device that is capable of wide temperature ranges, as low as -160°C to as high as 1000°C, in minutes for any type or combination of rheological tests. These mechanical tests were performed as frequency sweep tests at 5°C, 20°C, 35°C, 50°C, and 64°C. The loading frequency ranged from 0.1 Hz to 30 Hz at 1% shear strain amplitude. The frequency sweep tests were designed to help construct mastercurves of the dynamic shear modulus values and obtain t-T shift factors for the binder and emulsion residue used in this study. The asphalt residue used for DSR testing was recovered according to AASHTO R 78-16 (AASHTO 2020b) Method B.

Analysis of DSR test outcomes is a simple process due to the long-established standards and practices of the device. If the results of any two tests of the same emulsion type exceed the recommended 6.4% difference specified in AASHTO T 315-12 (AASHTO 2020c), then neither result should be used, and the emulsion must be retested. In this study, the DSR test results were averaged per emulsion and input into a mastercurve template builder using an Excel spreadsheet. This Excel spreadsheet uses the dynamic shear modulus, frequency, and temperature data obtained from the DSR tests to calculate the shift factors for each emulsion by fitting the data points to the Christenson–Anderson–Marasteanu (CAM) model (Christensen and Anderson 1992) at a reference temperature, as given in Equation (2-5). The general form of the t-T shift factor equation is given as Equation (2-6), where $|G^*|_g$ is the glassy dynamic shear modulus and is equal to 1 GPa for asphalt binder. ω_c, m, and v are the CAM model fitting parameters for the dynamic shear modulus mastercurve. Equation (2-6) describes the reduced frequency, ω_R, where a_T is the shift factor at temperature T and ω is the actual testing angular frequency.

$$\left|G^*\right|(\omega_R) = \left|G^*\right|_g \left[1+\left(\frac{\omega_c}{\omega_R}\right)^v\right]^{-\frac{m_e}{v}} \tag{2-5}$$

$$\omega_R = a_T \times \omega \tag{2-6}$$

where

$\lvert G^*\rvert$	=	dynamic shear modulus,
$\lvert G^*\rvert_g$	=	glassy dynamic shear modulus when frequency tends to infinite,
ω_c	=	constant, location parameter where loss modulus equals storage modulus,
m_e, v	=	constant, dimensionless shape parameter.

Equation (2-3) was employed to fit the t-T shift factor. Table 2-4 presents the shift factor coefficients for each emulsion in this study, measured at the reference temperature of 20°C. Figure 2-7 shows the dynamic shear modulus mastercurves for PG64-22

Table 2-4. Shift Factor Coefficients of PG 64-22 Binder Tack Coat Used in Study

Shift Factor Coefficients	a_1	a_2	a_3
PG 64-22	0.000823	-0.15368	2.741548

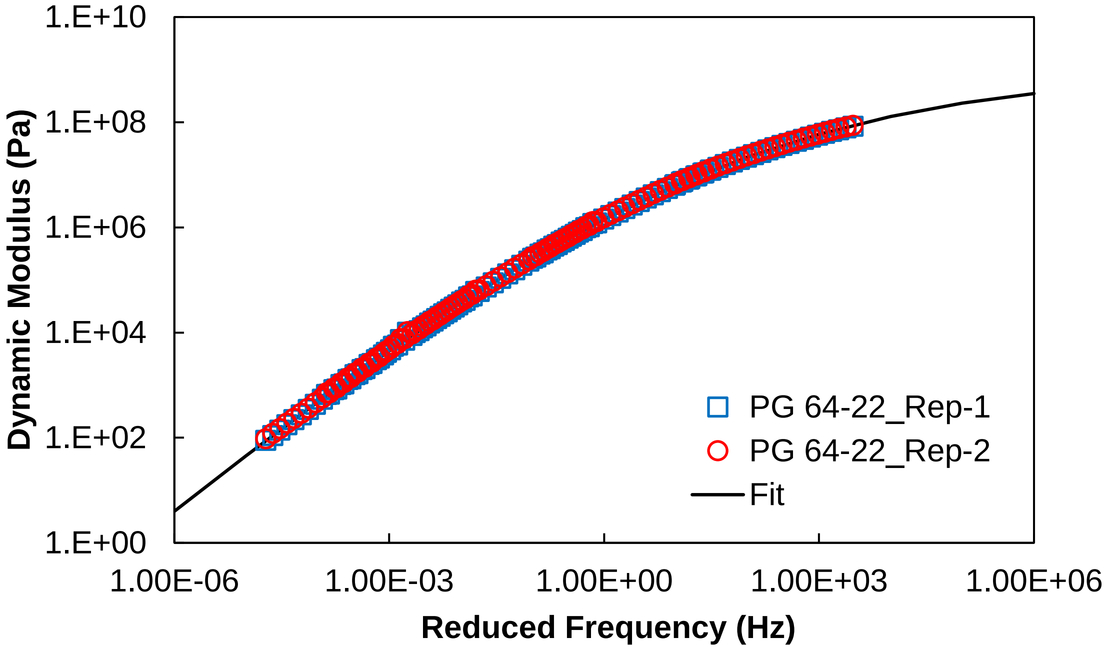

Figure 2-7. Dynamic shear modulus mastercurves for PG 64-22 binder tack coat.

Chapter 3. Sample Fabrication and Test Methods

This section describes research efforts to produce test specimens with uniform air voids distribution and test methods used in the study.

3.1 Crack Resistance Tests

3.1.1 Laboratory Fabrication of Beam Specimens

The major steps involved in the laboratory fabrication of beam specimens for the NBFTs are (1) compact the slab sample using a roller compactor, (2) prepare the geosynthetic product for slab samples, (3) apply the tack coat using a hot spray gun, (4) place the geosynthetic product on the slab sample, (5) prepare the beam specimen, (6) prepare the beam holding jig, (7) cut a notch in the beam specimen, and (8) speckle the beam specimen for DIC testing. A detailed explanation of each step is provided in Appendix E.

3.1.2 Air Void Study

Figure 3-1 schematically presents the dimensions of a beam cut into three parts for the air void study. Figure 3-2 (a) shows the actual beam specimens cut into three equal portions. Figure 3-2 (b) shows that the middle one-third of each beam is cut into two pieces, thus creating a bottom layer that is 18-mm (0.7-in.) thick and a top layer that is 36-mm (1.42-in.) thick.

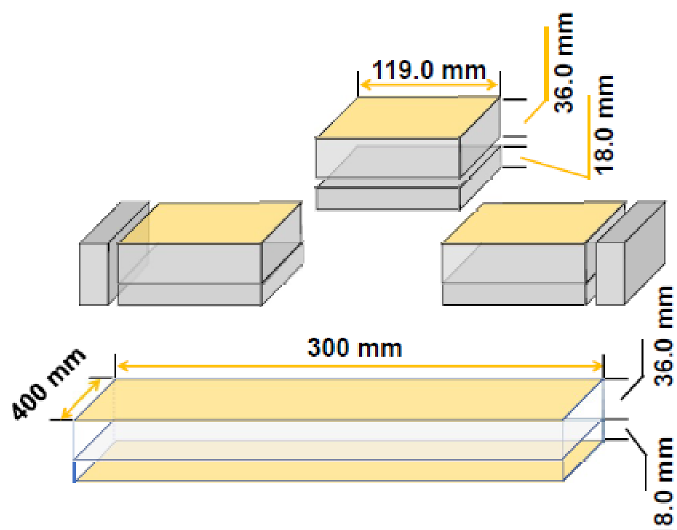

Figure 3-1. Schematic diagram of beam cut into three parts for air void study.

(a)

(b)

Figure 3-2. (a) Beam specimen cut into three equal portions and (b) middle one-third portion cut to create bottom layer (18-mm thick) and top layer (36-mm thick).

The nomenclature used to identify the beam specimens is ‘SYM’ ‘X’ ‘#’ and ‘SYM’ ‘X’ – ‘Y’ ‘SYM’ for the air void study specimens. Table 3-1 presents details of each designation.

Table 3-1. Nomenclature Details for Slab Specimens

Designation	Symbol/Acronym	Details
SYM	*	40% RAP
	+	20% RAP
	↑	Top part of top/bottom slab layer
	↓	Bottom part of top/bottom slab layer
X	A, B, C, etc.	Tag for slab sample
Y	T	Top of beam specimen
	B	Bottom of beam specimen
#	1, 2, 3	Beam specimens cut from a slab; beam in the compaction direction is numbered from ‘1’.

For the *B and +B specimens, the target air void content of 8.5% in the top layer resulted in a measured air void content of 12 percent. Visual inspection and height measurements of the slab surface proved the compactor’s inability to achieve the target height, thus leading to a higher achieved air void content. However, the bottom layer of the beam specimen in all cases showed an achieved air void content of 10% or greater, irrespective of the target air void content and even after achieving the target height. This difference for the bottom layer of the specimen compared to the top layer raised the concern that an air void gradient was present throughout the specimen. The cold compacting face of the roller compactor could be a contributor to this phenomenon as well. To address this concern, the research team decided to flip the bottom layer prior to the top layer compaction. Figure 3-3 shows the step-by-step procedure for flipping the slab.


(a)

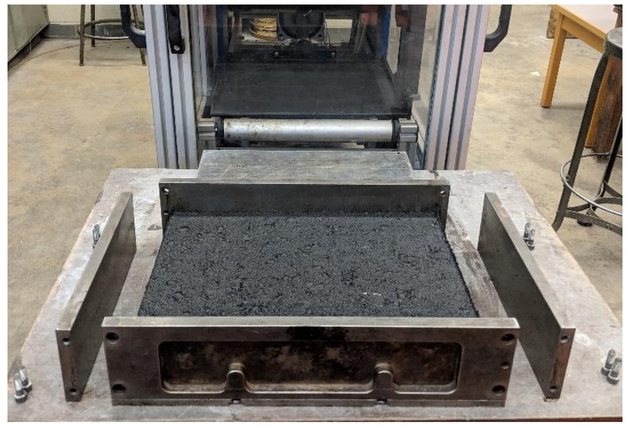
(b)


(c)

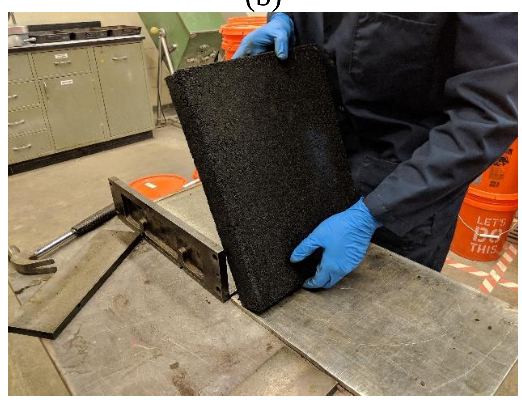
(d)


(e)

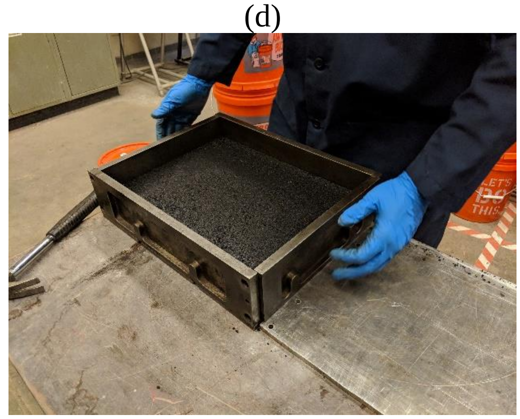
(f)

Figure 3-3. (a) Measuring height of bottom layer to check the level, (b) side plates of mold removed, (c) pushing bottom layer out of mold, (d) flipping over bottom layer, (e) pushing flipped bottom layer back into mold, and (f) closing sides of mold.

The results of the air void study of the slabs with the bottom layer flipped show that the air void content of the bottom layer of the beam specimen (top portion of the bottom layer of the slab) matches the achieved air void content of the top layer whose target air void content was higher than 8.5 percent. Figure 3-4 presents the air void study results for RAP-40. Measurements of the bottom portion of the same slab sample's bottom layer showed a 2% to 3% difference in the achieved air void contents. The difference in air void contents indicates an air void gradient in the layers. Because the top layer uses the bottom portion of the layer for the specimen, the air void gradient is not evident, whereas the top portion of the bottom layer (which would become the bottom layer in the beam specimen) shows a higher air void content. Therefore, all the beam specimens were made with the bottom layer flipped before the top layer was placed to achieve a consistent air void content throughout the specimen. However, flipping the bottom layer did not guarantee the consistency of the air void content throughout the depth of the beam for all target air void contents. Once the target air void content was below 8.5%, the top layer's air void content did not match the linear trend that was found in the flipped bottom layer. The resistance provided by the RAP coupled with the difficulty in compacting under the constraint of the size of the mold in the laboratory could be reasons for this outcome. Therefore, to achieve an adequate air void content under the limited laboratory conditions, the research team decided to achieve an air void content of 10%.

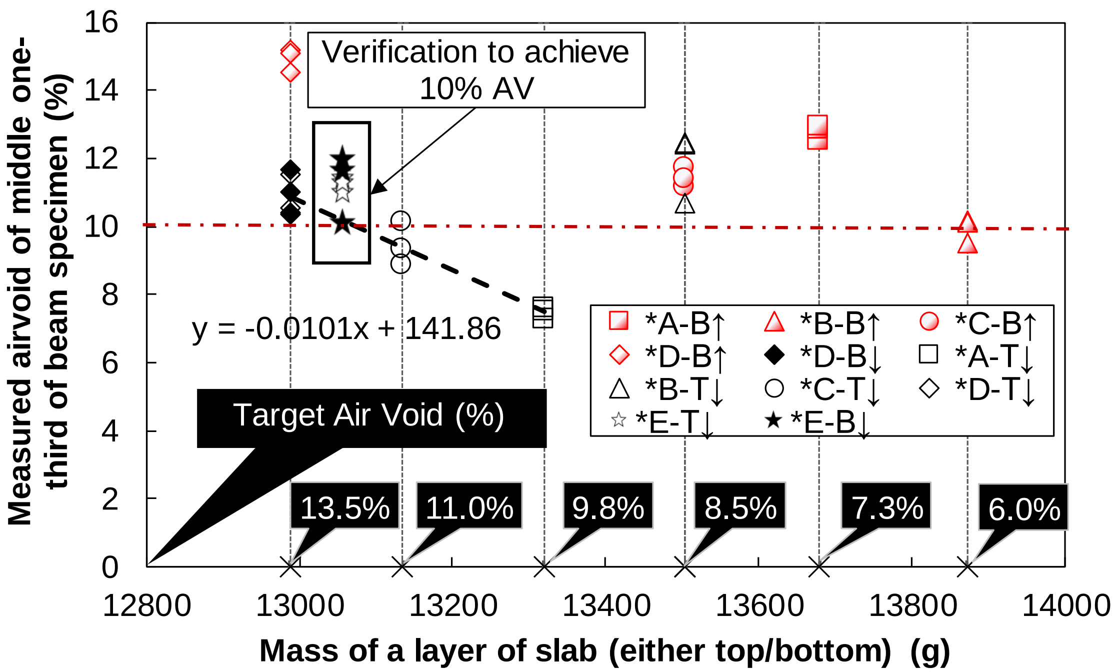

Figure 3-4. Air void study results for RS9.5C RAP-40.

Also, a visual inspection of the side walls of the molds in the compaction direction indicated an imprint of the compaction pattern. Figure 3-6 shows the compaction imprint and indicates the likelihood of an air void gradient in the samples. The imprint was traced and was found to overlap with the beam dimensions, as shown in Figure 3-6, which served to suggest the cause for the air void content variability among the three beam specimens cut from the same slab. The research team then decided to use only two beams from each slab for the performance study in order to maintain air void content uniformity. Figure 3-7 depicts the revised configuration for cutting beams from the slab.

Figure 3-5. Compaction imprint on side walls of mold.

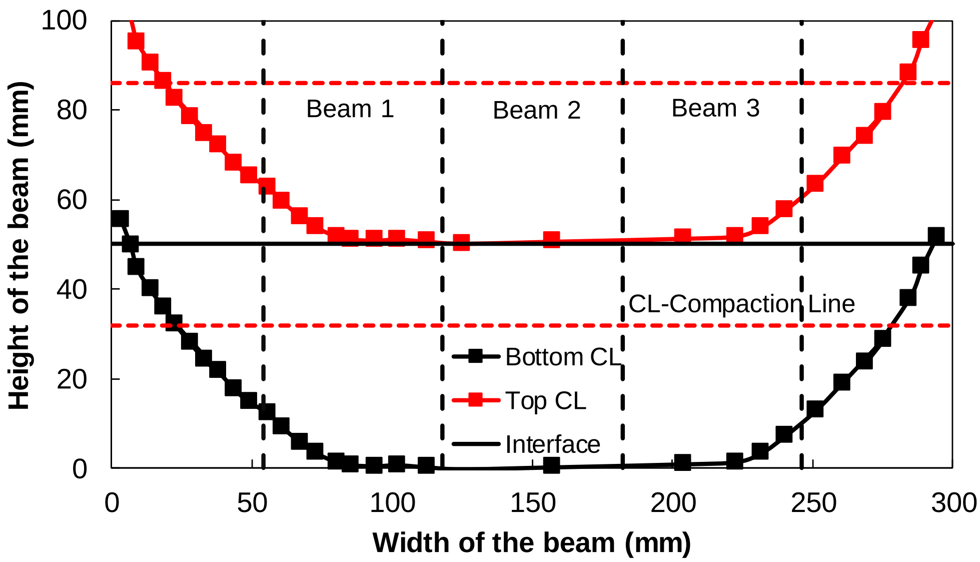

Figure 3-6. Traced imprint of side walls of molds with beam dimensions overlapping.

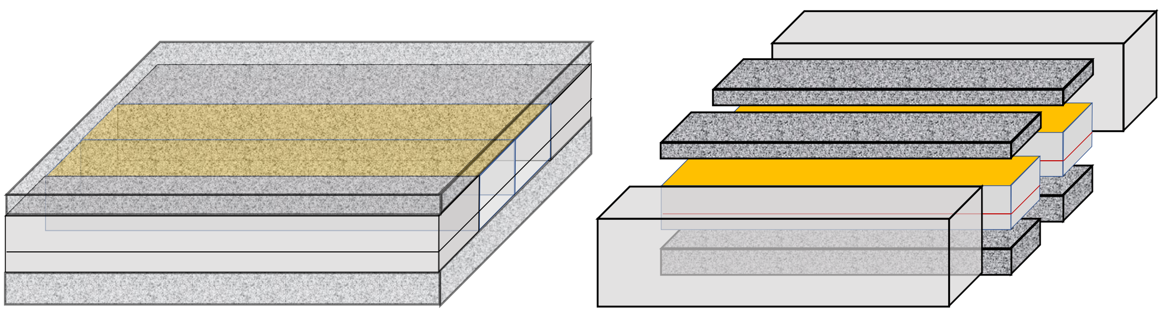

Figure 3-7. Revised configuration for cutting beams for performance study.

In order to confirm these findings, the research team carried out a study of two slab samples with three beams from each slab. Figure 3-8 shows the variability of the air void content in the RS9.5C RAP-40 slab, with an average air void content of 11.7% and a standard deviation of 0.8 for the three beam specimens.

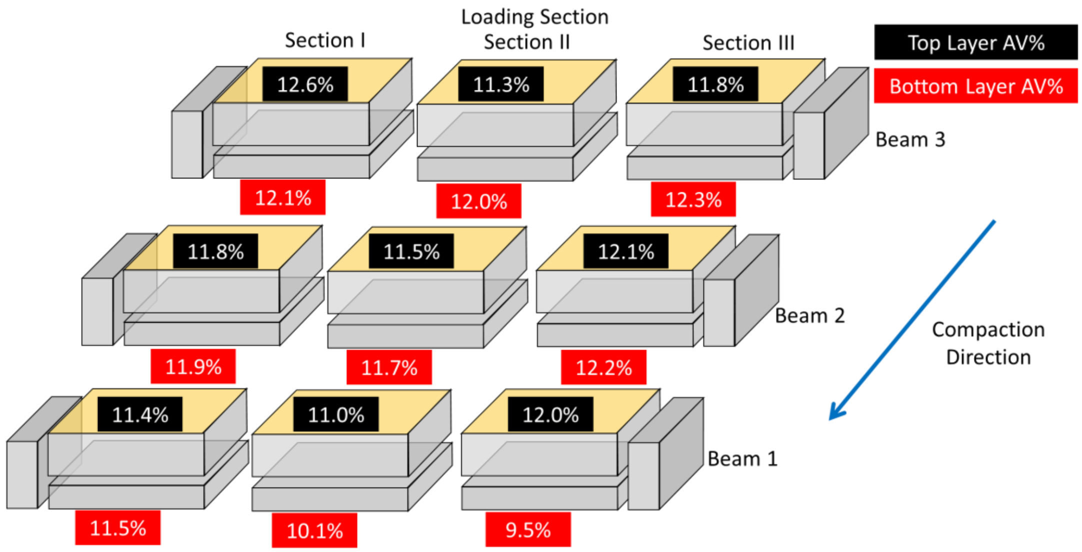

Figure 3-8. Air void study results for RS9.5C RAP-40 mixture beam specimens cut from slab.

3.1.3 Four-Point Bending Notched Beam Fatigue Test

The four-point bending beam test device used in this study simulates the Mode I pavement cracking mechanism via beam bending. Standard beam fatigue tests, ASTM D7460-10 (ASTM 2010) and AASHTO T 321-17 (AASHTO 2017b), were carried out using an AC beam specimen (from a single layer of a slab sample) with dimensions of 50 mm × 63 mm × 380 mm (1.97 in. × 2.48 in. × 14.96 in.) subjected to cyclic loading (control stress/control strain) at a frequency of 10 Hz. AASHTO T 321-17 (AASHTO 2017b) stipulates that a four-point beam loading device should be capable of (1) providing repeated sinusoidal loading at a frequency range of 5 Hz to 10 Hz, (2) subjecting specimens to four-point bending with free rotation and horizontal translation at all load and reaction points, and (3) forcing the specimen back to its original position (i.e., zero deflection) at the end of each load pulse.

The test device from Cox and Sons used in this study complies with AASHTO T 321-17 (AASHTO 2017b). The apparatus was adapted to fit in the MTS 810 Universal Testing Machine (UTM) that is available at the NCSU laboratory. Figure 3-9 shows the loading and free rotation points in the device.

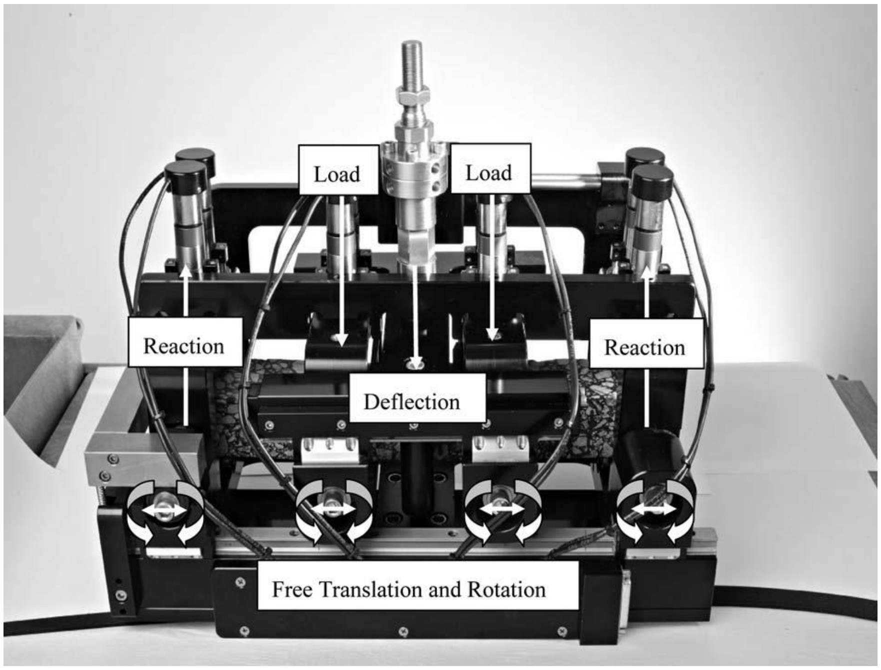

Figure 3-9. Cox and Sons four-point bending beam test apparatus (ASTM D7460-10).

The spacing between the clamps is 119 mm (4.69 in.), and the beam length between the outside clamps is 357 mm (14.06 in.) in this apparatus. A customized environmental chamber with a glass-covered opening, shown in Figure 3-10, was used to fit the apparatus and to condition all the beam fatigue test specimens.

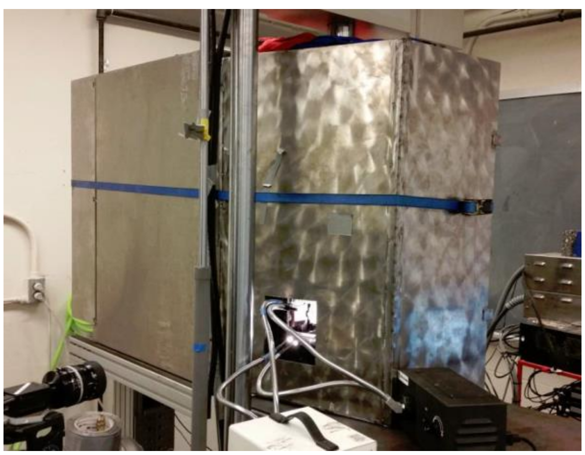

Figure 3-10. Custom-made environmental chamber attached to MTS to control temperature during beam fatigue tests.

ASTM D7460-10 (ASTM 2010) and AASHTO T 321-17 (AASHTO 2017b) call for the on-specimen displacement control mode; however, the Material Testing System, the servo-hydraulic testing machine used in this study, does not have a closed loop system from the on-specimen linear variable displacement transducer (LVDT). Therefore, the NBFTs were conducted in constant actuator displacement control mode at the frequency of 10 Hz at 23°C. In addition to the displacements measured by the actuator LVDT, on-specimen displacements were measured by an additional LVDT mounted on the neutral axis (i.e., mid-depth) of the beam.

Three different strain values were calculated and used in this study: tensile strain at the bottom of the beam, calculated from the actuator displacement (denoted as ε_{act}), tensile strain at the bottom of the beam, calculated from the on-specimen displacement (denoted as ε_{os}), and tensile strain at the interlayer, calculated from the on-specimen displacement (denoted as ε_{int}). Note that ε_{int} is one-third of ε_{os} and that ε_{int} in the NBFT is the strain of interest when the findings from this study are extended to overlays in the field. Note also that, in actuator displacement control mode, the on-specimen displacement amplitude and therefore ε_{os} will change as the loading continues and the damage in the beam increases, even though the actuator displacement amplitude and ε_{act} are constant throughout the NBFT. In this study, ε_{os} at the 50th loading cycle was used as the initial strain in the NBFTs.

3.2 Calibration of Measurement Systems for Study Test Devices and Methods

3.2.1 Digital Image Correlation Technique

A DIC system is a non-contact measurement system that can be employed to compute the relative displacements and strain activity in a 2-D plane by comparing images of a deformed specimen with images of an initial, undeformed reference specimen using advanced mathematical techniques. To implement DIC analysis of the differences between the initial image and the deformed images, the undeformed reference image is divided into small subsets, and then the corresponding locations of these subsets in the deformed images are tracked by matching their grayscale pixel levels, as shown in Figure 3-11. By monitoring the location of the subsets, the horizontal and vertical displacements of the center point of each subset in the pixels can be determined at different stages of the testing (Seo et al. 2002).

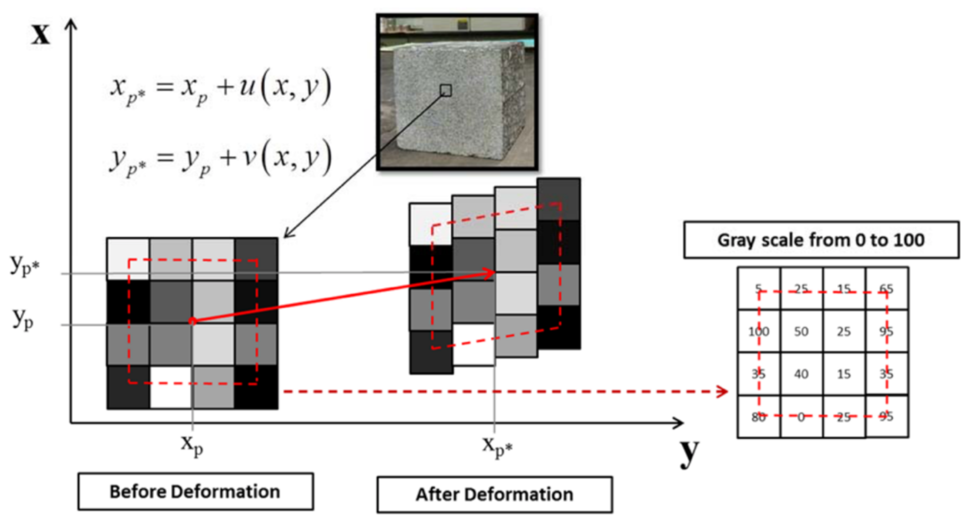

Figure 3-11. Digital image correlation analysis of differences between initial image and deformed image (Seo et al. 2002).

The DIC system set-up includes a 5-megapixel camera along with a 35–75 mm f: 3.3–4.5 manual focus lens to capture images. Two dual-fiber optical gooseneck lights were used in this study to provide consistent, cool, and sufficient lighting on the specimen surface. An adjustable tripod stand with built-in bubble levels was used to level the camera and placed at an approximate distance of 75 cm from the specimen and at the same height and lateral position as the specimen. A relatively high shutter speed of 1.5 ms was used to prevent blurry images. An f-stop of 3.3, a fairly wide lens aperture size, was used to let the maximum possible light hit the camera sensor. A relatively low gain setting close to -3.9 db was used to prevent unwanted image noise. The DIC camera was connected to a computer that was installed with two commercially available DIC software packages developed by Correlated Solutions, Inc: Vic-Snap and Vic-2D. Vic-Snap is used to acquire images during testing and control the camera shutter speed, position, and lighting levels. VIC-2D is 2-D DIC analysis software that is used to calibrate the scale, analyze the captured images, and calculate the displacements and strain through comparisons of images using advanced mathematical algorithms. Key aspects and details regarding DIC analysis can be found in Safavizadeh and Kim (2017).

3.2.2 Calibration of DIC System for Notched Beam Fatigue Testing

One of the primary reasons for conducting NBFTs in this research was to track the crack propagation in AC beams with and without geosynthetic reinforcement. The NBFTs were conducted in constant actuator displacement mode at 10 Hz frequency and the DIC technique was employed to capture and measure the crack lengths and widths. The full crack path at a specific loading cycle can be captured at its peak displacement amplitude. However, triggering the DIC camera at that exact time is tedious. The DIC system commonly uses the same cable to send the trigger signal and receive the captured image data between the computer and the camera. This process results in inaccuracy in the timing of image acquisition if the time interval is too short due to the delay in the communication with the camera and saving the image. Therefore, a hardware trigger is preferred for high-frequency tests, which involves an external camera triggering signal. A new fulcrum module was procured for this study to trigger the camera, depending upon the drive signal sent to the actuator. This section explains the calibration of the fulcrum module to check its reliability prior to conducting the NBFTs.

The maximum frame per second of the new DIC camera is 71. Thus, for a 10 Hz test, the maximum number of data points/images acquired per cycle (0.1 s) is seven. However, this number of data points may not be sufficient to construct a sinusoidal fit. Therefore, capturing images at the alternate load cycle and at a constant phase angle difference helps create a complete cycle. Figure 3-12 shows a single DIC cycle measured during a cyclic test. Typical DIC system software sets the trigger voltage signal depending on the MTS controller's drive signal that simulates the constant displacement amplitude. The MTS controller sends the drive signal to the actuator valves, and then the drive signal is read out via an analog reader and fed to the DIC system's data acquisition system (DAQ). VIC-Snap, the DIC image-capturing software, with the aid of the DAQ sets the trigger voltage and sends a trigger signal through a cable to the camera; this cable is separate from the image-saving cable to the computer. This process allows the accurate acquisition of DIC images.

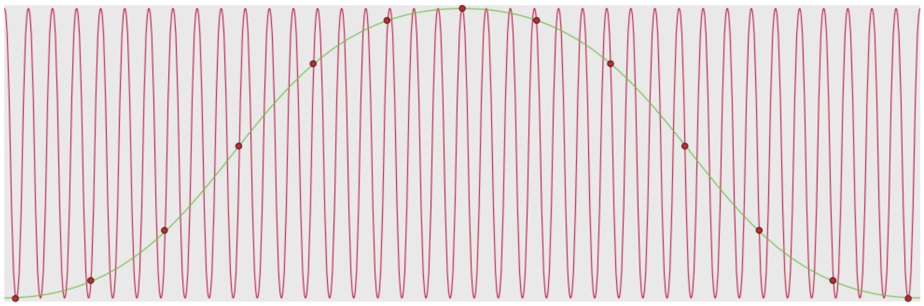

Figure 3-12. Typical fulcrum module capturing process during a cyclic fatigue test (from VIC-2D flyer).

Figure 3-13 shows the typical input options available in VIC-Snap's fulcrum module. In this study, a sequence recording was activated at a constant phase step for every n^{th} cycle, depending on the user's requirement. For instance, a 15° phase step at every 200 cycles triggers the camera to capture images that provide a full cycle with 24 images (360/15 = 24). However, the number of actuator cycles between two consecutive images for a 10 Hz test is four. The software must monitor one cycle to check the current frequency and limits, monitor another cycle to obtain the waveform/voltage, and then trigger the camera. Thus, to obtain a single DIC cycle (360°) that contains 24 images, the actuator must complete 96 cycles. Then, the next sequence initiates at the 200^{th} actuator cycle, and so on.

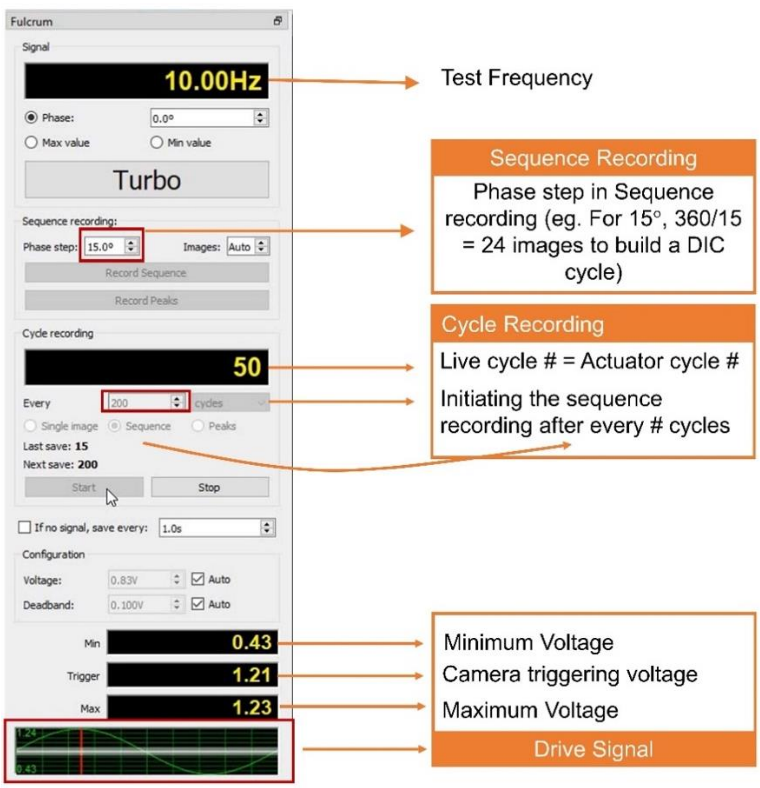

Figure 3-13. Input parameters for DIC fulcrum module.

Figure 3-14 shows the displacements measured using the actuator and DIC system in this study. As shown, the DIC system measurements match the actuator displacements, thus validating the accuracy of the DIC system for taking displacement measurements during fatigue tests.

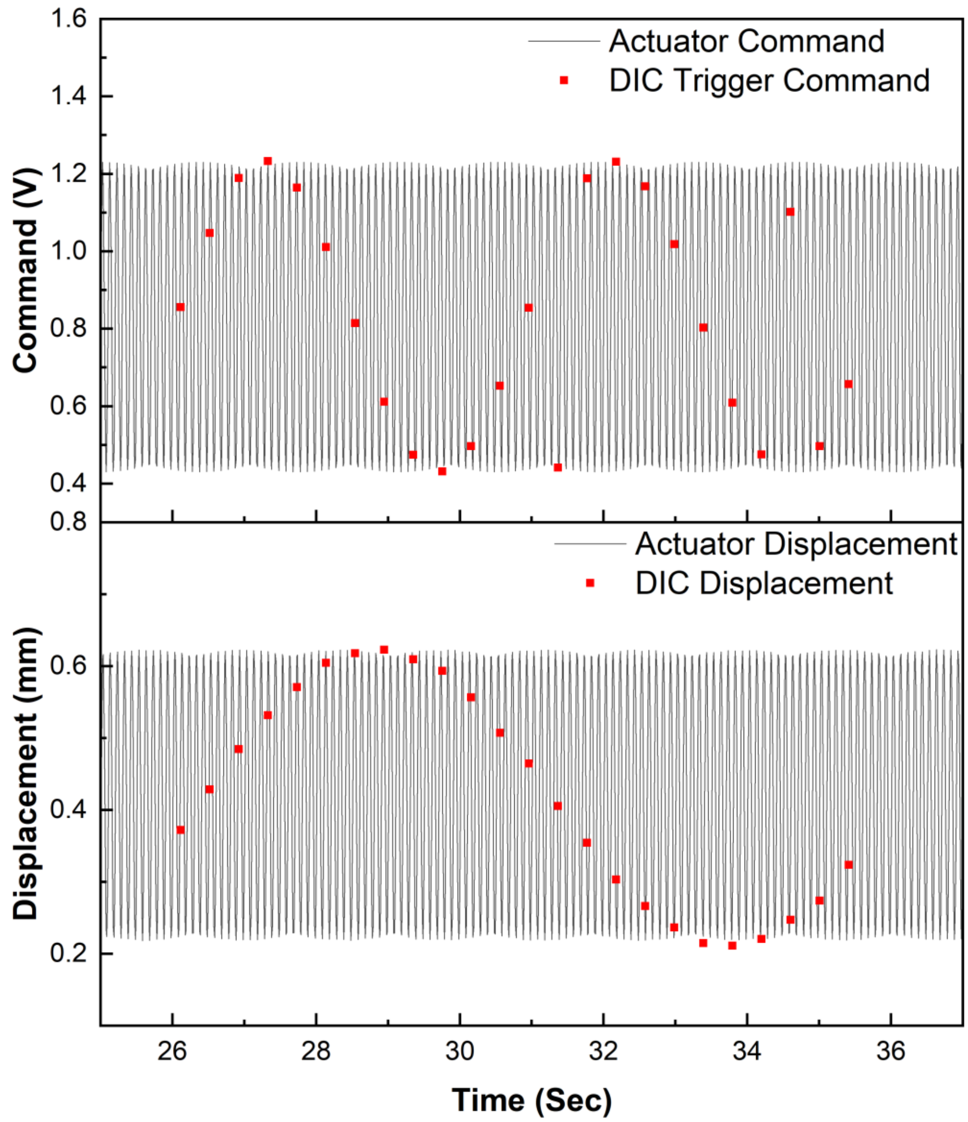

Figure 3-14. (Top) recorded commands: actuator commands versus DIC trigger commands; (bottom) actuator/LVDT displacements versus DIC displacements over time.

3.2.3 Calibration of Deflections for Notched Beam Fatigue Testing

Based on elastic beam deflection calculation methods, such as double integration or energy (Castigliano's theorem), the deflection at the center of a beam under four-point bending beam loading is 1.15 times greater than the deflection at the loading points (two points on the specimen, distance *a* from both ends). The current loading system at NCSU measures the displacement at the loading point using an actuator LVDT. Several connections and bearings must be set up before the specimen experiences the load, which raises the question of whether the cited difference between four- and two-point loading remains valid, as machine compliance might cause additional deformations. Therefore, the NCSU research team decided to use an on-specimen LVDT that measures the deflection at the neutral axis. The displacements measured using the on-specimen LVDT and the actuator LVDT were compared to the DIC system measurements to establish a relationship between the applied and measured displacements.

Also, a closed-loop system that could control the loading based on the on-specimen deflections would be useful for these types of tests. The current MTS system at NCSU, shown in Figure 3-15, does not support an add-on to configure the on-specimen displacement-controlled test. Hence, the NCSU team independently measured the on-specimen deflections and loads using an LVDT and load cell. The two main reasons for undertaking this work are that (1) most laboratories do not have an on-specimen controlled actuator loading system, so a method that a larger user group could use would be welcome, and (2) the current MTS actuator capacity at NCSU is 100 kN (22,000 lb) and has a maximum displacement range of 200 mm (7.87 in.). Controlling the actuator to accommodate a displacement that is less than a millimeter using a 150-kN capacity closed-loop system would cause a surge in loading and eventually lead to sudden specimen failure. Therefore, an actuator displacement control test would be ideal for avoiding catastrophic specimen failure. Also, an on-specimen LVDT and load cell can provide accurate displacement and load measurements, respectively.

Figure 3-15. Four-point bending beam test apparatus housed in MTS.

The calibration process was designed to accommodate the deflection ranges from the lowest to highest expected tensile strain levels (250 μ - 2000 μ) during the NBFTs. The calibration phase is composed of five stages, ranging from 250 μ, 500 μ, 1000 μ, 1500 μ, and 2000 μ tensile strain. The corresponding theoretical deflections were back-calculated to find 0.105 mm, 0.215 mm, 0.425 mm, 0.64 mm, and 0.85 mm, respectively. For each stage, 100 cycles of respective deflections were applied via actuator displacement, as shown in Figure 3-16. The rest periods between the two stages were fixed at two and three seconds.

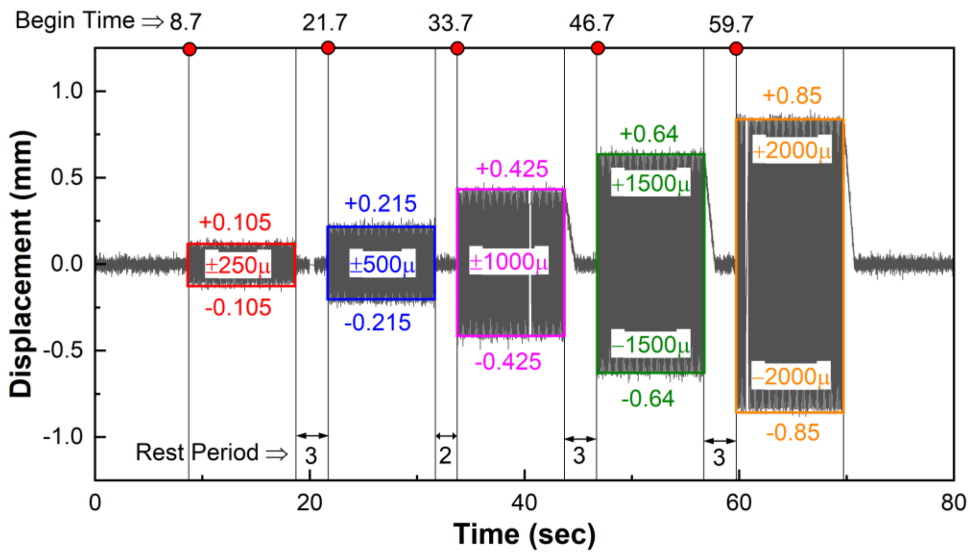

Figure 3-16. Five stages of displacement calibration.

LabVIEW logging software was employed to capture the displacements and loads. The deflections measured from the actuator and on-specimen LVDTs at different stages were used to calculate the tensile strain values. The data logging was configured to capture 1000 data points per second, i.e., 100 data points per cycle for the 10 Hz test. These data points must be fitted with a sinusoidal waveform to measure the amplitudes accurately. This fitting procedure is described in Appendix C. The described fitting procedure was used to measure the tensile strain that was recorded during each stage. Figure 3-17 (a) through (e) show the data noise and fitted lines for each of the five calibration stages, respectively. Two major observations can be made from Figure 3-17. First, the noise of the data points from the actuator is high at the lower tensile strain values of 250 μ (δ = 0.105 mm) and 500 μ (δ = 0.215 mm) whereas the on-specimen measurements at the same deflections remain smooth. The higher noise level for the actuator measurements of the smaller deflections can be attributed to the wide measurement range of the actuator LVDT. Second, the on-specimen tensile strain measurements are lower than the actuator-based tensile strain measurements, which indicates system compliance with regard to the displacement measurements.

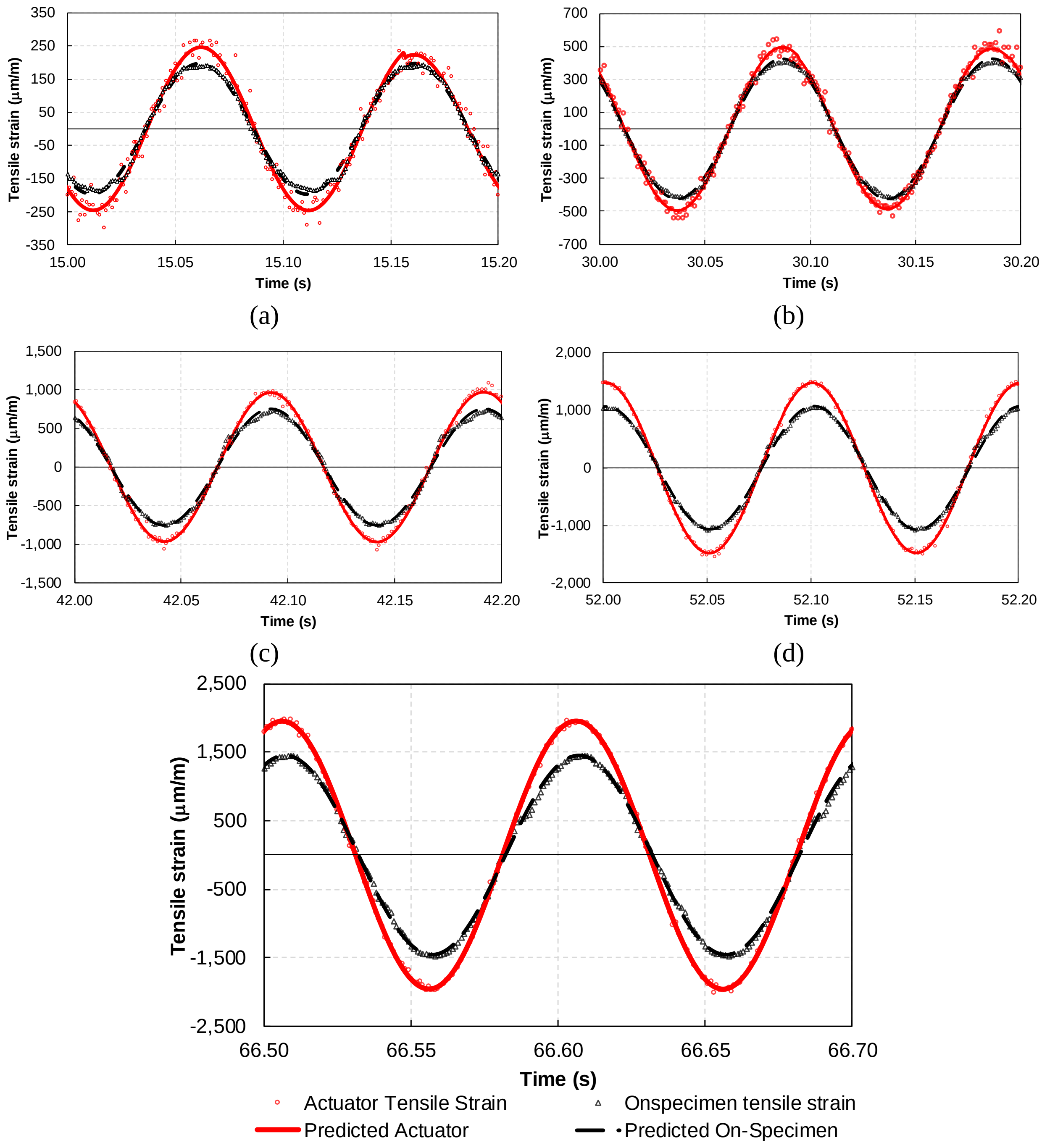

Figure 3-17. Tensile strain data points and curve fits for various actuator tensile strain input commands: (a) 250 μ, (b) 500 μ, (c) 1000 μ, (d) 1500 μ, and (e) 2000 μ.

Given these observations, relationships between the tensile strain that is based on the actuator input command and the tensile strain that is based on the measured actuator and on-specimen displacements could be established, as shown in Figure 3-18.

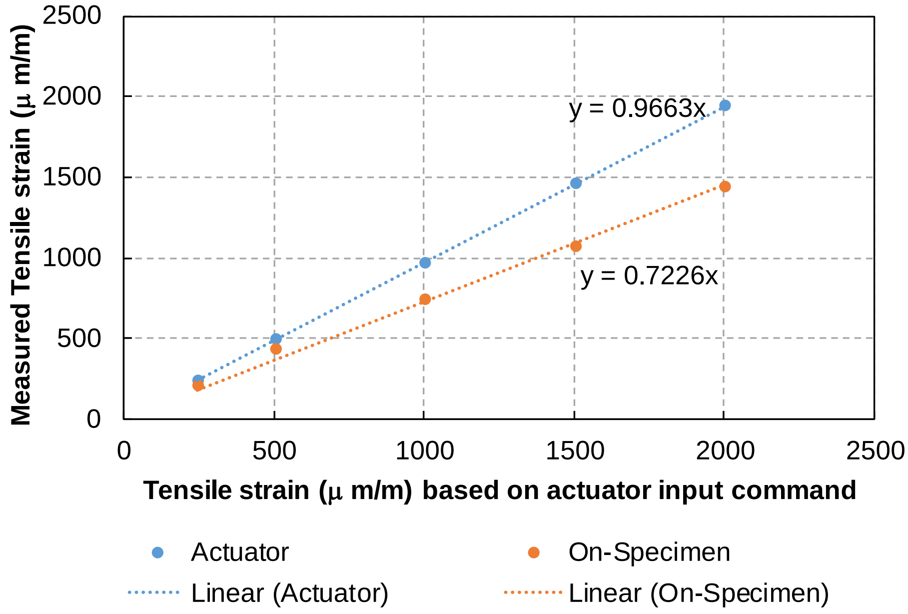

Figure 3-18. Relationship between tensile strain based on input commands and tensile strain based on measured actuator and on-specimen displacements.

The relationship shown in Figure 3-18 clearly indicates that only 72% of the input command displacement is reflected in the specimen deflection. Hence, the research team highly recommends that any laboratory should establish its own compliance-displacement relationship for the specific mixture of interest at a specific temperature so that the expected initial tensile strain can be predicted during the test. This exercise is essential, as system compliance varies among different laboratories. For the study mixture, RS9.5C, at room temperature, Table 3-2 presents the predicted tensile strain values that fit most of the tensile strain levels of the current project. Note that this compliance-displacement relationship remains valid only during the initial few cycles prior to damage initiation. Once the stiffness of the mixture degrades, the relationship for the current set-up does not remain valid. Therefore, the on-specimen deflections should be measured throughout the test for accuracy.

Table 3-2. Predicted On-Specimen Tensile Strain Based on Compliance-Displacement Relationship for the Study RS9.5C Mixture

Actuator input deflection (mm)	Predicted on-specimen deflection (mm)	Predicted actuator tensile strain (μm/m)	Predicted on-specimen tensile strain (μm/m)
1.043	0.754	2006	1500
0.835	0.603	1605	1200
0.626	0.452	1204	900
0.417	0.302	802	600
0.209	0.151	401	300
0.104	0.075	201	150

Chapter 4. Numerical Simulations of Pavement Responses

This chapter describes research efforts to simulate pavements with varying thicknesses and moduli values using a three-dimensional linear elastic finite element software program. The primary objective of this task is to predict the tensile strain underneath the asphalt overlay using FWD deflections obtained from existing pavements. This predictive methodology is necessary because FWD testing is performed on existing pavements prior to the overlay construction and the critical parameter for the performance prediction of asphalt overlay is the tensile strain at the bottom of the overlay.

4.1 Parameters Used in EverstressFE Simulations

EverstressFE is a 3-D linear elastic finite element software that can run pavement response analysis in batch mode. The advantage of EverstressFE over FlexPAVE™ is that an Excel VBA code is sufficient to create numerous combinations of structural and material input files. Moreover, a VBA code can easily extract the analyzed test results from the EverstressFE output file. Also, linear elastic pavement response analysis is common in the pavement community; therefore, a predictive equation that is based on linear elastic analysis can be easily verified.

4.1.1 Structure Information and Material Parameters

The pavement responses of standard structures with an overlay and surface, base, and subgrade layers were simulated using EverstressFE by combining various thicknesses and moduli values (~1500 combinations). Table 4-1 presents the material parameters and structural conditions considered for this study. Note that the aggregate base course thickness was fixed at 203.2 mm (8 in.) while the subgrade was assumed as semi-infinite by providing a large depth of 300 mm (118 in.). The thicknesses of the existing AC surface layer and overlay were varied to accommodate different pavement designs for various field conditions. The modulus values were varied to mimic various damaged and aged conditions of different layers in the field. Poisson's ratios (υ) of the asphalt, unbound, and subgrade layers were assumed as 0.35, 0.40, and 0.45, respectively. All the layers were considered to be fully bonded. Eventually, the outcome of nearly 1500 combinations helped to develop a predictive equation to measure the tensile strain underneath the newly constructed overlay, based on FWD measurements of the existing damaged/aged pavement.

Table 4-1. Pavement Simulation Conditions Using EverstressFE

$E_{overlay}$	**psi**	500,000				
	MPa	3,447				
$T_{overlay}$	**in. (mm)**	1.5 (38.1), 3 (76.2), 4 (101.6)				
E_{ac}	**psi**	700,000	500,000	300,000	100,000	50,000
	MPa	4,826	3,447	2,068	689	345
T_{ac}	**in. (mm)**	4 (101.6), 7 (177.8), 10 (25.4)				
E_{abc}	**psi**	50,000	40,000	30,000	20,000	10,000
	MPa	345	276	207	138	69
T_{abc}	**in. (mm)**	8 (203.2)				
E_{sg}	**psi**	20,000	15,000	10,000	5,000	2,500

	MPa	138	103	69	34	17
T_{sg}	**in. (mm)**	Semi-infinite 118 (300)				

Note: $E_{overlay}$ is overlay modulus; $T_{overlay}$ is overlay thickness; E_{ac} is asphalt concrete layer modulus; T_{ac} is asphalt concrete layer thickness; E_{abc} is aggregate base course modulus; T_{abc} is aggregate base course thickness; E_{sg} is subgrade modulus, and T_{sg} is subgrade thickness.

4.1.2 Climate Data

EverstressFE pavement response analysis is a linear elastic analysis. The input modulus value was determined at a representative condition (damaged or aged or both) of the pavement at 23°C.

4.1.3 Tire Load and Configuration

Two main types of structures were assumed for the study to analyze pavement responses, and the loading condition differs for each type. The first type is a structure without an overlay, shown on the left side of Figure 4-1, where FWD testing was expected to be carried out. However, in EvestressFE, the load parameters are wheel type, axle type, tire contact, and tire pressure. Hence, the load conditions were identified to fit the FWD load of 40 kN (9000 lb) applied through a loading plate with a diameter of 600 mm (12 in.). Thus, a 'single tire' wheel type in a 'single' axle with an applied tire load of 40 kN and tire pressure of 565 kPa that leaves a 'circular' imprint on the pavement was assumed for this study. The second type of structure is an overlay structure, illustrated on the right side of Figure 4-2, which was used to measure the tensile strain underneath the overlay (at the interface). The load parameters are applied through a single wheel and single axle. The load on the tire is 40 kN, and the tire pressure is 827 kPa. The tire contact shape is rectangular, with a tire width of 175 mm.

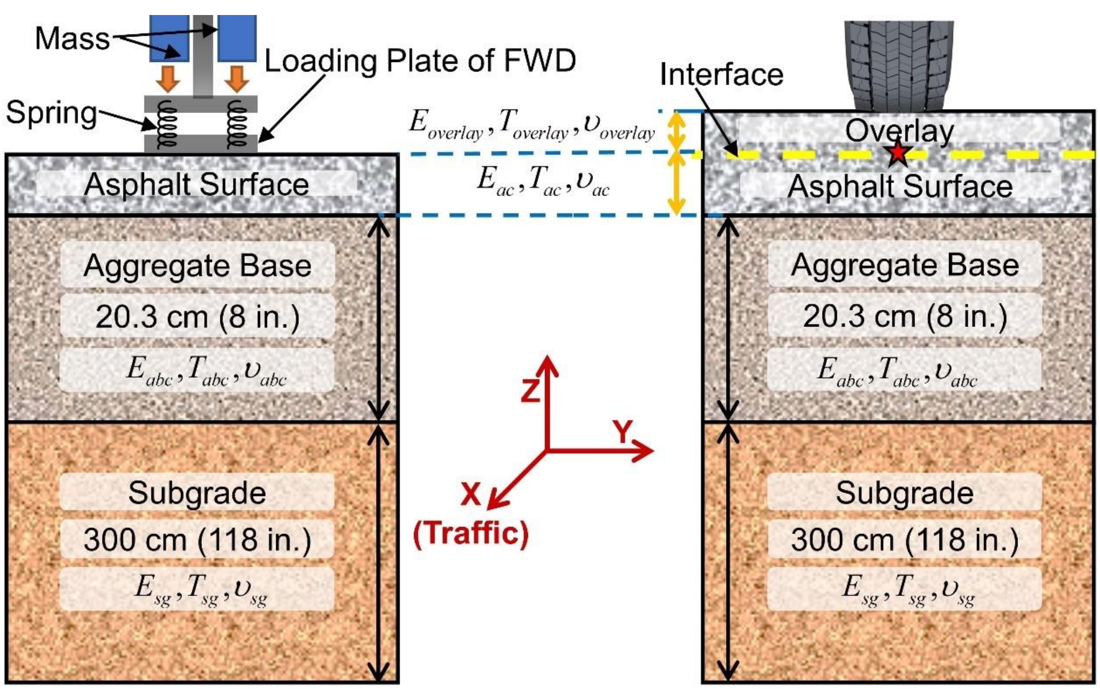

Figure 4-1. Pavement structures used to analyze pavement responses: (left) without overlay and (right) with overlay.

4.2 EverstressFE Analysis Output

The outputs measured for the two types of pavement structure differ due to the difference in the analysis requirements. The output of the structure without an overlay includes only the deflection measurements on the pavement surface that was subjected to FWD loading. The deflection points were measured at 0 in., 8 in., 12 in., 18 in., 24 in., 36 in., and 48 in. from the loading center. Figure 4-2 shows typical deflection bowl and deflection measurement points for the structure without an overlay. Similarly, Figure 4-3 and Figure 4-4 show the difference in the deflection bowl due to changes in the surface layer thickness and modulus, respectively. As expected, with an increase in AC thickness or modulus value, the deflections are reduced by keeping the other structural and material parameters constant.

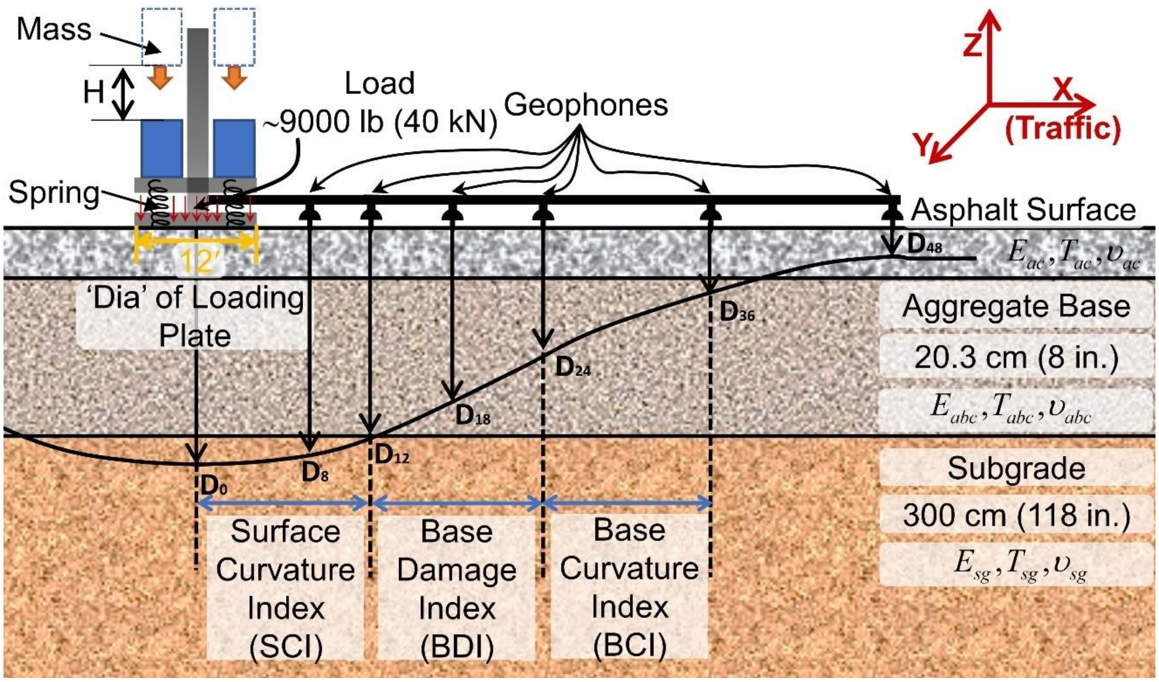

Figure 4-2. Typical FWD deflection bowl and measurement points.

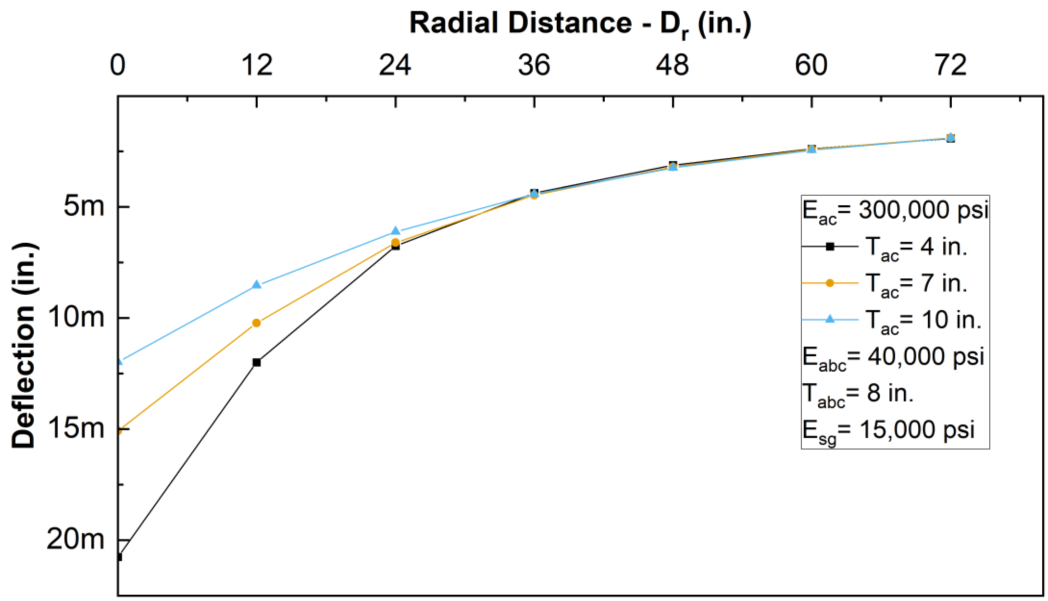

Figure 4-3. FWD deflection bowl with changes in asphalt concrete surface layer thickness.

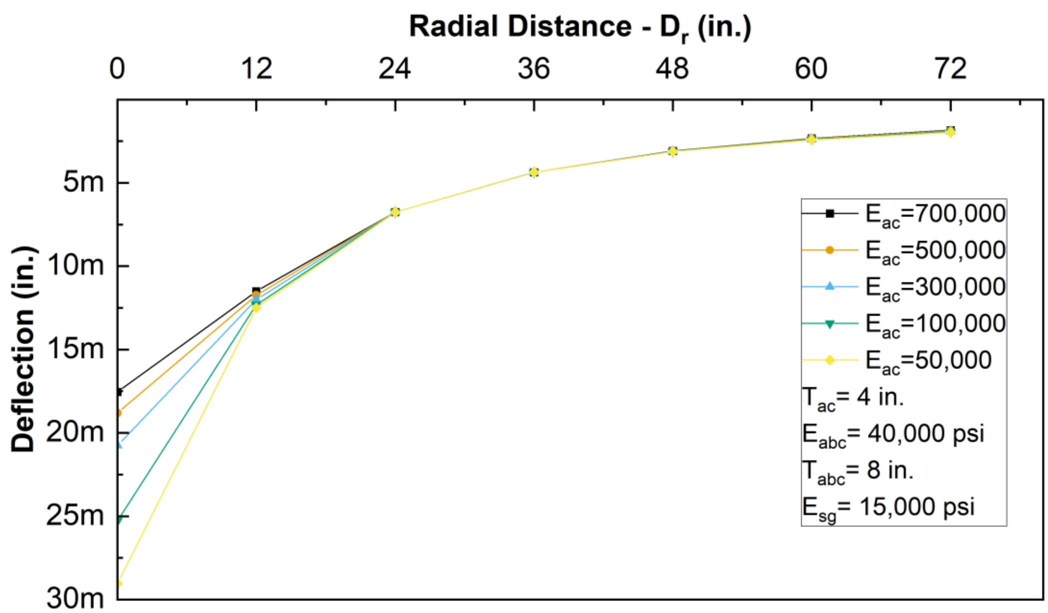

Figure 4-4. FWD deflection bowl with changes in asphalt concrete surface layer modulus.

The second type of structure, the structure with an overlay, was used to determine the tensile strain underneath the overlay. Before overlay simulations were conducted, there were three different structures analyzed without overlays during FWD simulations. For tensile strain measurement, each of these three structures was then simulated with overlays of varying thicknesses: 1.5 inches, 3 inches, and 4 inches. Therefore, three tensile strain values were determined for three overlay thicknesses on top of one existing pavement, which yielded one set of FWD deflections from the first set of simulations. Figure 4-5 and Figure 4-6 present the thicknesses and modulus values, respectively, for such a set of simulations of structures with overlays. The results indicate that the thickness and modulus of the overlay have a more significant influence on the tensile strain measured at the interface than the thickness and modulus of the existing pavement layer.

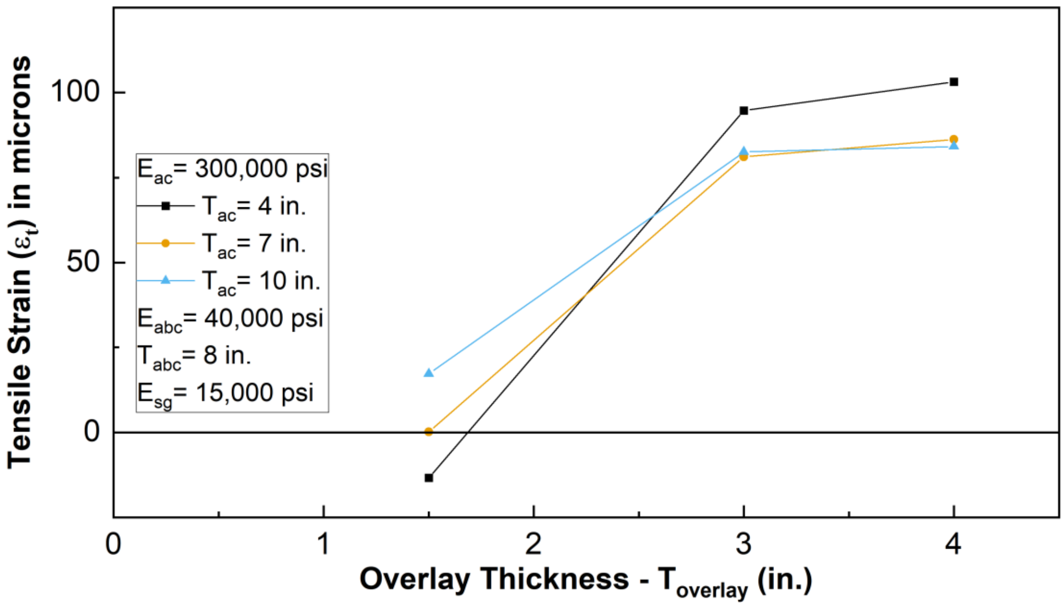

Figure 4-5. Tensile strain computed for various overlay thicknesses and asphalt concrete thicknesses of existing surface layer.

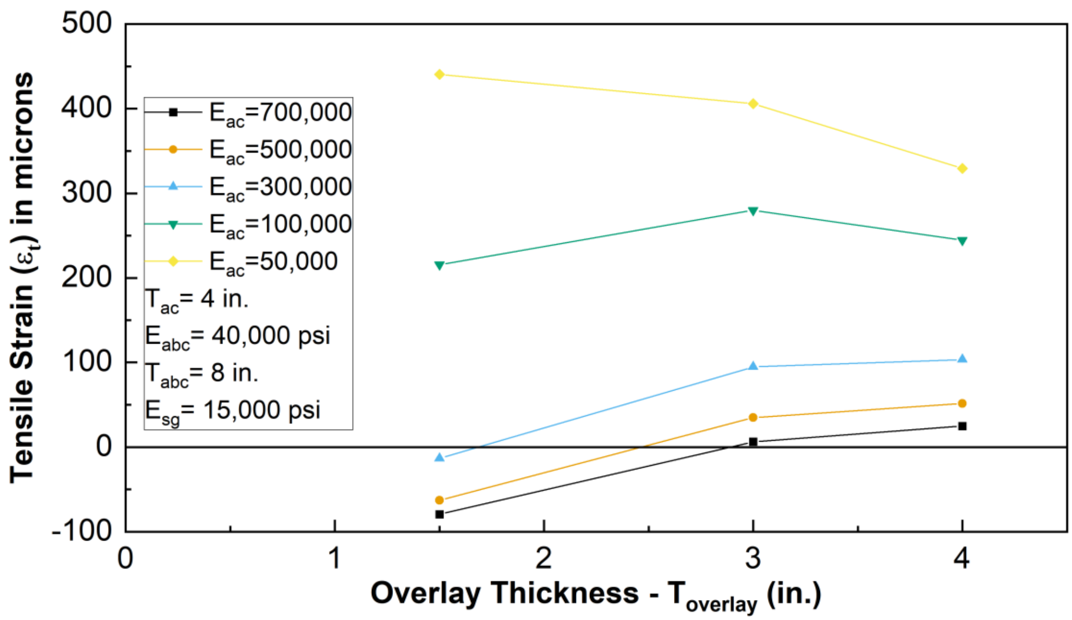

Figure 4-6. Tensile strain computed for various overlay thicknesses and varying asphalt concrete modulus values of existing surface layer.

Chapter 5. Field Distress Evaluation

5.1 NCDOT Interlayer Projects

The NCDOT provided details to the NCSU research team regarding in-service pavement sections constructed using geosynthetic interlayers. Table 5-1 shows the geosynthetic designations and corresponding NCDOT geosynthetic type as well as the number of in-service NCDOT projects for each type. A preliminary review of the data indicated that NCDOT geosynthetic interlayer projects date back to 2013. After a detailed investigation of the PMS data for the selected pavements, the NCSU research team selected five routes for this study. The following sections describe the selection process.

Table 5-1. NCDOT Special Provision for Geosynthetic Types and Designations

RP 2019-19 Designations	NCDOT Special Provision Type	No. of Projects
PM	Paving Mat Type I	1
-	Paving Mat Type II	3
PC#1	Composite Paving Grid Type III	10
PC#2	Composite Paving Grid Type II	3
PaG	Paving Grid Type II	0
PF	Paving Fabric Type II	1

Terminology

- Route: A designated roadway that connects one location to another and is identified by a unique number assigned by the NCDOT.
- MP (Mile Post): A marker that aids in identifying a location within a route.
- Section: A portion of the geosynthetic-reinforced roadway that has been subdivided based on the pavement structure, with each section being at least 0.1 miles long to match the availability and resolution of the automated distress data.

The research team chose twenty projects across North Carolina that had pavements reinforced with four types of geosynthetics: PC#1 (Paving Composite), PC#2 (Paving Composite), PM (Paving Mat), and Paving Fabric (PF). Notably, Paving Grid (PaG) was not used for any of the selected sections. Also, the PF section was not long enough to conduct a distress evaluation. To ensure that the selection process was fair and comparable, the routes were filtered based on the following specific criteria:

1. Date of completion (DOC): The completion date of pavement construction is within a year of the construction start date.
2. Route type: The route is designated as either a U.S. or NC route.
3. Construction method: The overlay is constructed via mill and fill.

4. Pavement structure: The pavement structure should be identical or comparable within the route.

Based on these criteria, the research team selected five routes for the project, described below. Figures that describe each route's section layout and location and provide distress data follow the route descriptions.

Route 20000264, Beaufort Co., PC#2

Figure 5-1 and Figure 5-2 respectively show the layout and distress details of Route 20000264 in Beaufort County. Comparisons and details of the different sections along the route are as follows:

- Sections 1, 2, and 6 had similar transverse crack conditions before the DOC of the overlay. However, all sections exhibited dissimilar performance. Hence, ISS testing possibly could help determine the effect of bond strength on the geosynthetics' performance.

- Section 7, compared to Sections 1, 2, and 6, had severe cracks in 2022. Hence, existing pavement FWD and ISS test data could help identify the factors that contributed to the geosynthetics' poor performance.

- Sections 6 and 7 showed delamination prior to the overlay construction. Hence, the effect of delamination could be studied using the ISS test.

- Sections 1 and 2 had similar pavement layer types and thicknesses for the top two layers. Sections 6 and 7 also had similar features. Therefore, both pairs could be compared to determine the effects of the pavement structure on the geosynthetics' performance.

Route 20000117, Pender Co., PC#1

Figure 5-3 and Figure 5-4 respectively present the layout and distress details of Route 20000117 in Pender County. Comparisons and details of the different sections along the route are as follows:

- Sections 1, 2, and 3 had similar transverse crack conditions before the DOC of the overlay. However, all sections exhibited dissimilar performance. Hence, ISS testing possibly could help determine the effect of bond strength on the geosynthetics' performance.

- Sections 1 through 6 had similar pavement layer types and thicknesses. However, all sections exhibited dissimilar performance. Hence, the current distress data could be compared to determine the contributing factors for the geosynthetics' performance.

- Section 1 is unreinforced, whereas Sections 2 through 6 are reinforced. Hence, comparing unreinforced and reinforced pavements could help determine the geosynthetic-reinforced pavement performance.

Route 20000701, Sampson Co., PM

Figure 5-7 and Figure 5-8 respectively present the layout and distress details of Route 20000701 in Sampson County. A comparison of the different sections along the route is as follows:

- Sections 3, 4, and 7 had similar transverse crack conditions before the DOC of the overlay. However, all sections exhibited dissimilar performance. Hence, ISS testing could help determine the effect of bond strength on performance. Note that Section 7 had not been reinforced. Comparing the unreinforced and reinforced pavements could help to determine the geosynthetic-reinforced pavement performance.

Route 39000024, Duplin Co., PM

Figure 5-5 and Figure 5-6 respectively present the layout and distress details of Route 39000024 in Duplin County. A comparison of the different sections along the route is as follows:

- Sections 3, 6, 10, and 13 had similar transverse crack conditions before the DOC of the overlay. In Section 1, the unreinforced section had a different transverse crack condition prior to the DOC of the overlay. Hence, comparing the unreinforced and reinforced sections and the ISS of cores from each section could help determine the reasons for the geosynthetic-reinforced pavement performance.

Route 29000017, Craven Co., PC#1

Figure 5-9 and Figure 5-10 respectively present the layout and distress details of Route 29000017 in Craven County. A comparison of the different sections on the route is as follows:

- Section 2 is unreinforced and Section 1 is reinforced. Hence, comparing the unreinforced and reinforced pavements could help determine the geosynthetic-reinforced pavement performance.

Figure 5-1. Section layout of Beaufort County Route 2000264007.

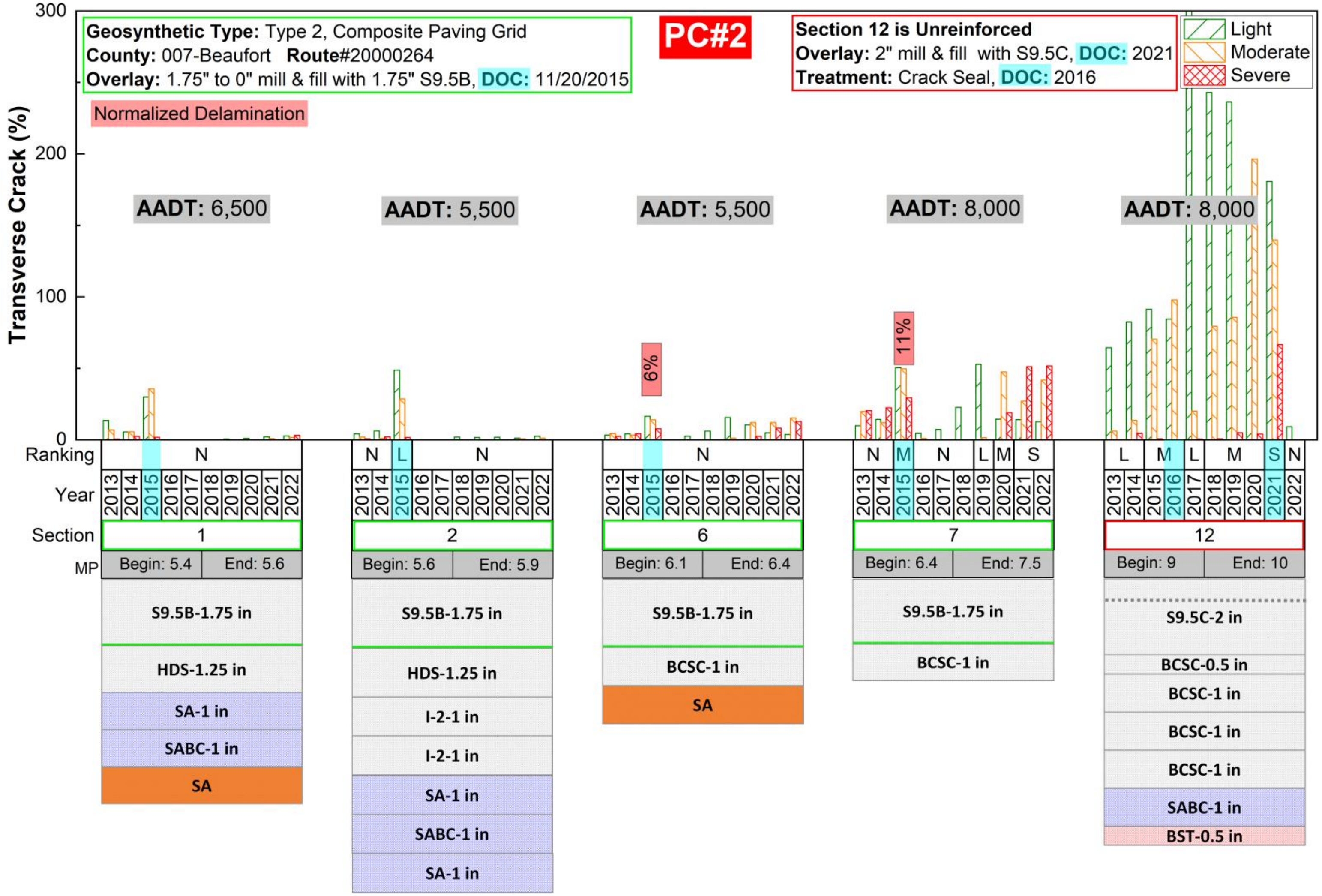

Figure 5-2. Distress data for Beaufort County Route 2000264007.

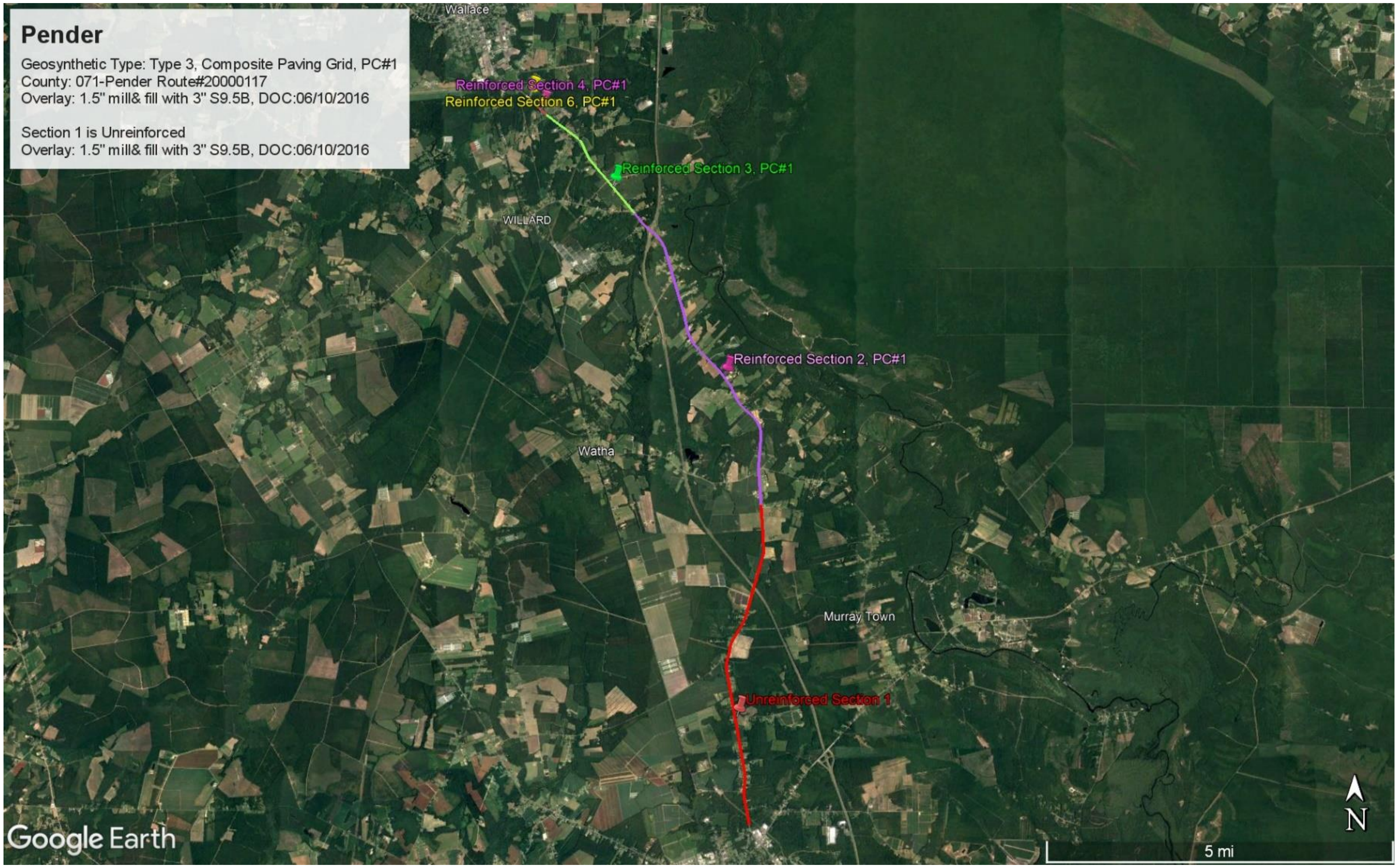

Figure 5-3. Section layout of Pender County Route 20000117071.

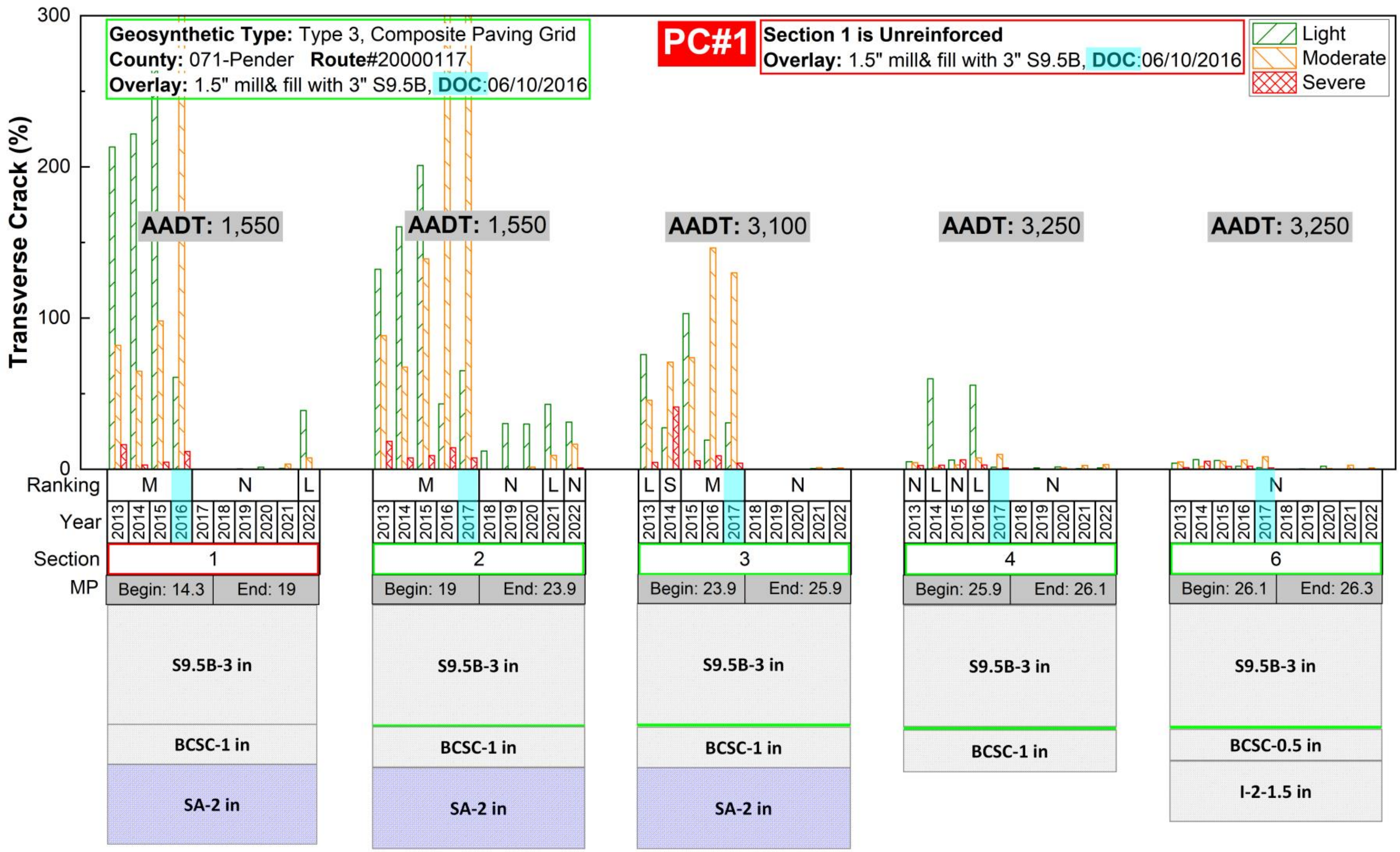

Figure 5-4. Distress data for Pender County Route 20000117071.

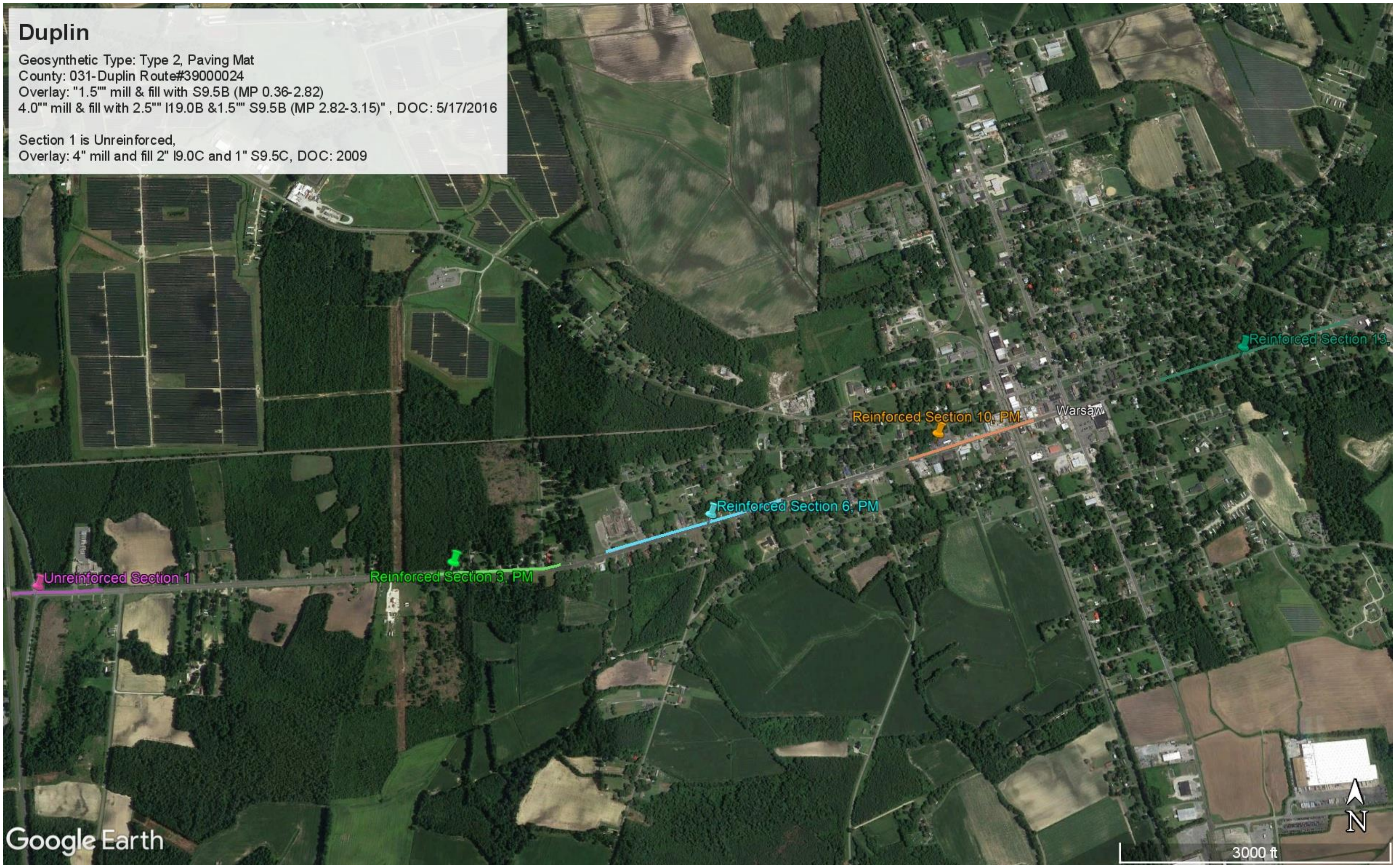

Figure 5-5. Section layout of Duplin County Route 39000024031.

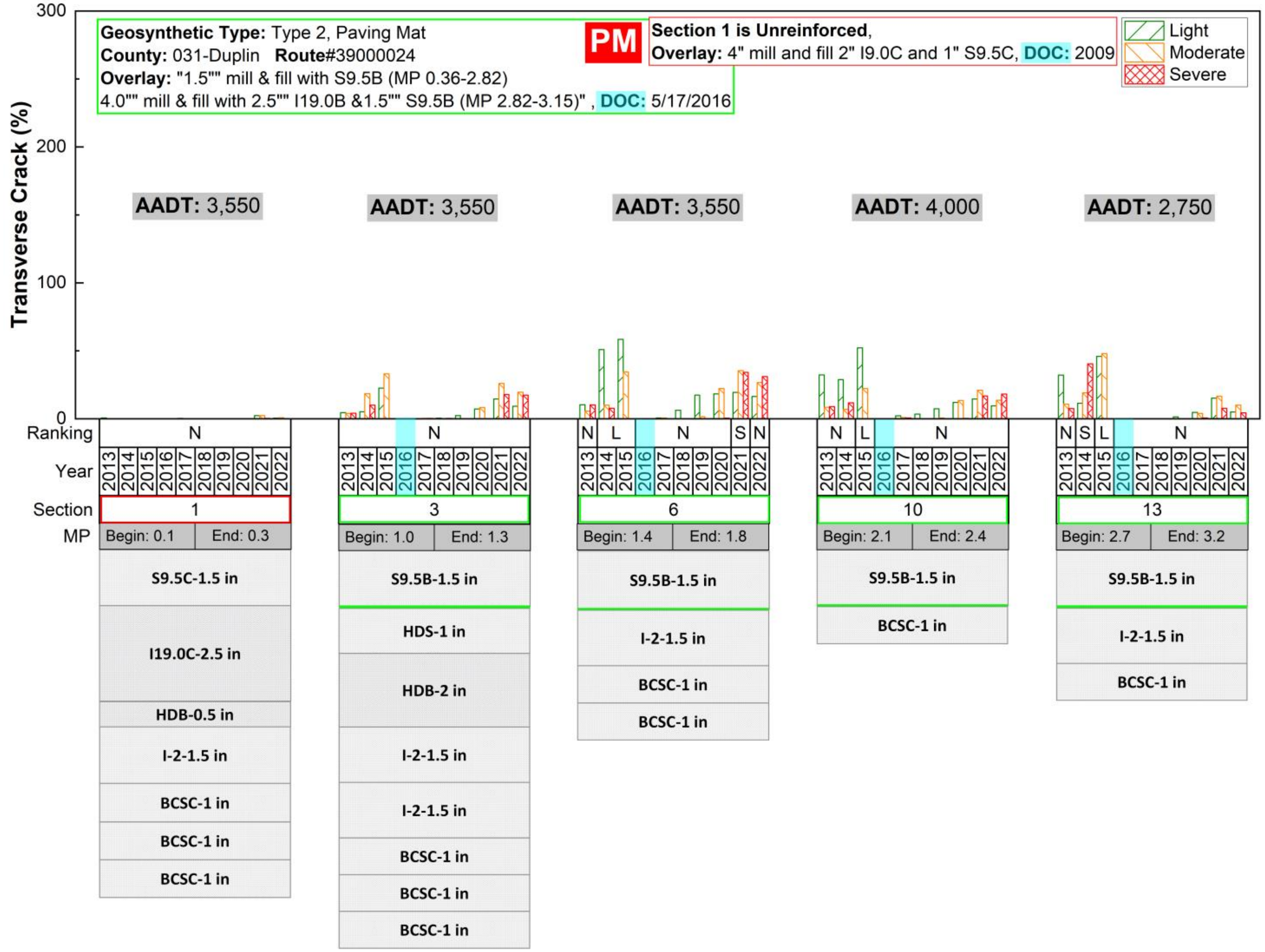

Figure 5-6. Distress data for Duplin County Route 39000024031.

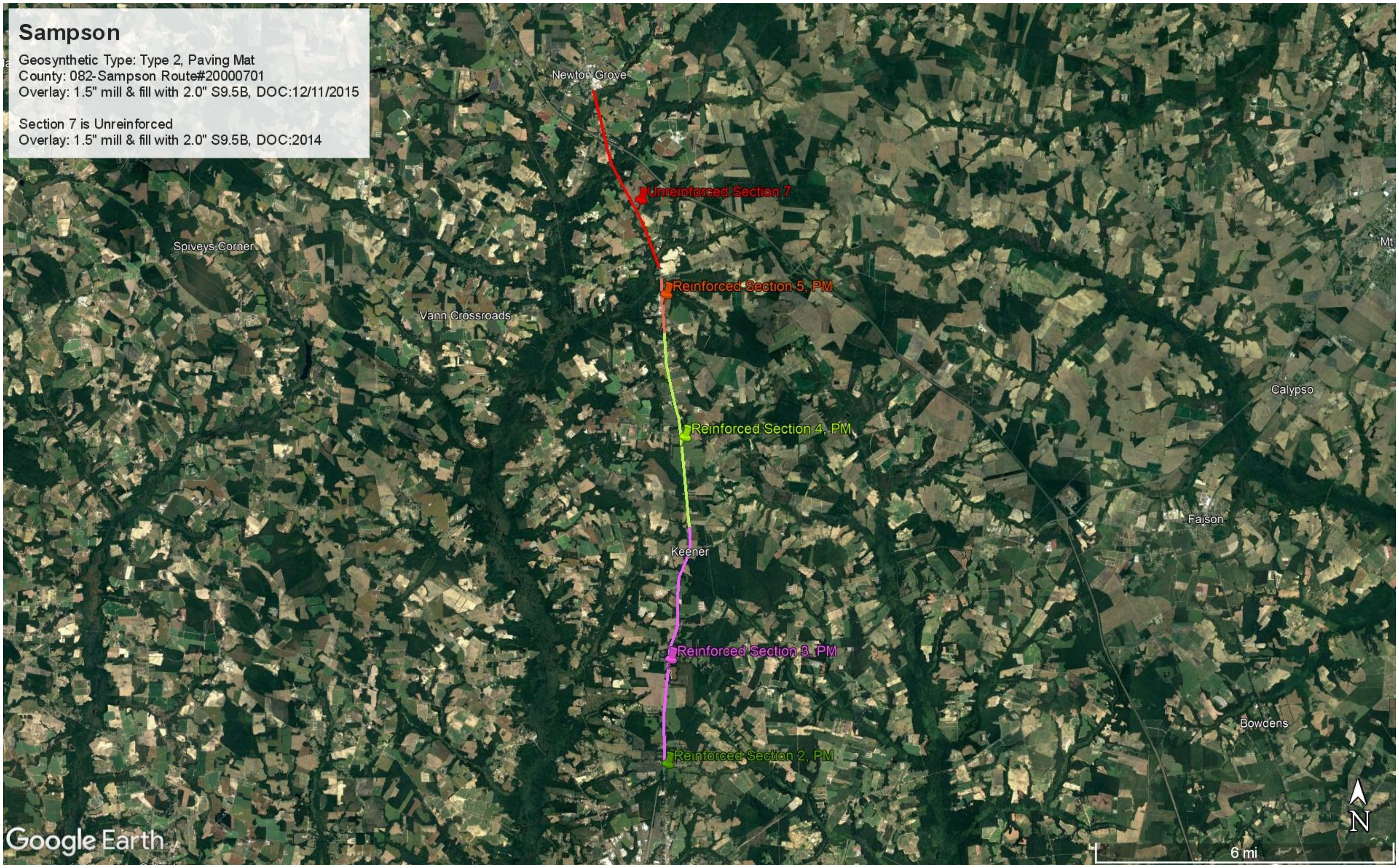

Figure 5-7. Section layout of Sampson County Route 20000701082.

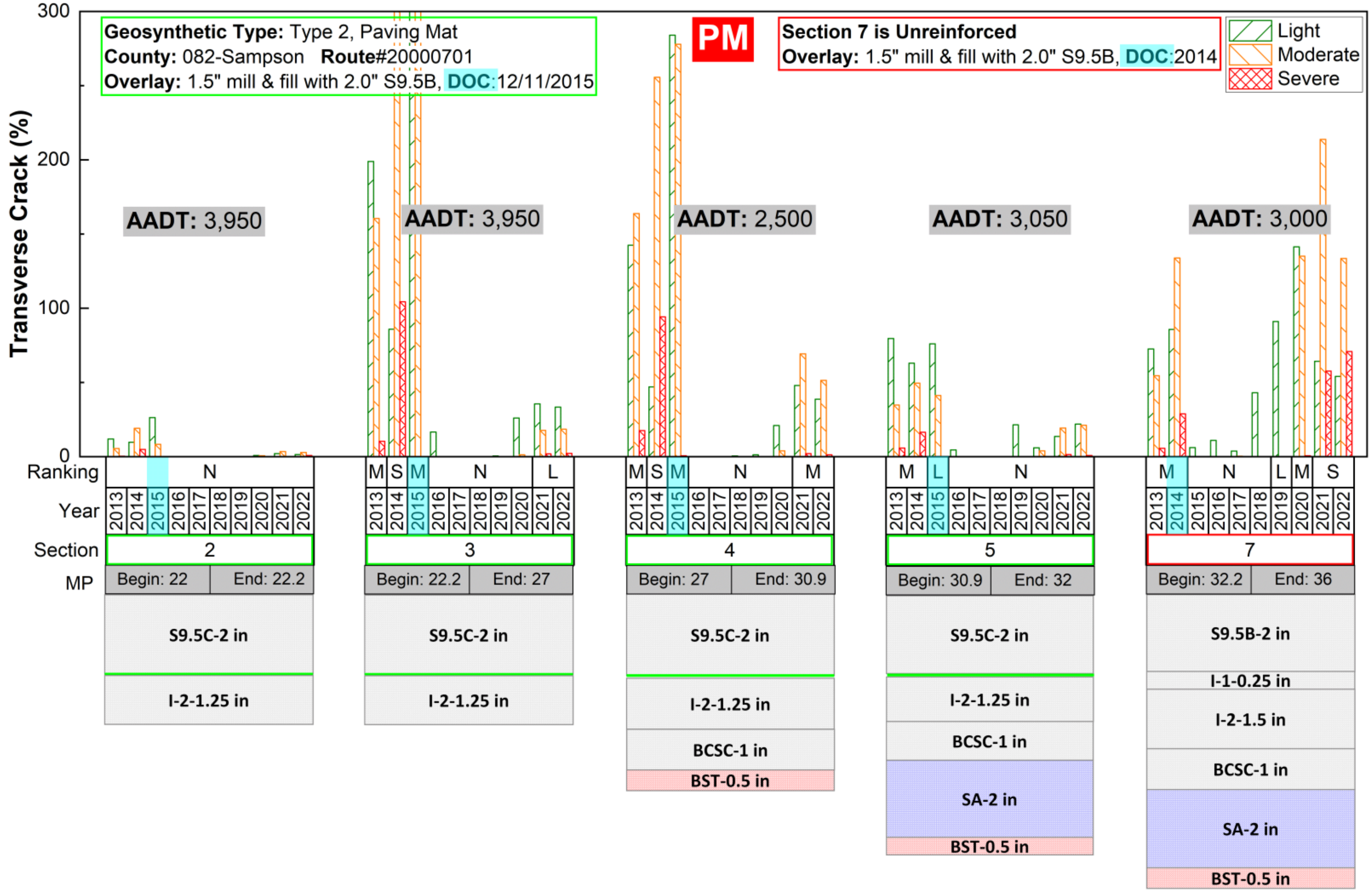

Figure 5-8. Distress data for Sampson County Route 20000701082.

Figure 5-9. Section layout of Craven County Route 29000017025.

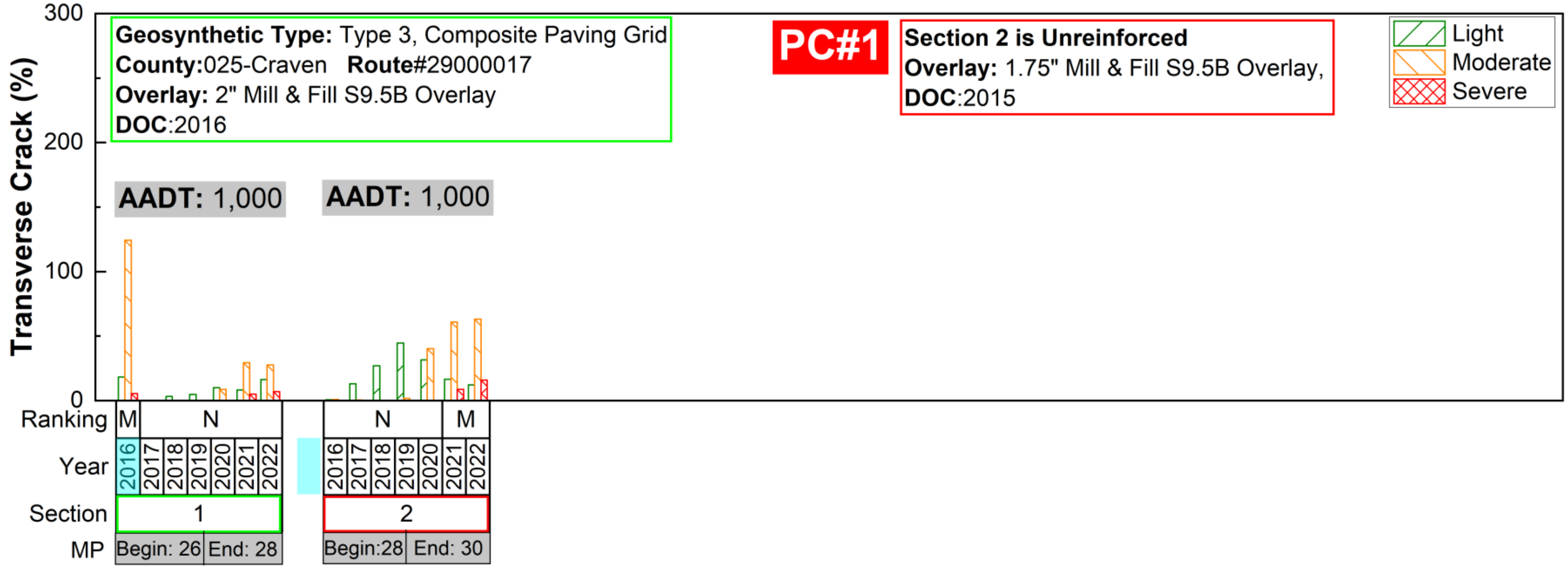

Figure 5-10. Distress data for Craven County Route 29000017025.

5.2 PMS Database Overview

Pavement Management Systems are software-driven methodologies and tools adopted by numerous transportation agencies to guide decision-makers in deriving cost-effective strategies to ensure that pavements remain serviceable. The data in a PMS are constituted from a blend of historical records, recurrent surveys, and inspections.

Different methods can be used for fatigue cracking percentage calculations. The four primary methods (discussed in Section 5.3) are the Corley method used by the NCDOT, the Federal Highway Administration's Performance-Related Specifications (FHWA-PRS) method, the Kansas Department of Transportation (KSDOT) method, and the Pavement Mechanical-Empirical (ME) method.

Table 5-2 shows the different fields available in the automated distress database of the NCDOT's PMS. Specific columns (or fields) in the PMS database are essential for calculating fatigue cracking percentages. The key fields are as follows.

Length, Lane Width, and Number of Lanes

- These parameters are fundamental to calculating the total lane area and total wheel area, which serve as the denominator in many of the fatigue calculation methods described below. These parameters are represented by 'Length,' 'Lane Width (ft),' and 'Number of Lanes' in the PMS data.

Alligator Cracking (Low, Moderate, High)

- Columns labeled 'Alligator Low (SF),' 'Alligator Mod (SF),' and 'Alligator High (SF)' denote the square footage of alligator cracks of low, moderate, and high severity, respectively. These values are essential for all four fatigue cracking calculation methods.

Longitudinal Cracking (Low, High)

- The 'Long. Low (LF)' and 'Long. High (LF)' columns capture the linear footage of low and high-severity longitudinal cracks, which are directly used in the FHWA-PRS, KSDOT, and Pavement ME methods.

Transverse Cracking (Low, Moderate, High)

- Columns 'Trans. Low (LF),' 'Trans. Mod (LF),' and 'Trans. High (LF)' represent the linear footage of transverse cracks of low, moderate, and high severity, respectively. They are utilized in the FHWA-PRS, KSDOT, and Pavement ME methods.

Date and Year

- The 'Date' and 'Year' columns might not directly influence the fatigue cracking percentage calculations. Still, they provide a timestamp that enables trend analyses over time and the tracking of the progression of pavement deterioration.

AADT:

- 'AADT' stands for annual average daily traffic, which represents the total traffic volume of a roadway over a year, divided by 365 days. Although AADT is not directly used in the cited calculation methods, it is a critical metric that impacts the rate of a pavement's wear and tear.

Pavement Type:

- The 'Pvmnt Type' column indicates the type of pavement material. Different materials may have distinct fatigue and cracking patterns. Although this field is not used directly in the cited calculation methods, understanding the pavement type is nonetheless crucial for more detailed pavement evaluations.

The remaining columns provide supplementary data about the location, administrative details, other distresses, and characteristics of the road segment. Although these data do not directly feed into the calculation of the fatigue cracking percentages using the methods outlined, they are valuable for a holistic understanding of the pavement's condition, its historical and current context, and for making informed maintenance and rehabilitation decisions. In essence, the PMS data provide a comprehensive overview of the pavement's state, allowing for both detailed calculations, such as the fatigue cracking percentage, and broader strategic planning for roadway maintenance and management.

Table 5-2. Fields Available in PMS Automated Distress Database

Fugro iVision URL	Fugro iVision Link
County	007-Beaufort
Route	20000264
Lane Direction	Increasing
Lane	1
Begin MP	7.50
To MP	7.60
Length	0.10
Date	2/27/2021
Year	2021
Card. Dir.	E
Number Of Lanes	4.00
Width	48.00
Lane Width (ft)	23.70
AADT	5000.00
Pvmnt Type	P
Alligator Low (SF)	259
Alligator Mod (SF)	2159
Alligator High (SF)	0
Trans. Low (LF)	85
Trans. Mod (LF)	205
Trans. High (LF)	216
Long. Low (LF)	130

Long. High (LF)	443
Left WP Rut (in)	0.48
Right WP Rut (in)	0.33
Max Avg Rut (in)	0.41
Ravel Low (SF)	0
Ravel Mod (SF)	0
Ravel High (SF)	0
Bleed Low (SF)	0
Bleed High (SF)	0
Non-WP Patch (SF)	0
WP Patch (SF)	0
Reflect Trans. Low (LF)	0
Reflect Trans. Mod (LF)	0
Reflect Trans. High (LF)	0
Delamination (SF)	0
Reflect Long. Low (LF)	0
Reflect Long. Mod (LF)	0
Reflect Long. High (LF)	0
Long. Lane Joint Low (LF)	0
Long. Lane Joint High (LF)	0
Left WP IRI	203
Right WP IRI	213
Avg Left/Right IRI	208.00
Collection Speed	36
System	US
NHS	
Tier ID	Regional
Functional Class	Principal Arterial (Other)
County Section Number	2
Latitude From	35.54712875
Latitude To	35.54716121
Longitude From	-77.0392974
Longitute To	-77.03752803
County Owner	02 /1 Beaufort Maint
District	02 Dist 1 Adm
Division	02 Div Adm
Statewide Owner	Highway Ops
Date Update	44579.41028
User Update	IMPORT(3522)

5.3 Verification Sections in US 1

The research team and NCDOT engineers collected cores, conducted FWD and Dynamic Cone Penetrometer (DCP) tests, and performed a pavement condition survey on US 1 sections at Moore County near Aberdeen on August 9, 2023. The data from these sections were used to verify the predictive procedure that was developed using the PMS data from the selected sections. Note that these sections were overlayed with different geosynthetic interlayer products during the NCDOT HWY-2012-02 project. A total of 16 cores were obtained, with four from each section. Due to the limitation in time and resources in the project, these cores were not tested in the study. These cores are stored at the NCSU pavement lab to ensure their preservation for potential future tests.

The team recorded Falling Weight Deflectometer (FWD) readings alongside the core extraction. These were taken at intervals of 100 feet. Additional FWD tests were conducted on the locations where the preoverlay cracks were present. The locations for the preoverlay cracks were determined from the detailed cracking maps that were developed during the HWY-2012-02 project. On average, 11 FWD readings were collected in each section.

The team also recorded DCP measurements to assess the aggregate base and subgrade conditions. The DCP tests were limited to one reading per section, resulting in four readings in total.

5.4 Fatigue Cracking Percentage Calculation Methods

Understanding the calculations of the total lane area and wheel path area is pivotal to a better understanding of the four fatigue cracking percentage methods (described respectively in Sections 5.3.1, 5.3.2, 5.3.3, and 5.3.4).

Total Lane Area

The total lane area represents the entire area of the evaluated lane segment. This parameter is essential for many cracking percentage calculation methods because it serves as the denominator when determining the percentage of the roadway that is affected by different distress types. Equation (5-1) is the calculation for the total lane area.

$$\text{Total Lane Area } (ft^2) = \text{Length } (mi) \times 5280\ (mi \Rightarrow ft) \times \text{ Lane Width } (ft) \times \text{No. of Lanes} \quad (5\text{-}1)$$

where

Length	=	length of the road segment under evaluation,
Lane Width	=	width of a single lane (standard widths vary by jurisdiction, but common values include 10, 11, or 12 feet), and
Number of Lanes	=	total number of lanes in the road segment.

Total Wheel Path Area

The wheel path area is crucial because most fatigue distress and other pavement distress types occur in areas where vehicles most frequently travel. Typically, two-wheel paths are considered for each lane: one for the left wheel and one for the right wheel. Equation (5-2) is the calculation for the total wheel path area for a specific lane segment.

$$\text{Total Wheel Path Area } (ft^2) = \text{Length } (mi) \times 5280 \ (mi \Rightarrow ft) \times \text{ Wheel Path Width } (ft) \times 2 \quad (5\text{-}2)$$

Typically, the wheel path width is considered as 3 ft to 3.5 ft, although it can vary. Multiplying by 2 accounts for the two-wheel paths in each lane.

With the knowledge obtained from the total lane area and wheel path area calculations, transportation agencies can better contextualize PMS data and the fatigue cracking percentages derived from the various methodologies. These foundational calculations are essential for understanding the extent and severity of the pavement distress and making informed maintenance and rehabilitation decisions.

5.4.1 NCDOT Cracking Percentage Calculation Using Corley Method

The Corley method used by the NCDOT determines the fatigue cracking percentage based on a weighted evaluation of low, moderate, and high severity alligator cracking. Equation (5-3) is the Corley method calculation.

$$FC(\%) = \left(\frac{5.9 \times \text{Low}(m^2) + 1.7 \times \text{Mod}(m^2) + 13.9 \times \text{High}(m^2)}{\text{Total Lane Area } (m^2)} \right) \quad (5\text{-}3)$$

where

FC = fatigue cracking and

Low, Mod, and High = square footage of alligator cracks of low, moderate, and high-severity, respectively.

The denominator, representing the total lane area, is derived from the length of the section, lane width, and number of lanes, as given in Equation (5-1).

5.4.2 Federal Highway Administration's Performance-Related Specifications Fatigue Cracking Percentage Calculation Method

The FHWA-PRS calculation method computes the fatigue cracking percentage as the cumulative alligator, longitudinal, and transverse cracking percentages. This method considers the square footage of alligator cracking and the linear footage of longitudinal and transverse cracks, converting them into percentages of the total lane area. Equations (5-4) through (5-8) describe the FHWA-PRS fatigue cracking percentage calculation method.

$$\text{AC Severity}\%[Low, Mod, High] = \frac{\text{Alligator Cracking}(SF)[Low, Mod, High]}{\text{Total Wheel Path}(SF)} \times 100 \quad (5\text{-}4)$$

$$AC\% = 40 \times \left(\frac{\%Low}{350} + \frac{\%Med}{200} + \frac{\%High}{75} \right) \quad (5\text{-}5)$$

$$LC\% = \frac{(Long.Low(LF) + Long.High(LF)) \times 1ft}{\text{Total Lane Area (SF)}} \times 100 \quad (5\text{-}6)$$

$$RC\% = \frac{(RC.Low(LF) + RC.Mod(LF) + RC.High(LF)) \times 1\,ft}{\text{Total Lane Area (SF)}} \times 100 \tag{5-7}$$

$$FC\% = AC\% + LC\% + RC\% \tag{5-8}$$

where

FC = fatigue cracking,
Low, Mod, and High = square footage of alligator cracks of low, moderate, and high severity, respectively,
AC% = alligator cracking,
LC% = longitudinal cracking, and
RC% = reflective cracking.

5.4.3 Kansas Department of Transportation (KSDOT) Cracking Percentage Calculation Method

Adopted by the KSDOT, this method calculates the alligator cracking percentage using a similar approach as the FHWA-PRS method but assigns distinct weights to the severity levels and considers the patched area. Equation (5-9) describes the KSDOT calculation method.

$$AC\% = \left(\frac{0.5 \times FCR_1 + 1.0 \times FCR_2 + 1.5 \times FCR_3 + 2.0 \times FCR_4}{8} \right) \tag{5-9}$$

where

FC_1 = hairline alligator cracking, pieces not removable,
FC_2 = alligator cracking, pieces not removable, cracks spalled,
FC_3 = alligator cracking, pieces are loose and removable, and pavement may pump, and
FC_4 = pavement has shoved, forming a ridge of material adjacent to the wheel path.

However, the PMS data available are assigned to the parameters FC_2 = AC_Low(%), FC_3 = AC_Mod(%), and FC_4 = AC_High(%). FC_1 is assumed to be zero. Then, the FC% is calculated using Equations (5-6), (5-7), and (5-8).

5.4.4 Pavement ME Cracking Percentage Calculation Method

The Pavement Mechanistic-Empirical (ME) method assesses fatigue cracking by calculating the percentages of alligator, longitudinal, and transverse cracks in relation to the total lane area. The individual percentages are aggregated to derive the overall fatigue cracking percentage. Equation (5-10) describes the Pavement ME calculation method.

$$AC\% = \frac{AC.Low(SF) + AC.Mod(SF) + AC.High(SF)}{\text{Total Lane Area (SF)}} \times 100 \tag{5-10}$$

Then, the FC% is calculated using Equations (5-6), (5-7), and (5-8).

Note: The Mechanical-Empirical Pavement Design Guide (MEPDG) predictions for load-related cracking are combined by adding the lengths of the longitudinal cracks and reflection cracks for hot mix asphalt overlays, multiplying by 1.0 ft, dividing that product by the lane area, and adding that value to the percentage of alligator cracking predicted by the MEPDG.

Although each calculation method offers a unique perspective, they all underscore the significance of grasping the severity and spread of cracking. Such insights can empower transportation agencies to make enlightened decisions concerning their roadway network maintenance, rehabilitation, and reconstruction.

Figure 5-11 compares the different crack percentage calculation methods against the Pavement ME crack percentage calculation method recommended by Applied Research Associates. Figure 5-11(a) shows that the data points for the FHWA PRS Method lie predominantly below the line of equality, indicating an underestimation of the crack percentages compared to the Pavement ME method. Figure 5-11(b) shows that the KSDOT data are closely aligned with the line of equality, suggesting a near-equitable estimation relative to the Pavement ME method. However, Figure 5-11(c), representing the NCDOT data, shows that most of the points lie below the line of equality, denoting an underestimation of crack percentages compared to the Pavement ME method. Among the datasets, the KSDOT method measurements seem to have the closest agreement with the Pavement ME method.

In this study, the Pavement ME crack percentage calculation method was selected to represent the field cracking percentage.

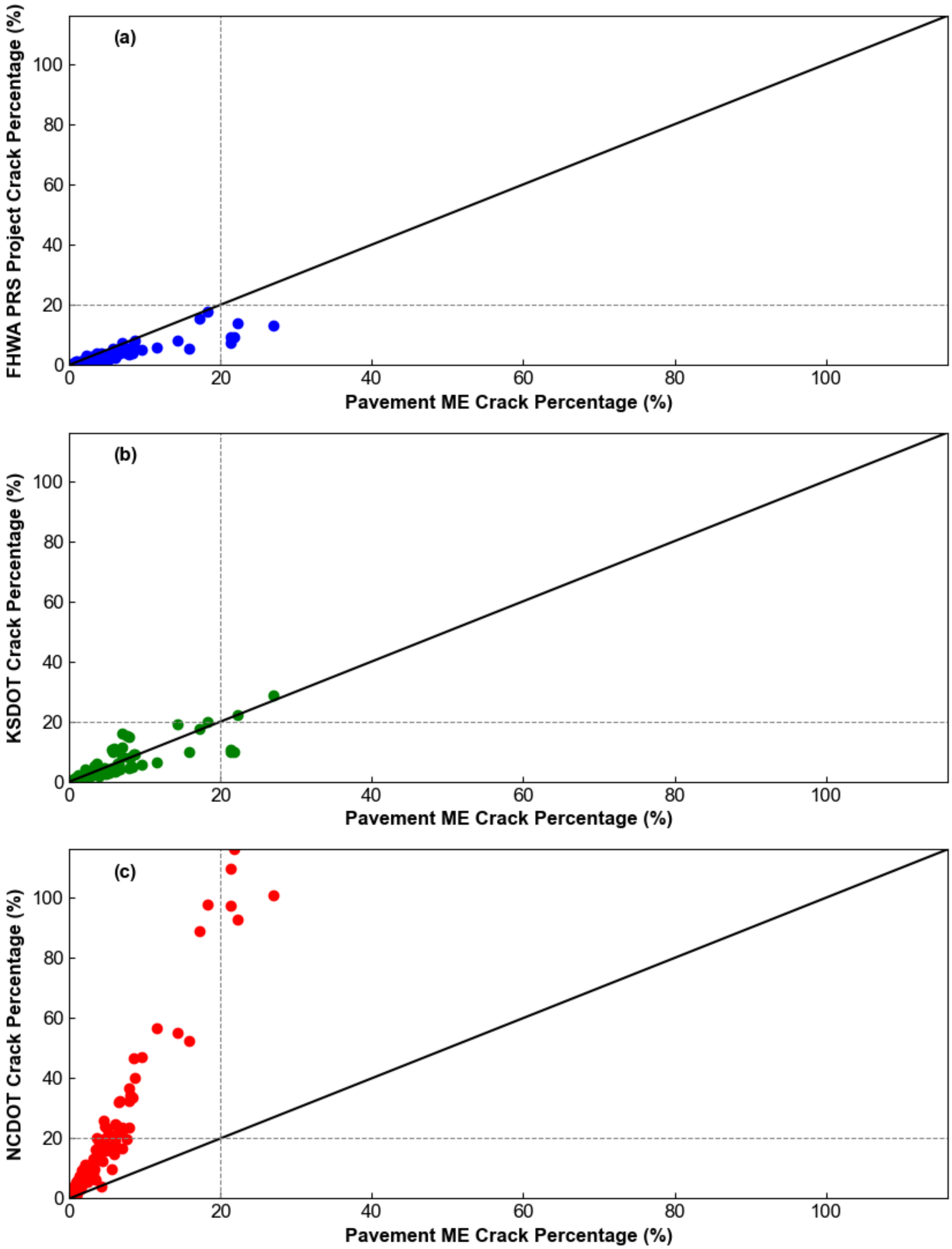

Figure 5-11. Comparison of three crack percentage calculation methods to Pavement ME crack percentage calculation method: (a) FHWA-PRS method, (b) KSDOT method, and (c) NCDOT (Corley) method.

Figure 5-12 through Figure 5-16 present variations in fatigue cracking percentages for different sections and reinforcements over the years, as assessed using the aforementioned fatigue cracking calculation methods. Collectively, the figures provide insights into the performance and durability of the road sections under study based on the different assessment techniques.

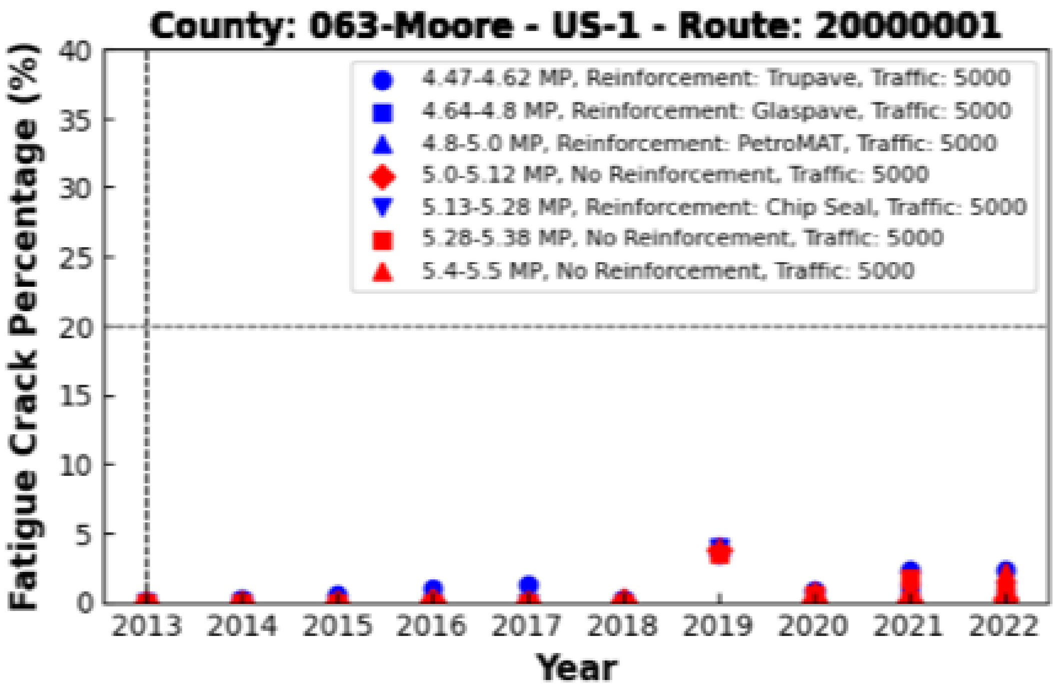

Figure 5-12. Total fatigue crack percentages by year for Moore County at Route 20000001.

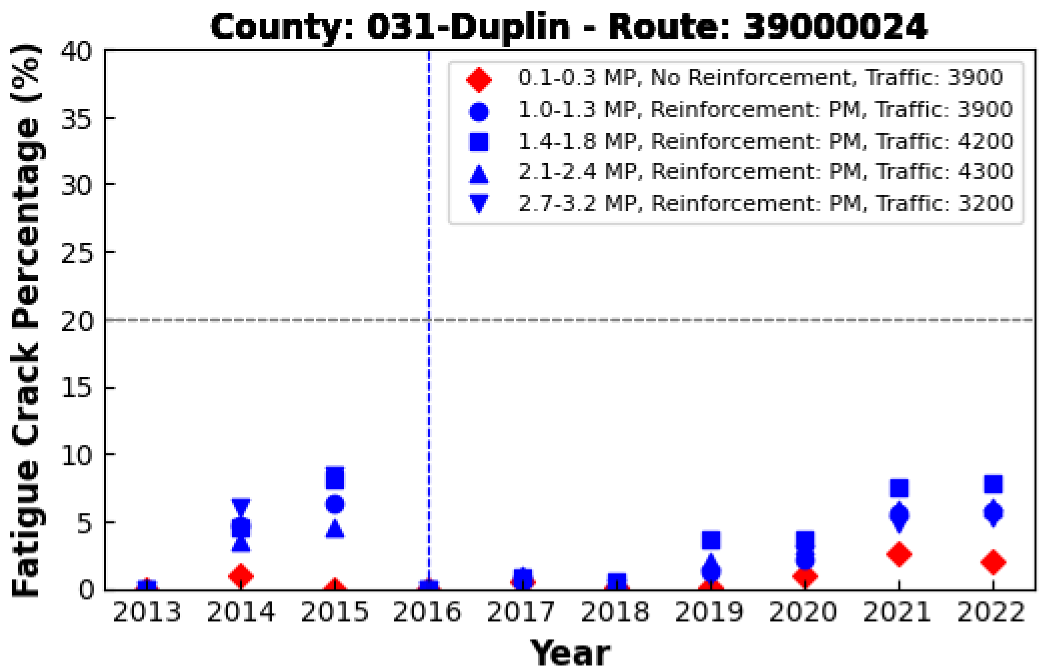

Figure 5-13. Total fatigue crack percentages by year for Duplin County at Route 39000024.

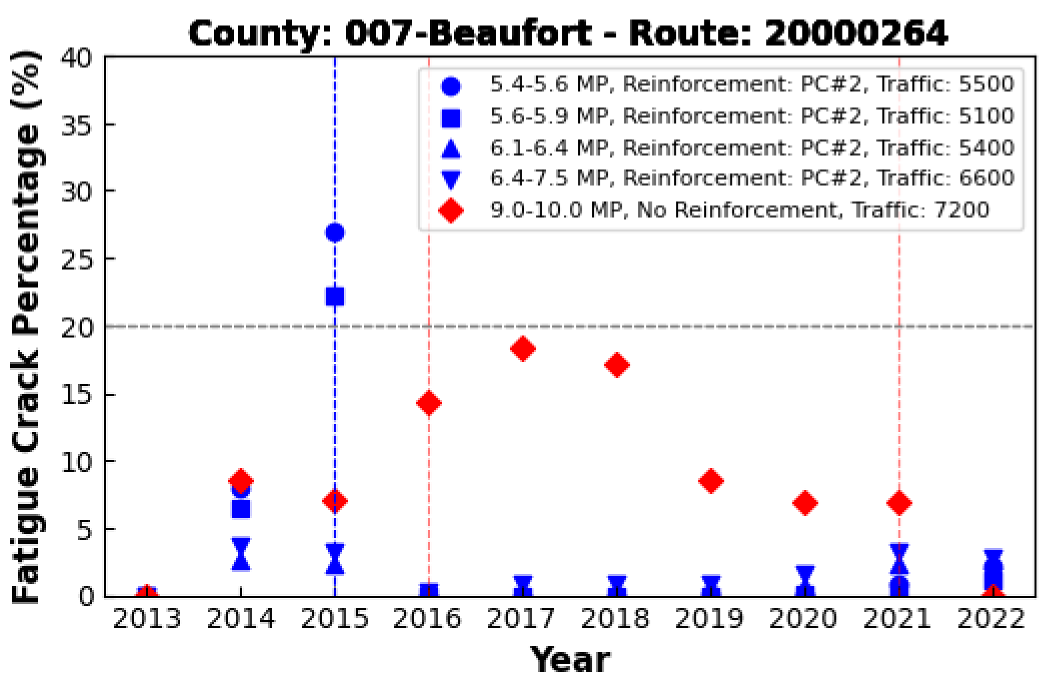

Figure 5-14. Total fatigue crack percentages by year for Beaufort County at Route 20000264.

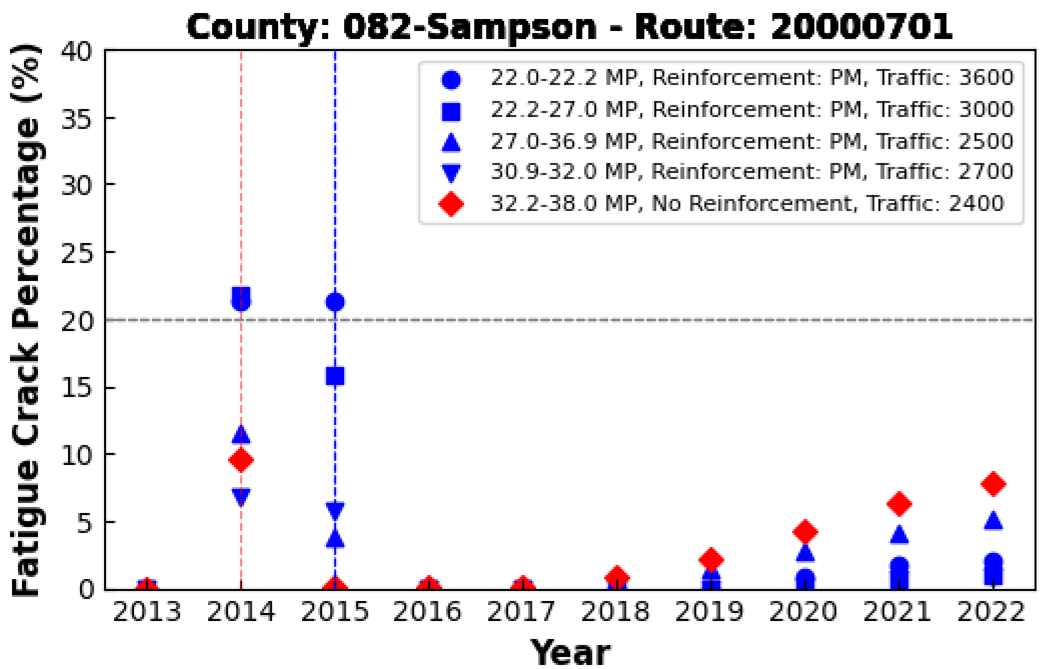

Figure 5-15. Total fatigue crack percentages by year for Sampson County at Route 20000701.

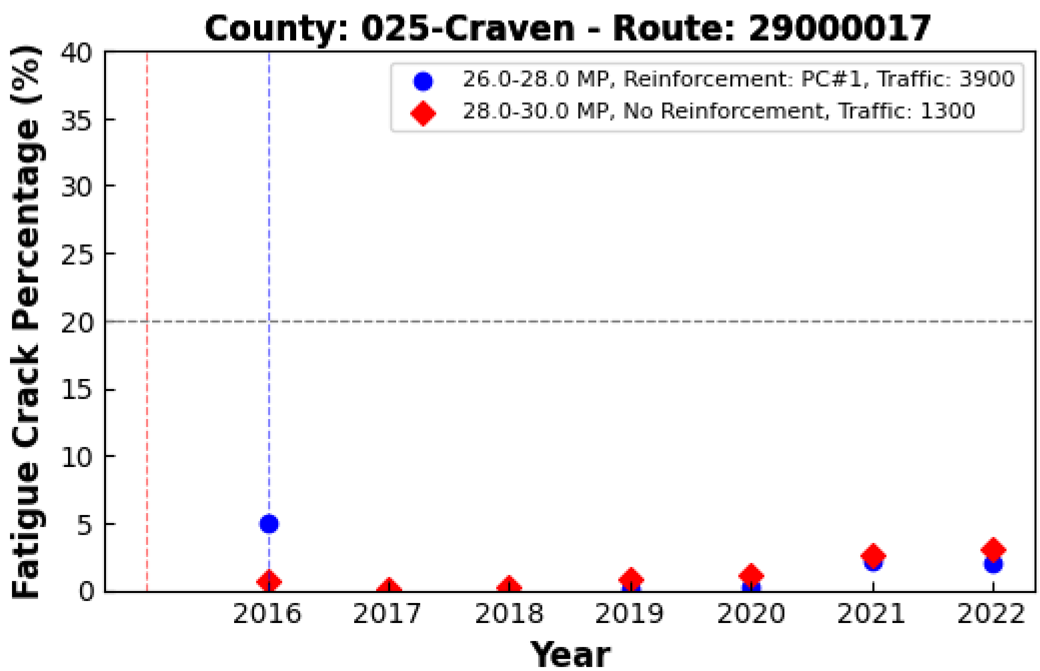

Figure 5-16. Total fatigue crack percentages by year for Craven County at Route 29000017.

Chapter 6. Notched Beam Fatigue Test Results and Discussion

Major fracture modes that drive reflective cracking in the field are opening mode (Mode I) and shearing mode (Mode II). A detailed explanation of the reflective cracking mechanism is provided in Appendix A. Thermal effects and vehicular loading cause Mode I fracture whereas Mode II is caused primarily by the vehicular load alone. Mode I fracture caused by thermal effects can be mimicked using an Overlay Tester, and Mode I fracture due to vehicular loading can be represented by a bending test. Mode II tests of AC fracture due to vehicular traffic are four-point shear tests. However, although Mode II fracture is a significant factor in the field, the test protocol available is not common and thus is relatively unexplored. Also, note that the major driving force for reflective cracking is fatigue loading (a combination of traffic and thermal loads) that is experienced by pavements in the field. Numerous fatigue test configurations are readily available in the literature, and the outcomes can be correlated to field behavior depending on the fatigue test type and failure criteria applied to the results. The fatigue test selected to measure the crack resistance of geosynthetic-reinforced AC in this study is the four-point bending notched beam fatigue test or in short NBFT. The NBFT captures the Mode I fracture under fatigue loading. In the NBFT, the crack resistance capacity is determined by the number of load cycles the geosynthetic-reinforced beam specimen resists before reaching the failure threshold.

The selection of an appropriate failure criterion is a common consideration for laboratory asphalt fatigue testing. Many factors should be taken into consideration when developing an ideal failure criterion, but the criterion should involve only simple measurements, such as the load and displacement of the specimen, and avoid dependency on visual crack monitoring and advanced techniques such as DIC. However, correlating DIC results with traditional failure criteria was essential for this investigation in order to eliminate DIC for future test conditions. Also, a DIC study can help designers anticipate a particular failure mode in the field when using a geosynthetic product for paving applications.

6.1 Fatigue Models and Failure Criteria

The primary reason for conducting fatigue tests of AC mixtures is to find the parameters that allow models to predict the fatigue life of the tested mixture for a given pavement structure. In this case, the parameters were used to predict the crack resistance of geosynthetic-reinforced AC in a layered pavement structure. The crack resistance capacity of a geosynthetic-reinforced beam is measured similarly to the fatigue life of a homogenous AC beam specimen. In general, fatigue models that are used to predict the responses of AC pavements can be categorized into phenomenological and mechanistic approaches. In the phenomenological approach, the fatigue characteristics of the asphalt mixture usually are expressed as the relationship between the initial stress or strain and the number of load repetitions to failure. The mechanistic approach employs two major damage theories to predict pavement performance. One theory works on the principle of fracture mechanics, while the other is continuum damage theory to define the fatigue behavior of AC. Phenomenological models are used more commonly than mechanistic models to evaluate pavement performance. A phenomenological approach was adopted in this study to evaluate fatigue life in terms of crack resistance.

In the phenomenological approach, the pavement's structural responses are compared against laboratory-developed fatigue failure criteria. The most widely used structural response factor is the tensile strain at the bottom of the AC layer for bottom-up cracking, whereas the tensile strain and shear strain at the pavement's surface layer are used for top-down cracking. The initial number of load repetitions (N_i) and the number of cycles to failure (N_f) that separate the different phases during a fatigue test must be determined arbitrarily by individual experiments. Because the main objective of flexure fatigue testing is to determine how many load repetitions the material will sustain before failure, an accurate, standardized, and consistent definition of failure is needed to maintain the integrity of the test results and provide a consistent basis for any implementation scheme. In general, under controlled strain testing, the fatigue life of stiff mixtures is relatively short and that of softer mixtures is relatively long (Benedetto et al. 2004; Witczak et al. 2007). Many researchers have proposed various failure criteria to determine the number of cycles to failure. The most common criteria are 'conventional' criteria based on the 50% reduction in stiffness as well as the phase angle criterion, *R*-squared criterion, dissipated energy ratio criterion, stiffness degradation ratio criterion, and stress × N failure criterion.

6.1.1 Basic Fatigue Models

Miner's cumulative damage principle typically is applied to predict fatigue cracking in AC pavements (Wilkins 1956). The ratio of predicted repetitions of traffic loading to the allowed repetitions of traffic during a specific period represents the pavement damage during that season. The damage ratios for various seasons are summed to determine the cumulative fatigue damage to the pavement, as shown in Equation (6-1). When the cumulative damage ratio over a period exceeds one, that pavement is considered to be failed due to fatigue cracking. Transfer functions are employed to convert the cumulative damage to the percentage of the area that is cracked.

$$D = \sum_{i=1}^{T} \frac{n_i}{N_i} \tag{6-1}$$

where

D = damage,
T = total number of periods,
n_i = actual traffic for period i, and
N_i = allowable failure repetitions under conditions prevailing in period i.

Equation (6-2) is the general mathematical form found in the literature that is used to measure the number of load repetitions to fatigue failure. This model is a function of the initial tensile strain response at a given location and the modulus of the asphalt layer considered for the initial tensile strain.

$$N_f = \beta_3 k_1 \varepsilon_t^{k_2} E^{k_3} \tag{6-2}$$

where

N_f = number of load repetitions to failure (i.e., fatigue cracking in this case),
ε_t = tensile strain at the bottom of the asphalt layer,
E = modulus of the asphalt concrete,
k_1, k_2, k_3 = material properties (calibration parameters), and

β_3 = field calibration factor (shift factor) that depends on the location and climatic conditions

The material properties k_1, k_2, and k_3 in Equation (6-2) are measured by conducting four-point beam fatigue tests. Figure 6-1 presents a typical fatigue life relationship obtained from the results of beam fatigue tests performed by Chakroborty and Das (2017). They conducted their tests at different tensile strain levels and various temperatures and measured the initial tensile strain at the 50th cycle. Each data point shown in Figure 6-1 is the fatigue life (number of cycles to failure) for the four-point beam fatigue test conducted at a specific temperature, frequency, and strain/stress level.

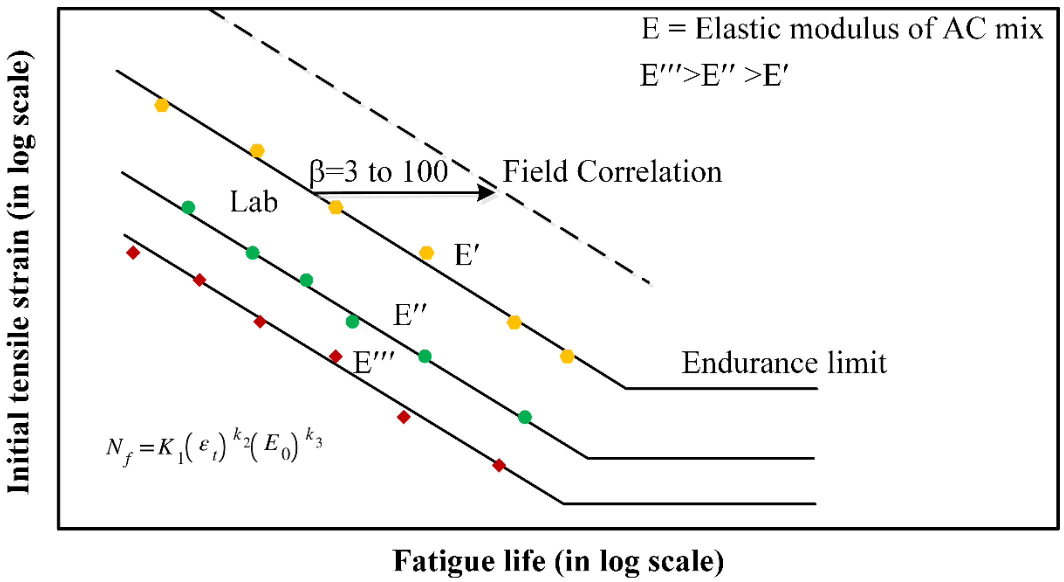

Figure 6-1. Schematic diagram of laboratory fatigue test results for asphalt concrete mixture (Chakroborty and Das 2017).

The fatigue life/specimen failure cycle can be measured using any of the failure criteria proposed in the following Section 6.1.2. Typically, the number of load cycles required for a 50% reduction in flexural stiffness is considered the failure criterion for a homogenous AC mix. Equation (6-3) mathematically expresses the phenomenological relationship for fatigue life for laboratory test results (Asphalt Institute 1991; Monismith et al. 1985; Shell International Petroleum Company 1978; Si et al. 2002; Tayebali et al. 1994). The Equation (6-3) coefficients are obtained by fitting the expression to the data points shown in Figure 6-1. The trend indicates that an increase in the mixture modulus reduces the fatigue life. This response is attributable to the brittle nature of the binder at high modulus values and vice versa in terms of fatigue failure. However, the fatigue life that is predicted using Equation (6-3) cannot be applied directly to predict field performance due to complexities in the field. Hence, users of this equation must develop local calibration factors (β) based on field studies to help relate lab study results to the field.

$$N_f = K_1\left(\varepsilon_t\right)^{k_2}\left(E_0\right)^{k_3} \tag{6-3}$$

where

ε_t = initial tensile strain,
E_0 = initial stiffness (modulus) of the material, and
k_1, k_2, k_3 = regression coefficients.

6.1.2 Different Types of Failure Criteria

The failure criterion that is selected to define failure determines the fatigue life. Descriptions of commonly used criteria and ways that each criterion can help determine the crack resistance of geosynthetic-reinforced AC mixes are provided below.

Conventional Criteria

During a beam fatigue test, the information obtained from the test device is the load and displacement data. This information is substituted in the relationships shown in Equations (6-4), (6-5), and (6-6) and used to measure the maximum stress, strain, and flexural stiffness, respectively, of beam specimens during four-point bending beam fatigue tests. Details regarding the derivations of the equations are provided in Appendix B.

$$\sigma_t = \frac{3 \times a \times P}{b \times h^2} \tag{6-4}$$

where
a = center-to-center spacing between clamps (Cox: 119 mm),
P = load applied by the actuator (N),
b = average specimen width (mm), and
h = average specimen height (mm).

$$\varepsilon_t = \frac{12 \times \delta \times h}{\left(3 \times L^2\right) - \left(4 \times a^2\right)} \tag{6-5}$$

where
δ = maximum deflection at the center of the beam (mm) and
L = length of the beam between outside clamps (Cox: 357 mm).

Equation (6-6) is used for calculating the flexural beam stiffness (MPa) that is referred to as stiffness (S) in this research.

$$S = \frac{\sigma_t}{\varepsilon_t} \tag{6-6}$$

Once the stiffness value is calculated for each data point during the test, it can be plotted against the number of cycles.

The flexural stiffness degradation of the beam that occurs with an increase in the number of load cycles in constant strain and constant stress mode tests follows a typical trend, as shown in Figure 6-2 (axes are in linear-linear scale). The three stiffness reduction phases are the primary, secondary, and tertiary stages, described in the following text.

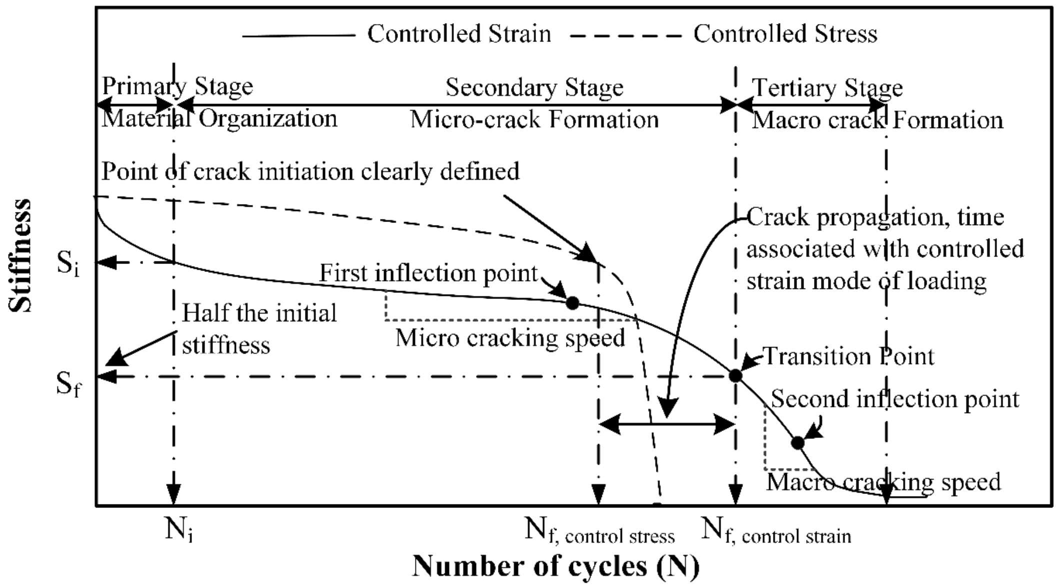

Figure 6-2. Typical relationships between stiffness and number of load repetitions for controlled strain mode vs. controlled stress mode tests.

Phase I or adaptation phase: The primary phase is associated with a rapid decrease in mixture stiffness. The material reorganization, equipment seating effects, and heat development can contribute to the sudden loss in stiffness. However, this stiffness is readily recoverable once the test is paused during this phase.

Phase II or quasi-stationary phase: The secondary phase is characterized by a steady linear decrease in stiffness at a slower rate than in the primary phase. The reduction in stiffness is due mainly to the formation of microcracks.

Phase III or failure phase: The tertiary stage starts with the formation of macrocracks. That is, the microcracks formed during Phase II coalesce to form macrocracks in Phase III. In both modes of loading (controlled strain and controlled stress), clear and definite transition points between the different phases are tedious to mark, as the formation of microcracks and macrocracks cannot be tracked easily during the test.

Stress $\times$ N Failure Criterion

The stiffness degradation ratio provides a quick and reasonable alternative for finding the failure point. Following this approach, a refined failure definition is proposed for cyclic fatigue testing, where cyclic fatigue failure is the cycle at which the product of the stress amplitude and cycle number reaches a peak value. Figure 6-3 shows the product of the stress and cycle number versus cycle number for a typical uniaxial cyclic fatigue test. The use of stress amplitude instead of stiffness eliminates the need for any on-specimen LVDT measurements and allows the failure cycle to be defined accurately, even in cases where the specimen fails outside the LVDT gauge points. Lee (2020) analyzed the effect of changing the failure definition by applying both the phase angle criterion and the product of the stress and cycle number approach during a uniaxial cyclic fatigue test. Lee (2020) found that the peak of the stress times the number of cycles yields approximately 6% shorter fatigue life than the phase angle criterion.

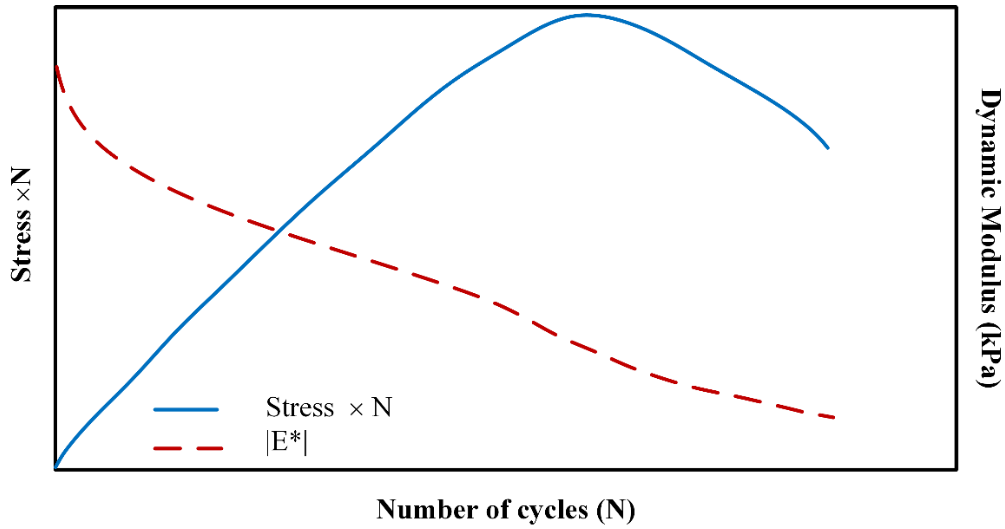

Figure 6-3. Stress × N versus number of loading cycles.

Figure 6-4 shows the change in the stress × N versus load cycles at different strain levels for the control specimen (‘CS’) and five geosynthetic-reinforced specimens. The control specimens show clear failure points at different strain levels, whereas the failure points are difficult to identify for the geosynthetic-reinforced specimens at certain strain levels due to the distorted stress × N versus N pattern or due to non-existent peak points.

Note that two different mechanisms develop as the notched beam is subjected to cyclic loading, i.e., vertical cracking and horizontal debonding at the interface of the geosynthetic interlayer and asphalt layer. The cyclic loading in NBFTs causes a crack to start at the tip of the notch and propagate to the interface. Then, the energy input that is due to the cyclic loading causes the vertical crack to turn in the horizontal direction if the bond strength between the geosynthetic and the bottom asphalt layer is low. If the bond strength is high, then the crack stalls at the interface of the geosynthetic layer and overlay. When the energy input that is due to cyclic loading exceeds the resistance from the interlayer, the crack starts to propagate upwards, causing reflective cracking. Therefore, the bond strength between the geosynthetic interlayer and the asphalt overlay is an extremely important factor and must be sufficient in order to fully capture the benefits of geosynthetic interlayers.

Also, note that the ‘failure’ detected by the stress × N failure criterion is caused by a combination of both the vertical cracking and horizontal debonding mechanisms. Therefore, the number of loading cycles at failure (N_f) should not be interpreted as the conventional fatigue life that is due to fatigue cracking, but rather as the life of the asphalt overlay that is due to the combined effects of vertical cracking and horizontal debonding on the geosynthetic-reinforced asphalt beam’s resistance to loading.

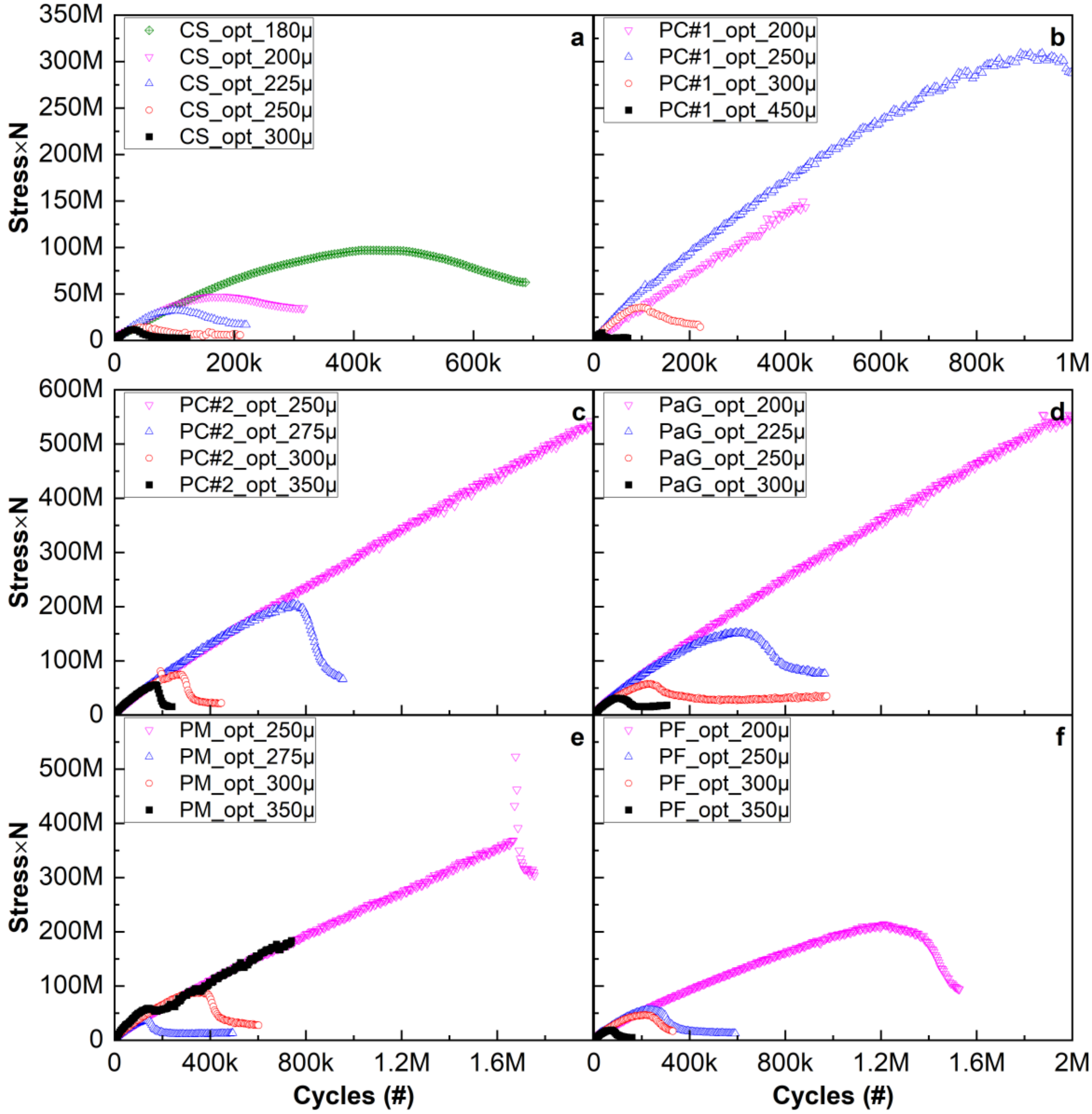

Figure 6-4. Stress × N (cycles) versus load cycles during fatigue tests: (a) CS, (b) PC#1, (c) PC#2, (d) PaG, (e) PM, and (f) PF.

6.2 Crack Resistance Capacity of Geosynthetic-Reinforced Beam Specimens

Figure 6-5 and Figure 6-6 respectively present the actuator and on-specimen tensile strain levels versus number of cycles to failure (N_f) plots for CS and the five geosynthetic-reinforced beam specimens used in this study. The stress × N failure criterion was applied to the NBFT results to determine the number of cycles to failure (N_f). The results of the lengthy tests for PC#1, PC#2, and PaG, which required the prediction of N_f values are not included in these figures to be consistent with other interlayer cases. The data in Figure 6-5 and Figure 6-6 were used to determine the fatigue coefficients k_1 and k_2 in Equation (6-7) for the five geosynthetic products and the 'no interlayer' unreinforced control scenario (CS). Table 6-1 and Table 6-2 present the fatigue coefficients obtained after fitting the data shown in Figure 6-5 and Figure 6-6, respectively, as well as the R^2 values obtained from regression analysis.

$$N_f = k_1 \left(\frac{1}{\varepsilon_t} \right)^{k_2} \tag{6-7}$$

where

N_f = number of cycles to failure, representing crack resistance,
k_1, k_2 = regression coefficients, and
ε_t = tensile strain in microns.

Both visual observations of the figures and the R^2 values suggest that the actuator tensile strain yields a better correlation (i.e., less scatter) with N_f than the on-specimen tensile strain. The reason for this finding is that on-specimen strain is determined from the on-specimen displacement at the 50th cycle. As mentioned in Section 3.1.3, the on-specimen displacement changes during the NBFT, which is in actuator displacement control mode. Changes in the on-specimen displacement during the NBFT may be different for different beam specimens for the same interlayer type and therefore may cause variation in the on-specimen strain at the 50th cycle. Also, the use of the strain at the 50th cycle as the 'initial' strain is arbitrary.

Several observations can be made from Figure 6-5 and Figure 6-6. Although data points are scattered in some cases, these figures clearly show the benefits of using a geosynthetic interlayer. As demonstrated in Figure 6-5, the fatigue life of geosynthetic-reinforced specimens is longer than that of the unreinforced (CS) specimens for the same tensile strain level regardless of the geosynthetic product type. Recognizing that the x-axis is in log scale, this increase in fatigue life is substantial. This enhancement in fatigue life can be even greater when we consider the effect of increased stiffness due to reinforcement in pavement structures. Increased stiffness due to reinforcement decreases the tensile strain at the bottom of asphalt overlays, thus increasing the fatigue life.

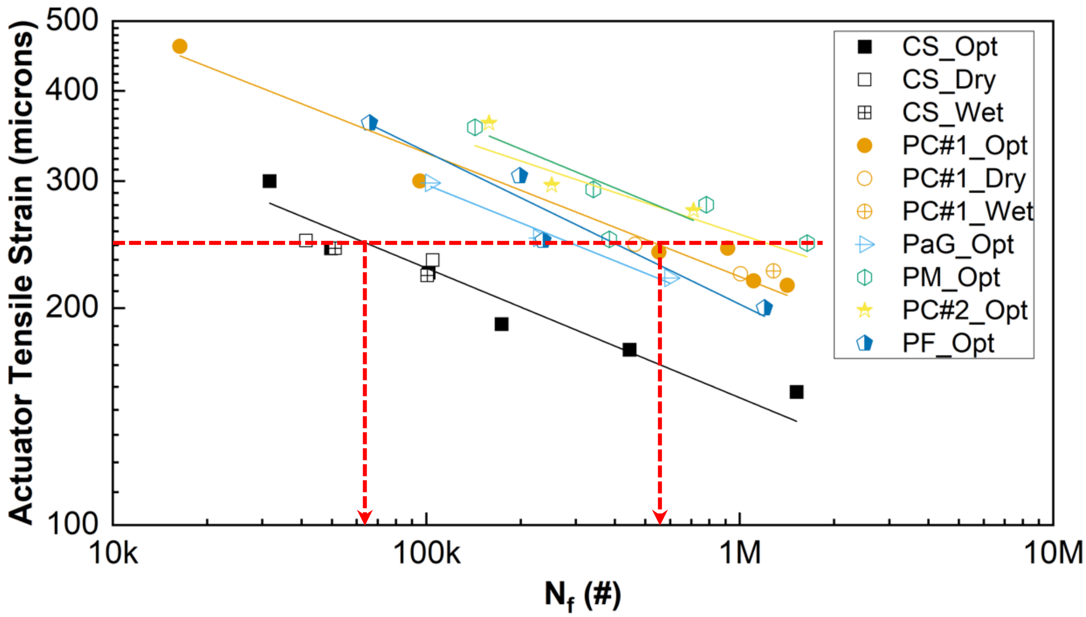

Figure 6-5. Actuator tensile strain versus fatigue life for unreinforced (CS) and reinforced beam specimens.

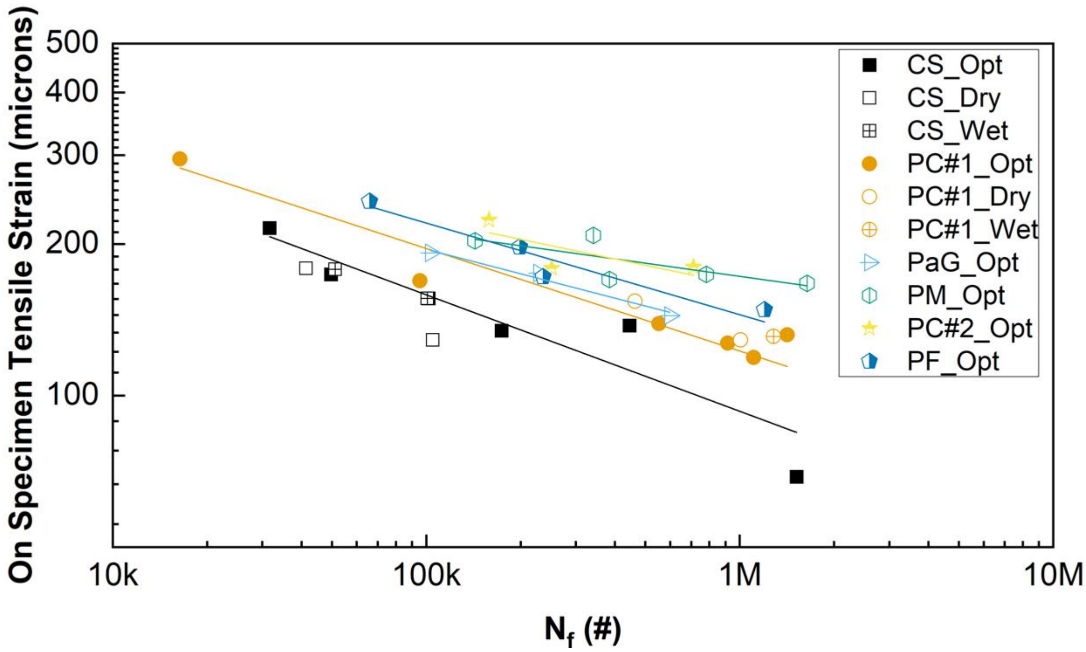

Figure 6-6. On-specimen tensile strain versus fatigue life for unreinforced (CS) and reinforced beam specimens.

Table 6-1. Fatigue Coefficients of Actuator Tensile Strain versus N_f for Unreinforced (CS) and Reinforced Specimens

Interlayer Type	CS	PC#1	PaG	PM	PC#2	PF
k_1	3.52×10^{-14}	1.08×10^{-17}	9.15×10^{-17}	3.30×10^{-21}	5.81×10^{-18}	2.35×10^{-13}
k_2	5.07	6.31	5.97	7.37	6.47	5.05
R^2	0.93	0.87	0.92	0.57	0.72	0.9

Table 6-2. Fatigue Coefficients of On-Specimen Tensile Strain versus N_f for Unreinforced (CS) and Reinforced Specimens

Interlayer Type	CS	PC#1	PaG	PM	PC#2	PF
k_1	5.15×10^{-16}	1.42×10^{-11}	8.82×10^{-19}	5.09×10^{-38}	6.38×10^{-24}	8.03×10^{-16}
k_2	5.35	4.25	6.21	11.50	7.72	5.49
R^2	0.78	0.90	0.95	0.42	0.1	0.89

The data shown in Figure 6-5 and Figure 6-6 were generated using the beam specimens with optimal tack coat application rates recommended by the individual geosynthetic manufacturers. In order to investigate the effect of tack coat application rate on the performance of geosynthetic-reinforced asphalt specimens, the application rate for CS and PC#1 specimens was adjusted by decreasing and increasing 0.091 L/m^2 (0.02 gal/yd^2) from the manufacturer's optimal application rate, respectively. The decision to adjust the optimal rate by 0.091 L/m^2 (0.02 gal/yd^2) was influenced by findings from previous research and involved a comparison between the target application rate set on the tack coat sprayer truck and the application rates observed in the field in earlier studies. The NBFT results for dry and wet specimens for CS and PC#1 are plotted in Figure 6-7, separately from all the other geosynthetic data.

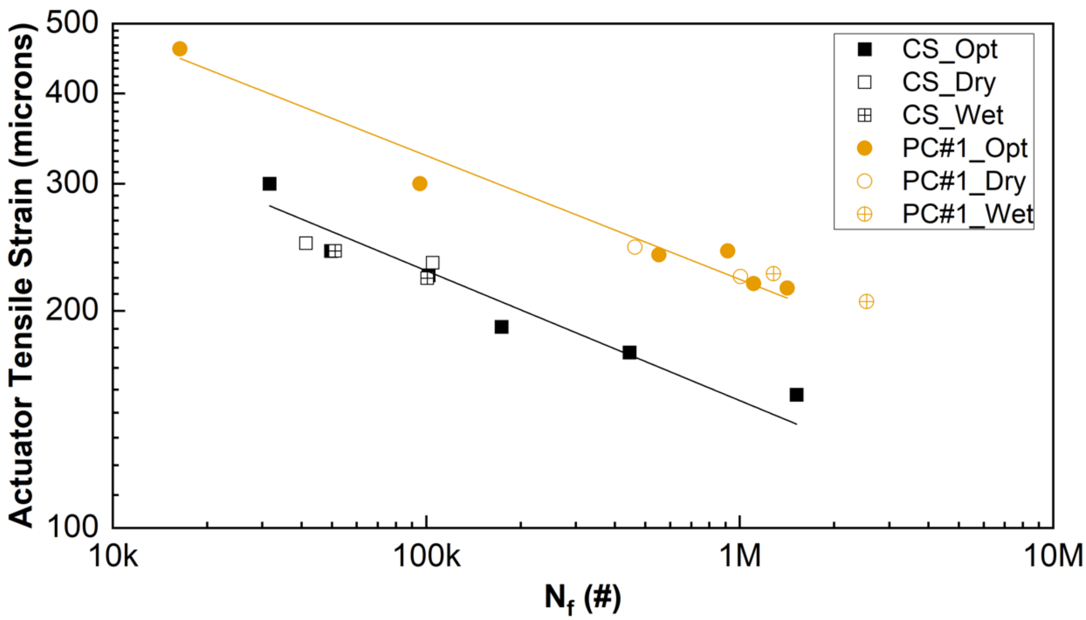

Figure 6-7. Actuator tensile strain versus fatigue life for reinforced (PC#1) and unreinforced (CS) beam specimens.

The initial hypothesis was that increasing the tack coat rate would enhance specimen performance up to a certain peak, beyond which performance would decline after surpassing the 'optimal' tack coat rate. However, the dry and wet results in Figure 6-7 fall near the line for the optimal rate, leaving the precise rate at which performance decreases unidentified.

In order to evaluate the effect of tack coat application rate on fatigue life, the number of cycles to failure of CS and PC#1 specimens at various application rates are summarized in Table 3. In this table, a specific Specimen ID is used to reflect the reinforcement type, tack coat application rate, and strain level. Within each category, specimens are further distinguished based on the tack coat rates, labeled as 'dry', 'wet', or 'optimal' (opt). The final three-digit number in each Specimen ID represents the actuator-based tensile strain measured for that particular specimen. The Specimen IDs and their corresponding N_f (number of cycles to failure) values provide the following insights into the performance of these specimens under different conditions.

- For CS specimens, CS_dry slightly outperforms CS_wet at the lower strain level. However, at the higher strain level, increasing the tack coat rate increases the fatigue life.
- For PC#1 specimens, increase in tack coat rate consistently shows increase in the fatigue life.

- Based on the above two observations, it is reasonable to conclude that the increase in tack coat application rate increases the fatigue life of geosynthetic-reinforced asphalt specimens.
- When comparing optimal conditions, PC#1_opt_242 significantly outperforms CS_opt_242, indicating a substantial improvement in performance with the use of PC#1.

Table 3. Summary of fatigue life of specimens with various application rate

Specimen ID	**N_f**	**Specimen ID**	**N_f**
CS_dry_222	104,825	PC#1_dry_224	1,006,351
CS_wet_225	100,777	PC#1_wet_225	1,282,115
CS_dry_247	41,380	PC#1_dry_246	462,831
CS_opt_242	49,645	PC#1_opt_242	916,086
CS_wet_243	51,202	PC#1_wet_208*	2,539,499

Note: *N_f preidicted based on Weibull model.

Chapter 7. Development of Field Calibration Guidelines for Geosynthetic Products

This chapter details the research team's efforts to develop a step-by-step procedure for predicting field performance of geosynthetic-reinforced asphalt overlays. The elements required for developing these guidelines are as follows:

- **Predictive Model for Crack Resistance:** This model assesses the fatigue life of an asphalt overlay reinforced with a geosynthetic interlayer. It uses the tensile strain at the bottom of the overlay to predict crack resistance and overall performance.

- **Predictive Model for Tensile Strain:** This model determines the tensile strain at the bottom of the asphalt overlay, based on the load-bearing capacity of the pavement layer beneath the overlay. It is essential for evaluating the overlay's structural integrity.

- **Temperature Correction Model:** This model predicts FWD deflections at a reference temperature using deflections measured at varying temperatures. This correction is crucial for standardizing deflection data across different temperature conditions.

- **Calibration Factor (Beta):** This factor is a function of pavement thickness and is crucial for translating the damage index derived from laboratory tests to field-measured fatigue crack percentages (FC%). The calibration factor ensures that laboratory findings are applicable to real-world conditions, enhancing the reliability of the predictive models for field performance.

The research team integrated these elements to develop a procedure for geosynthetic interlayer product selection. The following sections discuss the research efforts undertaken to obtain each of these elements, providing detailed insights into the methodologies and results that contribute to the comprehensive guidelines for pavement design and maintenance.

7.1.1 Development of Predictive Model for Crack Resistance Capacity

The crack resistance capacity of various geosynthetic-reinforced beam specimens was measured using NBFTs conducted at different constant actuator tensile strain levels at 23°C (73°F). Typically, the crack resistance model is established by correlating tensile strain with crack resistance. In NBFTs, tensile strain is measured at the underside of the beam specimen. However, in field applications, the tensile strain of interest is at the interface or bottom of the overlay. Therefore, it is essential to establish a relationship between interlayer tensile strain and crack resistance to develop an accurate beam crack resistance model. Further analysis shows that the usage of on-specimen tensile strain measured at the bottom of the beam provides reasonable damage index values that can be compared to FC%. Hence, it was decided to use the on-specimen tensile strain at the beam bottom to establish the predictive model.

The analysis of NBFT outcomes led to the development of a relationship between tensile strain and crack resistance, which is presented in Equation (7-1). Figure 7-1 shows the data points of all the NBFT results and the fitted crack resistance model.

$$N_f = k_1 \left(\frac{1}{\varepsilon_t} \right)^{k_2} \tag{7-1}$$

where

N_f = number of cycles to failure, representing crack resistance,
k_1, k_2 = regression coefficients, and
ε_t = tensile strain in microns.

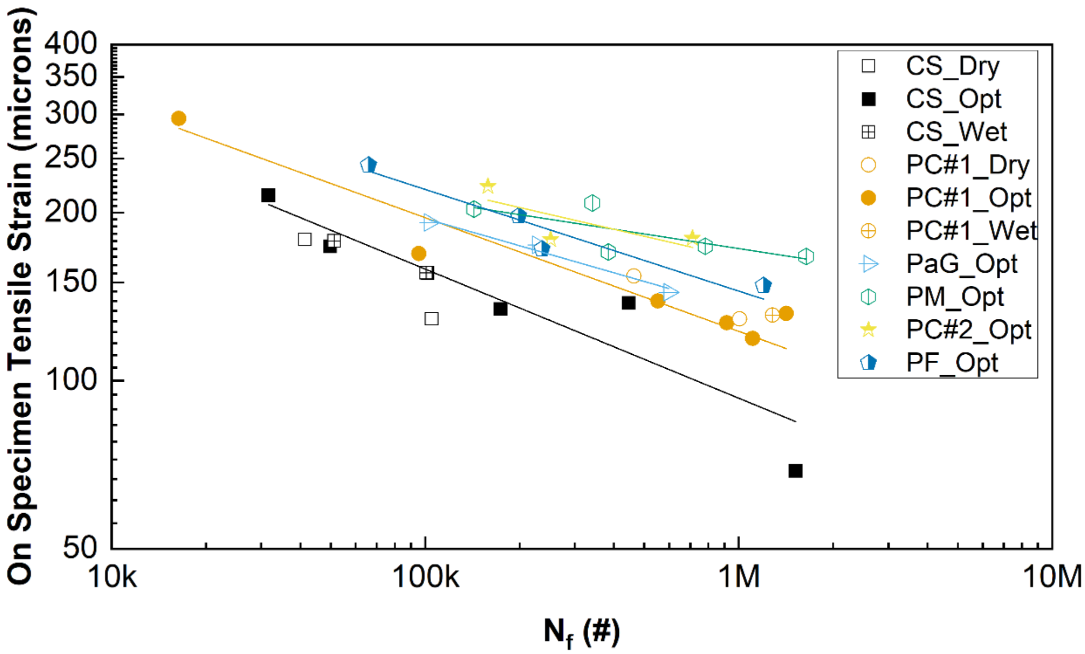

Figure 7-1. Crack resistance model showing relationship between tensile strain and N_f.

Table 7-1 presents the parameters k_1 and k_2 for the five geosynthetic products and the 'no interlayer' scenario (CS). Equation (7-1) and the k_1 and k_2 values in Table 7-1 are used to determine the crack resistance of asphalt overlays reinforced with different geosynthetic interlayer products. The results are used in developing the predictive procedure for geosynthetic-reinforced asphalt overlays, which is presented later in this chapter.

Table 7-1. Fatigue Coefficients of Interlayer Tensile Strain versus Number of Loading Cycles for Unreinforced and Reinforced Specimens

Interlayer Type	**CS**	**PC#1**	**PaG**	**PM**	**PC#2**	**PF**
k_1	5.15×10^{-16}	1.42×10^{-11}	8.82×10^{-19}	5.09×10^{-38}	6.38×10^{-24}	8.03×10^{-16}
k_2	5.35	4.25	6.21	11.50	7.72	5.49
R^2	0.78	0.90	0.95	0.42	0.1	0.89

7.1.2 Prediction of Tensile Strain at the Bottom of Asphalt Overlay

In the previous RP2019-19 report, the failure modes of geosynthetic-reinforced beams—vertical cracking or debonding—were found to depend on the type of geosynthetic interlayer and the strain level, as indicated by DIC contours. The change in failure modes with varying strain levels introduced the transient tensile strain concept, which suggests that any overlay strain level above the transition tensile strain indicates vertical cracking, while strain levels below this threshold indicate debonding.

To implement this concept in geosynthetic product selection guidelines, a predictive model for the tensile strain under the asphalt overlay was developed. This model was based on the load-bearing capacity of both the asphalt overlay and the existing pavement, using inputs such as FWD deflections, overlay thickness and properties, and the material properties of the underlying pavement layers.

Kim et al. (2000) demonstrated a close relationship between the tensile strain at the bottom of an asphalt layer and deflection basin parameters. In the RP2019-19 study, pavement response analysis using EverstressFE software was conducted for various thickness and modulus combinations to develop this relationship. Deflection basin parameters were calculated for sections without an overlay, and simulations with three overlay thicknesses were used to determine the tensile strain underneath the overlay. Linear regression was then performed to develop a predictive model using overlay tensile strain as the dependent variable and parameters such as overlay thickness, deflection basin parameters such as SCI, BDI, and BCI, and $Esg \times Teq$ as independent variables.

However, this approach has limitations. When a new thin overlay is placed, if the existing pavement is not sufficiently damaged, the strain at the bottom of the overlay determined by FEM can be compressive because the neutral axis of the overlay and existing pavement together is below the interface between the overlay and the existing pavement. As the pavement deteriorates over time, the neutral axis moves upward, and tensile strains start to develop under the overlay. Therefore, solely relying on pavement response analysis based on continuum mechanics could yield spurious results.

7.1.3 Development of Predictive Equation for Overlay Strain Using Jung's Method

To address these limitations, we adopted an alternative approach proposed by Jung (1988) for determining the tensile strain at the bottom of the asphalt concrete layer. This method bypasses the need to back-calculate the modulus of each layer, directly estimating the tensile strain from the deflection basin. Jung's equation that is applied to the estimation of tensile strain (ε_t) at the bottom of asphalt overlay is given by:

$$\varepsilon_t = \frac{h_{OL}\,(d_0 - d_{tire\ edge})}{r_{tire}^2} \qquad (7\text{-}2)$$

where

h_{OL} = thickness of the asphalt concrete layer,
d_0 and $d_{tire\ edge}$ = deflections at the center and at the edge of the tire placed on the overlay, respectively, and
r_{tyre} = radial distance at the tire edge.

Preliminary parametric studies using multilayered elastic software for a theoretical pavement system under a standard 40 kN load revealed that the tensile strain calculated using Burmister's theory is approximately 30% to 50% of that calculated with Jung's equation. Therefore, Jung's method tends to overestimate the tensile strains at the bottom of asphalt concrete layers, leading to an underestimation of pavement fatigue life. This overestimation highlights the strong dependency of tensile strain on asphalt concrete modulus and thickness, as well as on the base material modulus.

To improve the accuracy of the predictive model, we adjusted the tensile strain estimation from Jung's method by taking only 60% of its value, accounting for the overestimation. The adjusted tensile strains underneath the overlay (i.e., 0.6 x tensile strain from Equation (7-2)) were correlated to the deflection basin parameters of pavements without overlay, which were obtained by numerical simulations in Chapter 4. The resulting predictive equation for tensile strain under the overlay is as follows:

$$\varepsilon_t = 0.6\times\left(-66.2+35.676\times h_{ac}+337\times\log(SCI)-362\times\log(BDI)+159\times\log(BCI)\right) \qquad (7\text{-}3)$$

where

SCI = $d_0 - d_{12}$,

BDI = $d_{12} - d_{24}$,

BCI = $d_{24} - d_{36}$, and

d_{12}, d_{24}, d_{36} = deflections at 12, 24, and 36 inches, respectively, on existing pavement without overlay.

The predicted tensile strain from Equation (7-3) without the reduction factor of 0.6 was compared against the tensile strain predicted using Jung's method in Equation (7-2) in Figure 7-2. Reasonable comparison is found in the figure.

Note that Equation (7-3) allows the prediction of tensile strain at the bottom of the overlay using the FWD deflections from the existing pavement and the overlay thickness. That is, users of this equation can perform FWD tests on a pavement prior to asphalt overlay and use the resulting deflections and design overlay thickness to determine the tensile strain under the asphalt overlay, thus the fatigue life of the overlay.

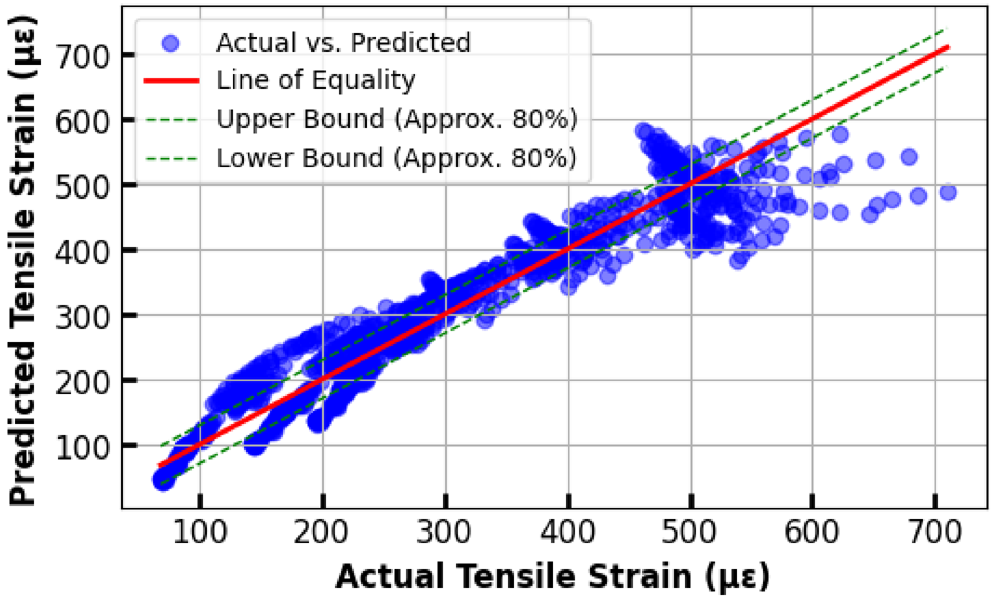

Figure 7-2. Predicted and measured overlay tensile strain using Equation (7-3).

7.1.4 Temperature Correction for Deflections at Radial Offset Distance

The FWD deflections measured at a specific temperature must be corrected to the reference temperature of 23°C (73.4°F) because all the NBFTs were conducted at 23°C (73.4°F). The temperature correction factor, show in in Equation (7-4), is the ratio of the measured deflection at a specific temperature (*T*) to the deflection at a reference temperature, which in this case is 23°C (73.4°F).

Kim et al. (1997) proposed a deflection correction model shown in Equation (7-4) based on their statistical analyses of measured deflections and temperatures in North Carolina. The deflection correction factor (λ_w) for center deflections measured under a 9-kip FWD load can be expressed as Equation (7-5).

$$\lambda_w = \frac{w_{T_0}}{w_T} \tag{7-4}$$

where

w_{T_0} = deflection corrected to temperature T_0,
w_T = deflection at temperature *T*, and
λ_w = temperature correction factor.

$$\lambda_w = 10^{-C(H_{ac})(T-T_0)} \tag{7-5}$$

where

H_{ac} = asphalt concrete layer thickness (in.), and
C = regression constant.

To provide temperature correction factors at various offset distances, an empirical model was developed based on statistical analysis of the temperature deflection data. Because the degree of the temperature dependency of a deflection linearly decreases as the radial distance increases, the *C* value at a given offset distance may be determined using Equation (7-6).

$$C = -Ar + C_0 \tag{7-6}$$

where

r = radial distance from center of load plate (in.), and
C_0 and A = regression constants, which are different for three regions.

Table 7-2. C_0 and A Values for Each North Carolina Region and Statewide Values

Regions	**C_0 values**	**Statewide C_0 value**	***A* value**	**Statewide *A* value**
East	3.61×10^{-5}	4.65×10^{-5}	-5.72×10^{-8}	-5.47×10^{-8}
Central	5.80×10^{-5}		-5.62×10^{-8}	
West	4.32×10^{-5}		-5.07×10^{-8}	

Kim et al. (1997) reported that the corrections appear to work well except for the last FWD sensor. At a radial distance of 60 in., the deflection at a low temperature is greater than at a high temperature. This phenomenon is thought to be due to the reduction in stiffness of the AC layer at high temperatures, which in turn reduces the lateral spread of the stress distribution.

7.1.5 Measuring Pavement Temperature for Pavement Performance Calculation

It is crucial to know the average monthly temperature of the surface AC layer to accurately measure pavement performance. The temperature found at mid-depth of the surface AC layer is used to determine the modulus of that layer. Therefore, the temperature of a layer depends not only on its location (latitude and longitude) and pavement structure (AC surface layer thickness) but also on the climate model used for prediction.

Several pavement temperature prediction models are available, including the Enhanced Integrated Climatic Model (EICM), SHRP A-648A, BELL2, and BELL3. Figure 7-3 shows the hourly temperature fluctuation at different pavement depths using EICM. Average monthly temperature for 20 years was calculated using different models and plotted in Figure 7-4. Note that, in January, the surface temperature predicted by SHRP A-648A model is about 30°C, whereas the average air temperature is lower than 5°C. This difference is deemed to be too much, and thus EICM is selected in this study to predict temperature profiles. It integrates climatic impacts consistently and comprehensively into pavement design, ensuring more reliable, durable, and optimized pavement structures. When averaged over a day, month, and multiple years, the average monthly temperature at the surface and various depths calculated using EICM remains fairly constant in Figure 7-4. This consistency simplifies the analysis of pavement performance and helps in predicting long-term behavior under climatic influences.

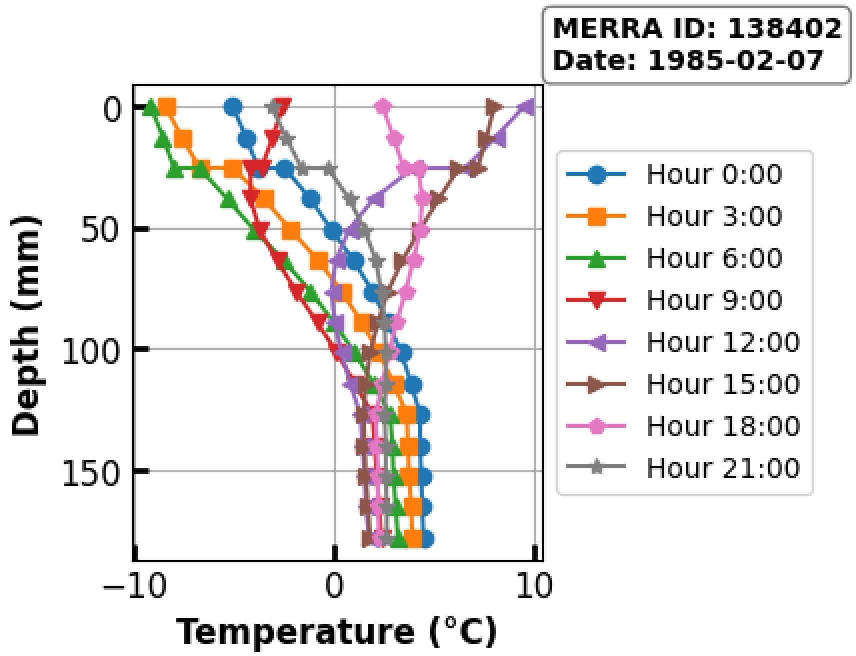

Figure 7-3. Hourly temperature profile using EICM.

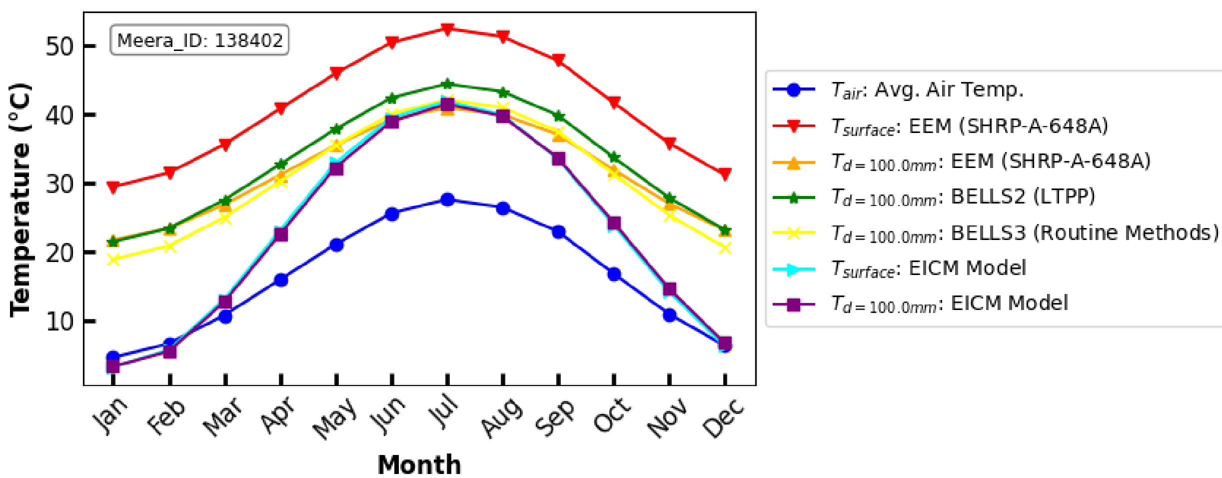

Figure 7-4. Averaged monthly temperature for more than 20 years using different models and depth.

7.1.6 Calculation of Pulse Duration for Dynamic Modulus Analysis

The primary objective of this analysis is to accurately calculate the pulse duration, as the loading time is a critical factor in determining the dynamic modulus of asphalt concrete. The tensile stress data (*Sxx*) along the transverse direction is analyzed using a bell shape model to fit the experimental data obtained from pavement response analysis performed with FlexPAVE 1.1. The analysis is conducted on a thick pavement with an AC layer of 7 inches under a standard wheel load of 80 kN, considering various speeds (10, 25, 40, 55, 70 mph) and depths (ranging from 0.5 to 5.0 inches in increments of 0.5 inches).

The bell shape model, characterized by its symmetric peak, effectively represents phenomena with a central peak and gradual decay on either side. Mathematically, the model is defined by the Gaussian function:

$$y(x) = a \times e^{\left(-\frac{(x-b)^2}{2c^2}\right)} \tag{7-7}$$

where *y(x)* represents the fitted *Sxx* values, *x* represents time, *a* is the amplitude of the peak, *b* is the location of the peak, and *c* controls the width of the bell shape. The width parameter *c* is particularly important as it is considered equivalent to the pulse duration.

In this implementation, the parameters *a, b,* and *c* are adjusted to best fit the experimental data. The function is evaluated over a dense range of *x* values between the specified start and end indices to ensure a smooth representation of the fitted curve.

The original tensile stress (*Sxx*) data points are plotted alongside the fitted bell shape model to visually assess the accuracy of the fit. Additionally, a vertical dashed line is added at *x=0* to indicate the peak time, aligning with the peak of the fitted curve. This model effectively captures the central tendency and spread of the tensile stress data along the transverse direction.

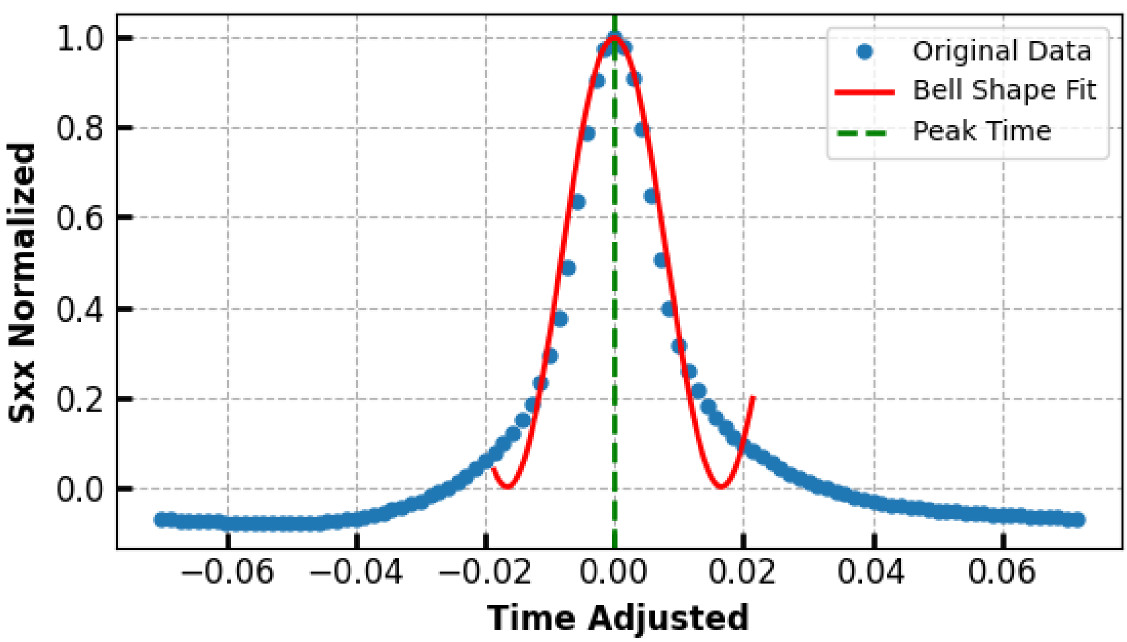

Figure 7-5. Representative fitted Bell Shape model on a pavement response data.

The pulse duration, determined by the width parameter *c*, is calculated for different depths and speeds. These pulse durations are then compiled into a table, providing essential data for the calculation of the dynamic modulus of the pavement. This comprehensive approach allows for the detailed analysis of pulse durations across different conditions, offering valuable insights into the behavior of tensile stress under varying depths and speeds, ultimately aiding in the accurate determination of the pavement's dynamic modulus.

Table 7-3. Vehicle Pulse Duration in Seconds at Different Depths and Vehicle Speeds

Depth (in.) \ Speed (mph)	10	25	40	55	70
0.5	0.1258	0.0505	0.0331	0.0241	0.0189
1.0	0.1316	0.0542	0.0373	0.0272	0.0214
1.5	0.1379	0.0560	0.0369	0.0269	0.0211
2.0	0.1421	0.0575	0.0371	0.0274	0.0215
2.5	0.1449	0.0596	0.0380	0.0285	0.0224
3.0	0.1506	0.0605	0.0395	0.0288	0.0226
3.5	0.1595	0.0642	0.0419	0.0307	0.0241
4.0	0.1704	0.0686	0.0448	0.0327	0.0257
4.5	0.1778	0.0714	0.0467	0.0341	0.0268
5.0	0.1781	0.0716	0.0468	0.0342	0.0269

7.1.7 Calculation of Damaged Dynamic Modulus

The dynamic modulus of the existing, damaged asphalt layer ($|E^*|_{dam}$) is a critical parameter for evaluating the performance of asphalt overlays in field conditions. The calculation involves determining the amount of damage in existing asphalt layers, represented by the damage parameter (d_{AC}), and using it to adjust the undamaged dynamic modulus mastercurve. Below is a step-by-step procedure on how to calculate the damaged dynamic modulus.

Step-by-Step Procedure

1. **Develop Undamaged Dynamic Modulus Mastercurve:**

   Use the sigmoidal function to develop an undamaged dynamic modulus mastercurve from laboratory mixture test. The sigmoidal function is given by:

$$\log(E^*) = \kappa + \frac{\log(\max E) - \kappa}{1 + e^{(\delta + \gamma \log f_r)}} \qquad (7\text{-}8)$$

   where
   $|E^*|$ = dynamic modulus (psi),
   max E = maximum dynamic modulus (psi),
   κ, δ, γ = model parameters, and
   f_r = reduced frequency.

   The following table shows the fitted parameters of the model for the RS9.5C mixture, which is used for this study.

Table 7-4. Sigmoidal Fit Parameters for RS9.5C

Parameter	Value
κ	2.78E+00
Max_E	3.62E+06
δ	-1.49E+00
γ	-4.27E-01
a_1	7.45E-04
a_2	-1.65E-01
a_3	2.89E+00

2. **Obtain Field Cracking Data:**
   - Conduct a distress/condition survey to determine the amount of alligator cracking that was initiated at the bottom of the asphalt layers and was measured at the pavement surface. Express this as FC_{Bottom}, the percentage of total lane area with cracking. Chapter 5 explains the calculation steps.

3. **Calculate the Damage Parameter (d_{AC}):**
   - Use the following equations to calculate d_{AC}:

$$C_2^{'} = -2.40874 - 39.748 \times (1 + h_{ac})^{-2.856} \quad (7\text{-}9)$$

h_{ac} = asphalt concrete layer thickness (in inches)

$$FC_{\text{bottom}} = \left(\frac{6000}{1 + e^{C_1 C_1' + C_2 C_2' \log_{10}(d_{\text{AC}} 100)}} \right) \frac{1}{60} \quad (7\text{-}10)$$

where

FC_{Bottom}	=	area of alligator cracking that initiates at the bottom of hot mix asphalt layers, % of total lane area,
d_{AC}	=	damage parameter in fractional form,
C_1	=	1,
C_2	=	0.876, both C_1 and C_2 are calibrated in the RP 2017-03 project,
C_1’	=	$-2C_2$’, and
C_2’	=	$-2.40874-39.748\ (1+h_{\text{ac}})\ -2.856$.

Solve for d_{AC} using numerical methods.

4. **Calculate the Damaged Dynamic Modulus Mastercurve:**
   - Once d_{AC} is determined, use it to calculate the entire damaged mastercurve from the undamaged mastercurve using the following equation:

$$|E^*|_{\text{dam}} = 10^{\delta} + \frac{|E^*| - 10^{\delta}}{1 + e^{-0.3 + 5\log(d_{\text{AC}})}} \quad (7\text{-}11)$$

where

$|E^*|$ = undamaged dynamic modulus, and

δ = parameter from the undamaged mastercurve.

By following these steps and using the provided equations, the damaged dynamic modulus ($|E^*|_{dam}$) of existing asphalt layers can be calculated. Figure 7-6 presents the undamaged dynamic modulus mastercurve of the RS9.5C mixture used in this study and the damaged dynamic modulus mastercurve based on the structure and condition of NC 96 pavements that were used in the HWY 2017-03 project. Note that the damaged dynamic moduli values at low reduced frequency (lower than around 10^{-5} Hz) are higher than undamaged dynamic moduli values. This unexpected trend is due to the symmetric nature of the sigmoidal function. That is, the shape and magnitude of the damaged dynamic modulus mastercurve at the high reduced frequencies forced the shape and magnitude of the damaged dynamic modulus mastercurve at the low reduced frequencies.

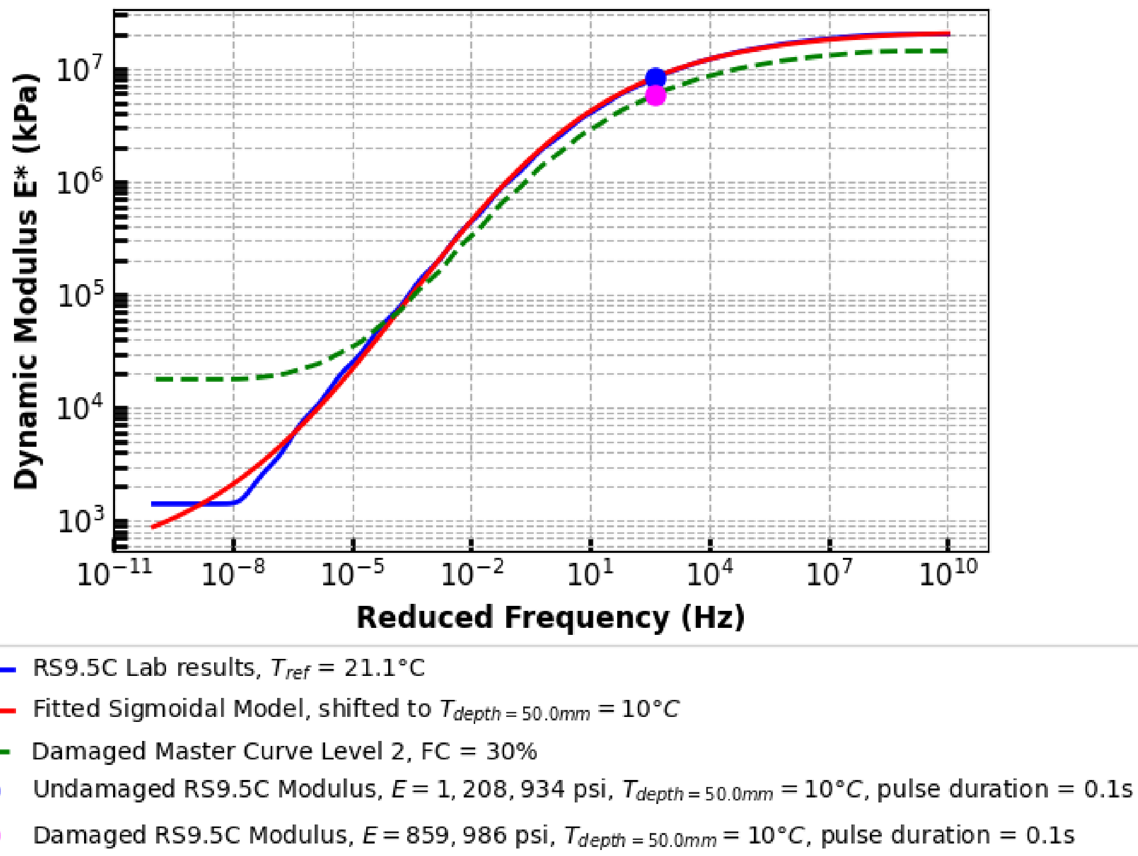

Figure 7-6. Damaged Dynamic Modulus Calculation from Undamaged Master Curve.

7.1.8 Calculation of Damage Index

The Damage Index (DI) is a crucial parameter used to evaluate the extent of damage in pavement structures. It is calculated based on the ratio of the cumulative load applied to the pavement to the load required to cause failure. The process involves using data from fatigue tests to predict the number of cycles to failure and correlating this with field performance data. The DI is expressed as the sum of the ratios of actual load repetitions to the allowable load repetitions for each load category.

Steps to Calculate Damage Index:

1. **Determine Allowable Load Repetitions (N_f):**

    - For each load category, calculate the allowable number of load repetitions to failure (N_f). This is derived from fatigue tests. Section 7.1.1 provides all the material coefficients to calculate the allowable load repetitions before failure. The NBFT is carried out only at 23°C, at 10 Hz; hence, there is a need to translate the equation to the other temperatures and loading conditions. The failure criterion, so-called D_R model, is applied here.

$$d = \ln\left[\left(\frac{0.85}{D^R_{\text{Rep}} - 0.1}\right) - 1\right] - 4.49 \times \log\left|E^*_{LVE}\right| \qquad (7\text{-}12)$$

where

$|E^*_{LVE}|$ = the representative dynamic modulus value and

$D^R{}_{\text{Rep}}$ = representative D_R value determined from the following equation.

$$D^R = 0.1 + \frac{0.85}{1 + e^{d + 4.49 \times \log\left|E^*\right|}} \qquad (7\text{-}13)$$

Closed form solution is available in FlexMAT™ that can predict the N_f at any temperature and loading conditions using the viscoelastic continuum damage theory. The form is as follows:

$$N_f = \left(\frac{D_R\left(C_{12} + \rho\right)}{C_{11} \cdot \rho}\right)^{-\frac{\rho}{C_{12}}} \cdot \left(\frac{f_r . 2^{\alpha}}{\rho\left(C_{11} - C_{12}\right)^{\alpha}}\right) . \left(\varepsilon_t . 10^6\right)^{-2\alpha} \left(\left|E^*\right| . 10^3\right)^{-2\alpha} . \frac{1}{K_1} \qquad (7\text{-}14)$$

Equation (7-14) can be used to develop the N_f equation at the reference temperature of 23°C (73°F) and the N_f equation at the temperature of interest. Rearranging these equations, N_f at the temperature of interest can be determined from the following equation:

$$N_{f@T} = k_1 \times \left(\frac{1}{\varepsilon_t}\right)^{k_2} \left[\left(\frac{D_{R,T}}{D_{R,23°C}}\right)^{-\frac{\rho}{C_{12}}} \times \frac{f_{r,T}}{f_{r,23°C}} \times \left(\frac{\left|E^*\right|_T}{\left|E^*\right|_{23°C}}\right)^{-2.\alpha}\right] \qquad (7\text{-}15)$$

2. **Record Actual Load Repetitions (N_i):**

- Record the actual number of load repetitions applied to the pavement based on the following equation.

$$\text{Monthly Traffic} = AADT \times 0.6 \times 0.5 \times 30 \qquad (7\text{-}16)$$

The following is a step-by-step explanation of each component:

1. **Average Annual Daily Traffic (AADT):**
    - This represents the Average Annual Daily Traffic (AADT) for the specific month. AADT is the total volume of vehicle traffic on a highway or road for a year divided by 365 days. It gives an average number of vehicles that pass a certain point each day over the year.
2. **Lane Distribution Factor (0.6):**
    - This factor accounts for the distribution of traffic across different lanes. Typically, traffic is not evenly distributed across all lanes, and certain lanes may carry more traffic than others. The factor 0.6 indicates that 60% of the total traffic is considered to affect the lane of interest, which is common in single-lane analysis. The research team recognizes that 0.6 is outside of the NCDOT standard policy, and thus future calibration should use the values recommended by NCDOT.
3. **Directional Distribution Factor (0.5):**
    - This factor accounts for the directional distribution of traffic. In most cases, traffic is split roughly equally in both directions on a road. The factor 0.5 assumes that half of the AADT travels in each direction.
4. **Days in a Month (30):**
    - This number represents the average number of days in a month. This factor is used to convert the daily traffic count into a monthly traffic count.

3. **Calculate Damage for Each Month Traffic:**

    - For each load category, calculate the damage using the following formula:

$$DI = \frac{N_i}{N_f} \qquad (7\text{-}17)$$

4. **Sum the Damage Indices:**

    - Sum the damage indices for all load categories to get the total Damage Index:

$$DI = \sum_{i=1}^{n} \frac{N_i}{N_f} \qquad (7\text{-}18)$$

7.1.9 Translating Damage Index to Fatigue Cracking Percentage

Once the DI is calculated, it is necessary to translate this index into a Fatigue Cracking Percentage (FC%). The relationship between the DI and FC% is defined by the following function:

$$FC = \frac{100}{1+e^{C_2(2-\log_{10} DI)}} \tag{7-19}$$

where C_2 is a parameter that has been determined to be 7.4.

Adjustments for Pavement Thickness

When applying this function to predict FC%, it is important to adjust for variations in pavement thickness. Specifically, very thin pavements (below 2 inches) and thick pavements (around 6 inches) require calibration to ensure accurate predictions.

To achieve this calibration, a regression analysis is performed using field-measured FC% data. This analysis provides a calibration factor, β_{f1} , which adjusts the predicted FC% values to better match observed field performance.

$$\text{modified DI}=\frac{1}{\beta_{f_1}}\sum\frac{N}{N_f} \tag{7-20}$$

$$FC\% = \frac{100}{1+e^{7.4(2-log_{10}modified\ DI)}} \tag{7-21}$$

By following these steps, the DI values of the selected pavement sections were predicted. The DI values were compared against the FC% and the β_{f1} value for each section was determined to minimize the error between the predicted and measured FC% values. Figure 7-7 shows the fitting of FC% as a function of modified DI with the section-specific β_{f1} values. The data in Figure 7-7 are replotted in Figure 7-8 with line of equality to show the comparison of the measured and fitted data more clearly.

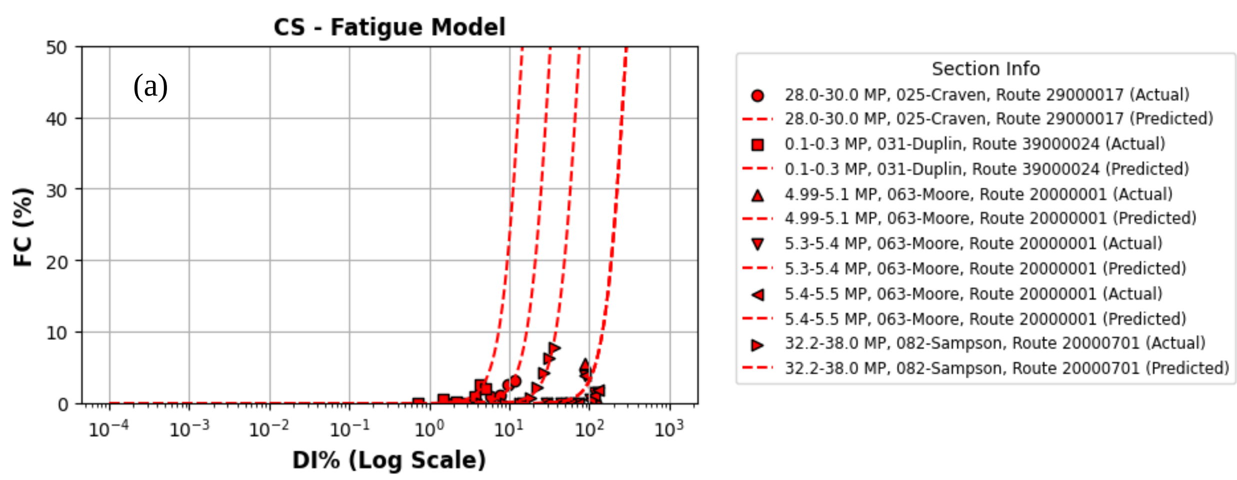

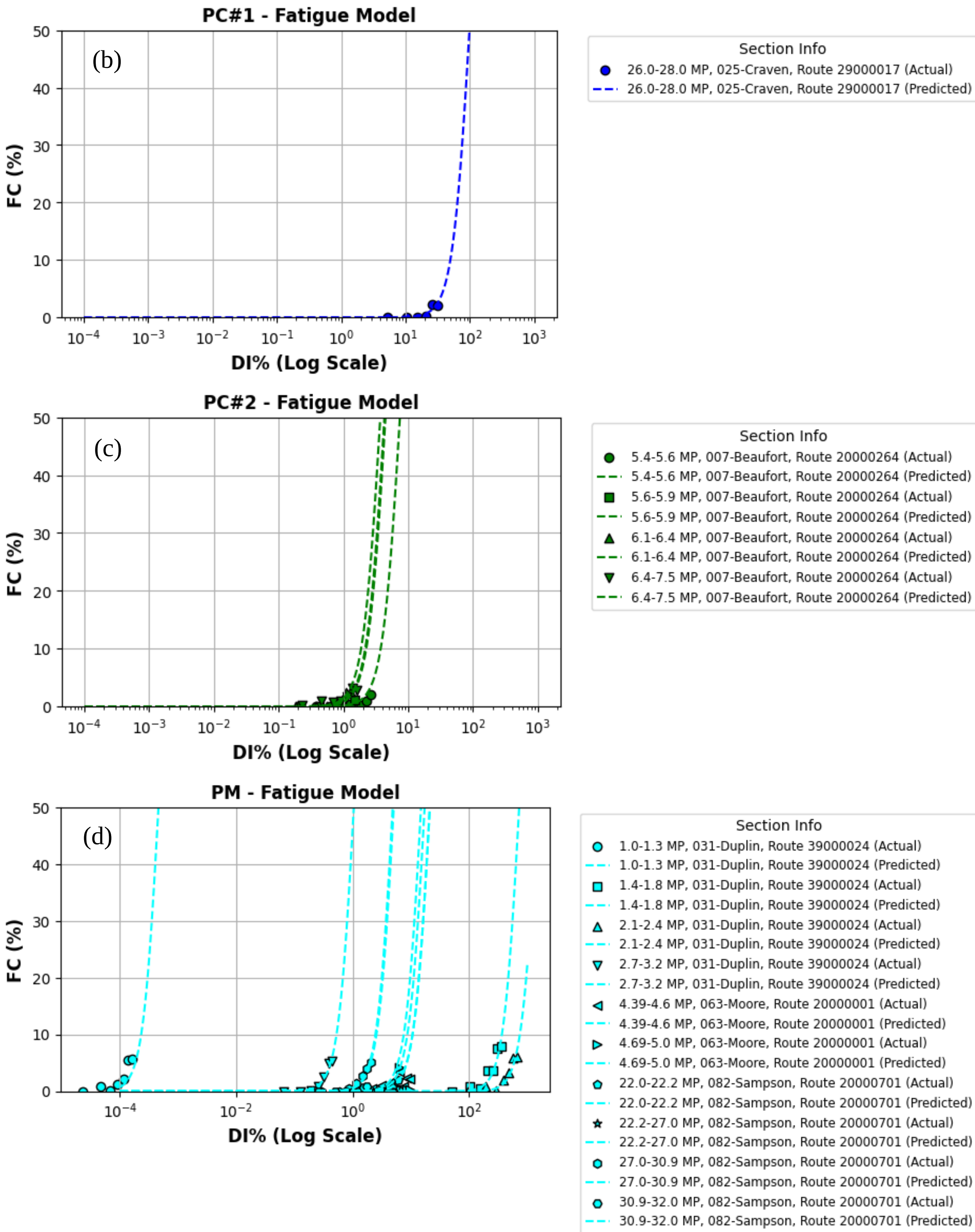

Figure 7-7. FC% versus log DI relationship of the selected sections with measured and fitted data.

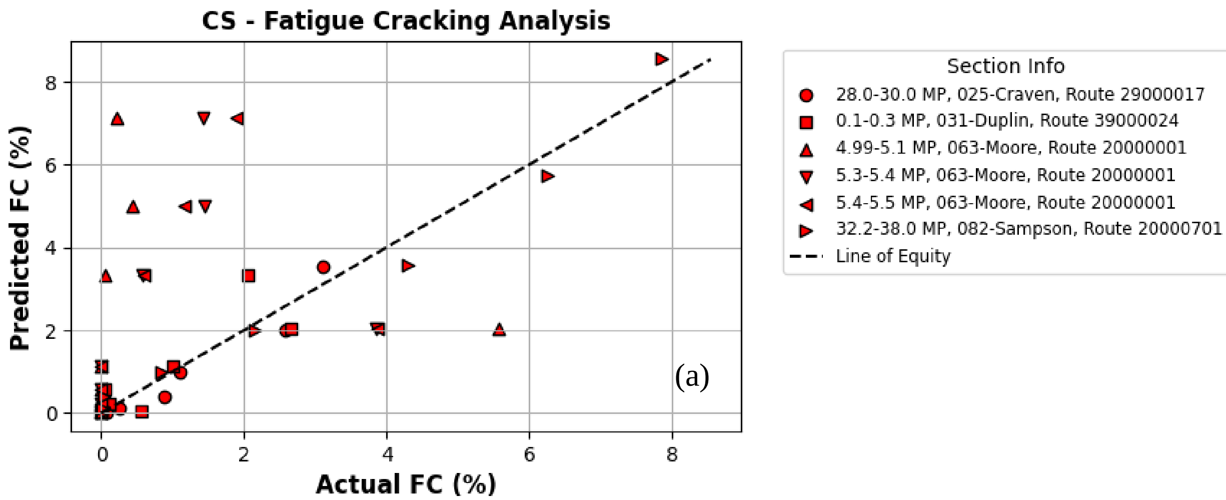
CS - Fatigue Cracking Analysis
Predicted FC (%)
Actual FC (%)
0
2
4
6
8
Section Info
28.0-30.0 MP, 025-Craven, Route 29000017
0.1-0.3 MP, 031-Duplin, Route 39000024
4.99-5.1 MP, 063-Moore, Route 20000001
5.3-5.4 MP, 063-Moore, Route 20000001
5.4-5.5 MP, 063-Moore, Route 20000001
32.2-38.0 MP, 082-Sampson, Route 20000701
Line of Equity
(a)

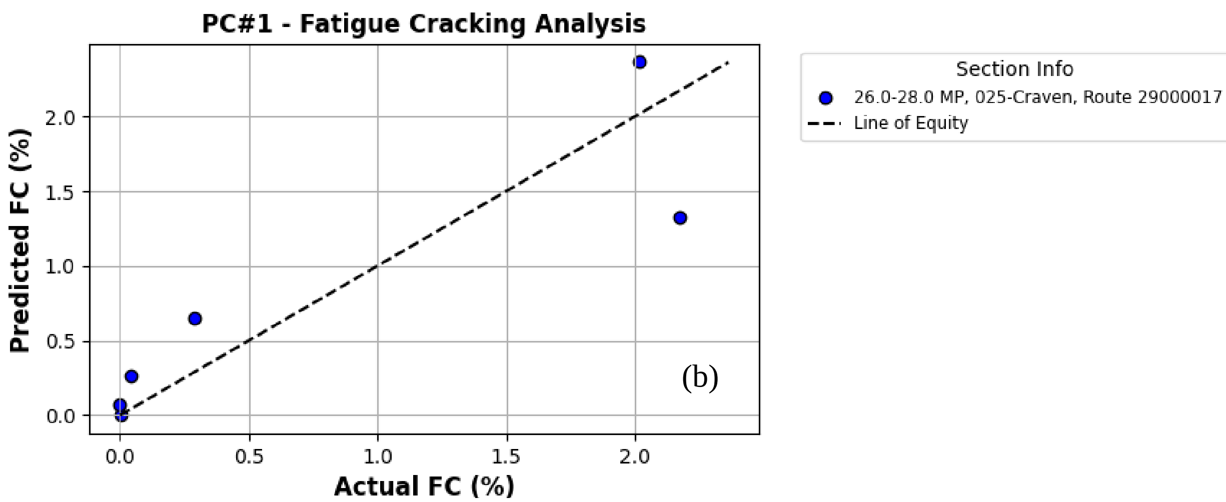
PC#1 - Fatigue Cracking Analysis
Predicted FC (%)
Actual FC (%)
0.0
0.5
1.0
1.5
2.0
Section Info
26.0-28.0 MP, 025-Craven, Route 29000017
Line of Equity
(b)

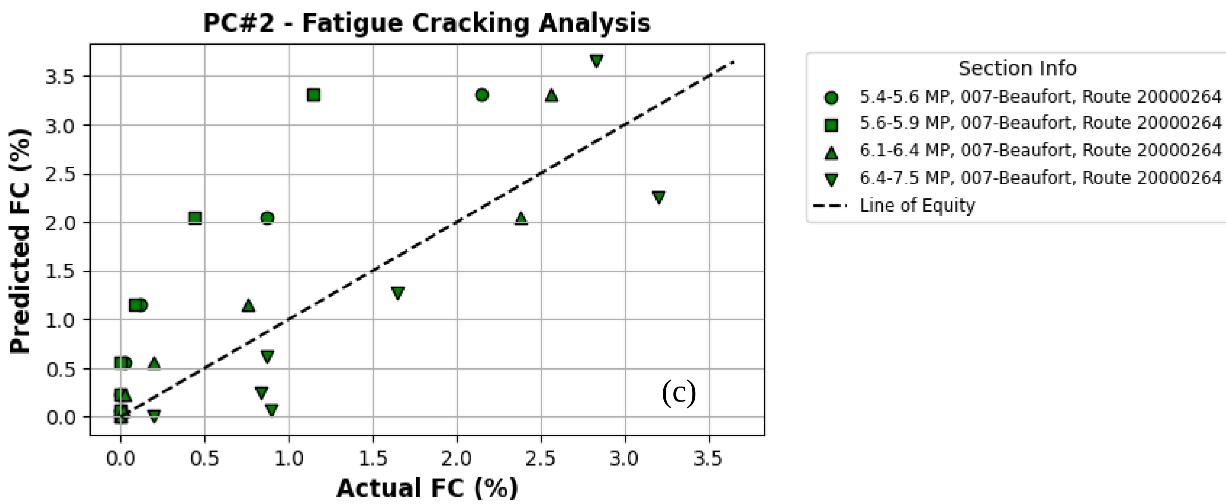
PC#2 - Fatigue Cracking Analysis
Predicted FC (%)
Actual FC (%)
0.0
0.5
1.0
1.5
2.0
2.5
3.0
3.5
Section Info
5.4-5.6 MP, 007-Beaufort, Route 20000264
5.6-5.9 MP, 007-Beaufort, Route 20000264
6.1-6.4 MP, 007-Beaufort, Route 20000264
6.4-7.5 MP, 007-Beaufort, Route 20000264
Line of Equity
(c)

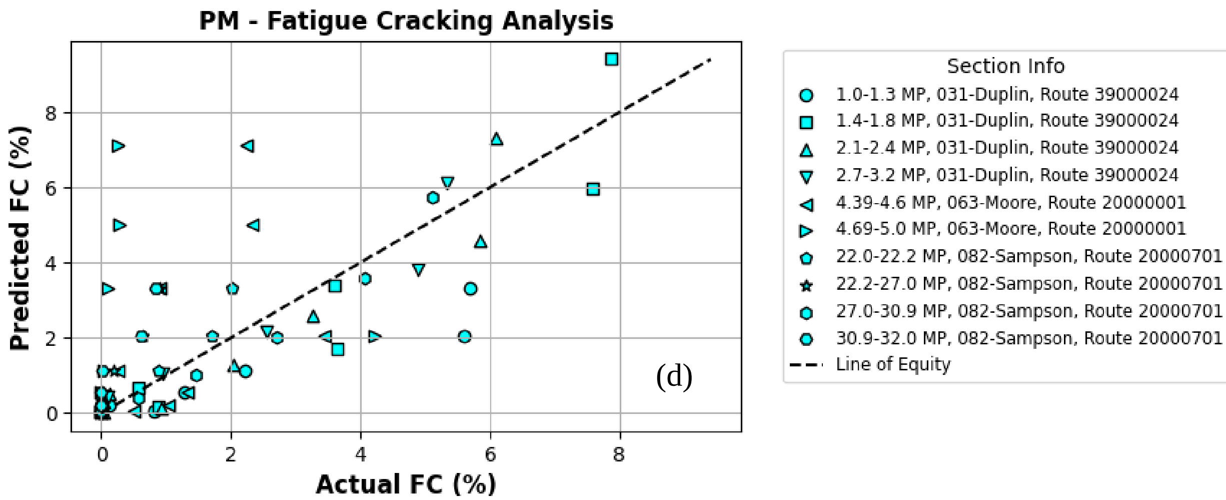

Figure 7-8. Comparison of predicted and fitted data.

Figure 7-9 illustrates the relationship between the calibration factor β_{f1} and asphalt thickness. Note that the data from Pender County sections are not shown in this figure because the PMS data indicated that no significant cracking was observed after the asphalt overlay in these sections. Also, the β_{f1} values from the control sections of the selected routes were not included in this figure because they form a different trend against the asphalt layer thickness compared to that of the geosynthetic-reinforced sections.

The calibration factor β_{f1} was used to adjust the predicted FC% to better match observed field performance, particularly for pavements of varying thicknesses. The data points on the graph represent different reinforcement types (PC#1, PC#2, PM), and the fitted curve represents the exponential decay model used to describe the relationship. Thus, the equation based on the fitted curve is:

$$\beta_{f_1} = 370 \times e^{-2.34 \times h_{ac}} \tag{7-22}$$

where h_{ac} = thickness of existing AC layer in inches.

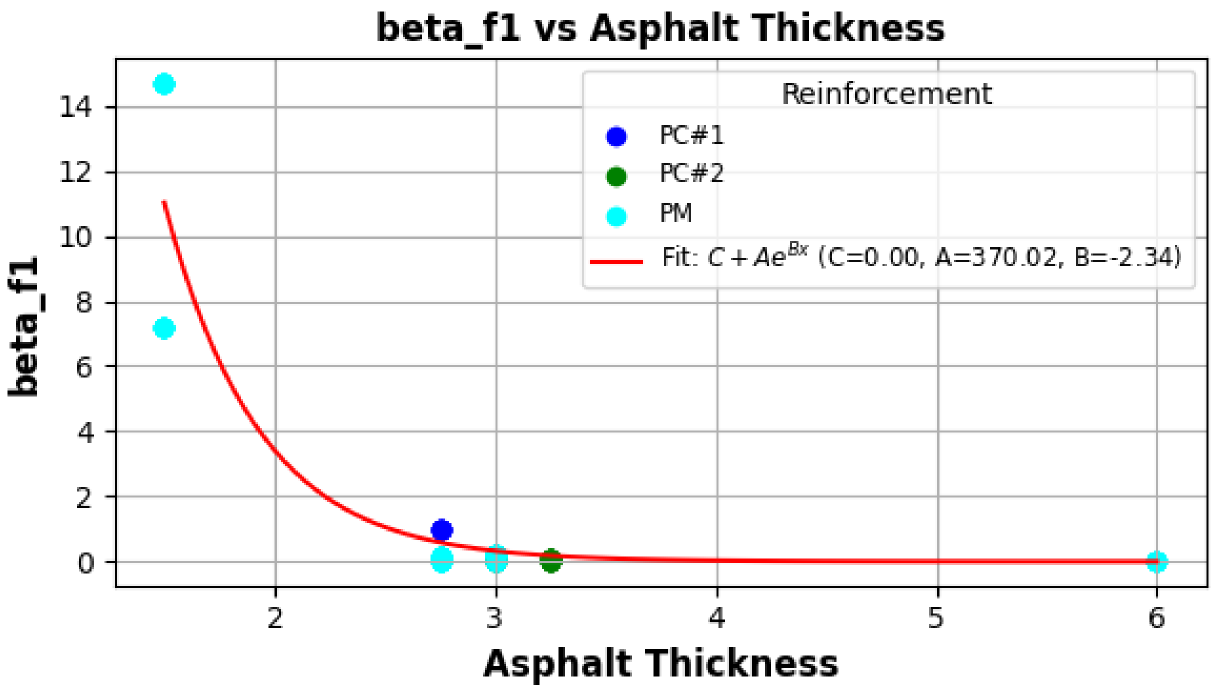

Figure 7-9. Relationship between calibration factor β_{f1} and asphalt thickness.

The developed procedure was verified using the data from the US 1 sections. The US 1 project included five sections, including the control, chip seal section, a section reinforced with paving fabric, and two sections with different paving mat products. Two paving mat sections are used in this verification study. The verification results are shown in Figure 7-10. The developed procedure underpredicted FC% of the PM section with the milepost between 4.47 and 4.62 slightly, but in general the predicted FC% followed the line of equality. For the PM section with the milepost between 4.64 and 4.8, the developed procedure overpredicted FC% when actual FC% is zero (i.e., no cracking observed in the condition survey data) but slightly underpredicted FC% when actual FC% is about 4%. Note that FC% predicted from the developed procedure is based on propagation of bottom-up reflective cracking; therefore, the overprediction of FC% when actual FC% is zero may mean that significant damage occurred in the pavement even though no cracks are observed on the pavement surface. In general, the verification plot in Figure 7-10 indicates that the developed procedure predicts the cracking performance of paving mat reinforced sections reasonably well. More sections with higher cracking percentages are needed to fully validate the predictive methodology.

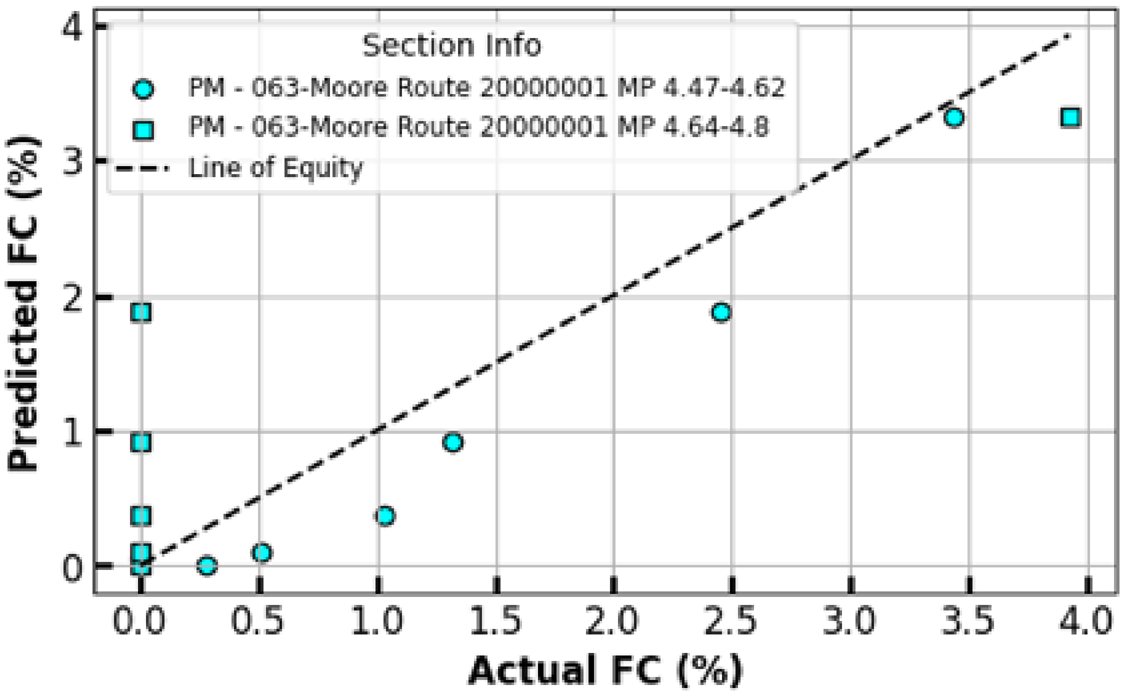

Figure 7-10. Verification of the developed procedure with calibration factor β_{f1}.

7.1.10 Summary on the Calibration of Laboratory Data to Field Performance

The calibration process is essential for translating laboratory findings into accurate field performance predictions. It involves integrating data from two major categories: field data and laboratory data. This calibration procedure ensures that the predictive models developed from controlled laboratory experiments can reliably estimate real-world pavement behavior. The following section describes the step-by-step procedure involved in calibration and the steps designers should follow to predict the geosynthetic reinforced pavements.

Field Data

Field data collection encompasses two levels:

Level 1: Falling Weight Deflectometer (FWD) Measurements

1. Conduct FWD tests on the pavement site to measure deflections.
2. Obtain the Enhanced Integrated Climatic Model (EICM) data for the location, which provides the average monthly temperature at the mid-depth of the surface asphalt concrete (AC) layer.
3. Using the measured FWD temperature and the temperature correction equation, calculate the deflections for other months in a year at different temperatures.
4. Employ the predictive equation to determine the tensile strain at the bottom of the overlay, utilizing inputs such as AC layer thickness, Surface Curvature Index (SCI), Base Damage Index (BDI), and Base Curvature Index (BCI).

Level 2: Fatigue Cracking Percentage (FC%) Measurements

1. Measure the total FC% using the available Pavement Management System (PMS) data.

2. Calculate the damage factor (d_{AC}) of the AC layer from the FC% data.

3. Obtain the average monthly temperatures for a year from the EICM data.

4. Based on the design speed and existing layer thickness, determine the damaged dynamic modulus of the AC layer for different average monthly temperatures using the standard undamaged mixture sigmoidal parameters.

5. Utilize EverstressFE software to calculate the deflection bowl of the FWD for different months and the tensile strain at the bottom of the overlay using the proposed overlay strain equation.

The primary goal of both levels is to measure the tensile strain at the bottom of the overlay.

Laboratory Data

Three sets of laboratory data are required:

1. AC properties from dynamic modulus and uniaxial fatigue tests.

2. Notched Beam Fatigue Test (NBFT) data.

3. The dynamic modulus data is used to obtain the sigmoidal function parameters of the undamaged AC mix.

4. The fatigue test data provides two parameters that help translate the NBFT results from one temperature and frequency to any other temperature and frequency through a closed-loop solution.

5. The NBFT data provides the damage resistance of the geosynthetic-reinforced mixture at 23°C and 10 Hz.

The standard equation for the four-point bending fatigue test is modified using the closed-loop solution, allowing the prediction of the allowable number of load repetitions to failure (N_f) for different pavement conditions.

Calibration Process

1. Using the tensile strain data from the field and the N_f relationship from the laboratory study, calculate the N_f for field conditions.

2. Knowing the traffic conditions on the field, calculate the actual number of load repetitions (N) from the Average Annual Daily Traffic (AADT) data.

3. Determine the Damage Index (DI), which is the ratio of N/N_f.

4. Calibrate the field and laboratory data using the measured total FC% and the calculated DI for each month and cumulative DI for multiple years.

5. Utilize the standard relationship between FC% and log (DI) where C_2 is a fixed parameter at 7.4, and β_{f1} is the calibration factor.

6. Calculate β_{f1} by fitting the field-measured FC% data to the modified DI values calculated from DI/β_{f1}.

7. Establish the relationship between β_{f1} and the asphalt thickness using the fitted data.

8. Using pavement sections that are not used in the development of the predictive procedure, verify the predictive capability of β_{f1} by comparing the predicted FC% values with measured field data.

Once the calibration factor β_{f1} is determined, designers can follow either Level 1 or Level 2 methods to calculate N_f, modify N_f with β_{f1}, and then calculate DI and FC% for their specific pavement conditions.

This comprehensive calibration process ensures that the laboratory-derived predictive models accurately represent field performance, enabling informed decision-making for pavement design and maintenance strategies.

Chapter 8. Conclusions and Recommendations for Future Work

This comprehensive research project aimed to develop a field-calibrated method for performance prediction of geosynthetic-reinforced asphalt overlays. Through a multifaceted approach, the study addressed several critical aspects, leading to significant findings and contributions to the design of asphalt overlays with geosynthetic interlayer systems. The key outcomes and their implications are summarized below:

Evaluation of Field Distress Data:

- The analysis of field data from the NCDOT PMS provided insights into the performance of various geosynthetic-reinforced pavement sections across the state.
- The data highlighted the potential benefits of using geosynthetic interlayers in mitigating reflective cracking and extending the service life of asphalt overlays, showcasing their practical applications in pavement maintenance and rehabilitation strategies.

Laboratory Testing and Crack Resistance Modeling:

- Notched Beam Fatigue Tests (NBFTs) were conducted on geosynthetic-reinforced and unreinforced beam specimens to quantify their crack resistance capacity under controlled laboratory conditions.
- The results demonstrated a significant improvement in crack resistance when incorporating geosynthetic interlayers compared to unreinforced scenarios.
- Predictive models were developed to correlate tensile strain with crack resistance, enabling the estimation of crack resistance capacity based on tensile strain measurements.

Predictive Model for Tensile Strain:

- A novel approach was adopted, utilizing Jung's method, to predict the tensile strain at the bottom of the asphalt overlay.
- This method directly utilizes deflection basin parameters, overcoming the limitations of relying solely on pavement response analysis.
- The approach provides a more reliable estimation of tensile strain under the overlay, aligning better with observed field conditions and reducing the risk of spurious results.

Comprehensive Procedure for Field Performance Prediction:

- The research team developed a comprehensive procedure for translating laboratory data into field performance predictions, bridging the gap between controlled experiments and real-world applications.

- The procedure involves temperature correction models for deflections, calculation of pulse durations for dynamic modulus analysis, determination of damaged dynamic modulus, and the calculation of a Damage Index.
- The Damage Index was correlated with field-measured fatigue cracking percentages. Calibration factors were developed for different geosynthetic interlayer systems as a function of asphalt layer thickness.

Performance Prediction Procedure for Geosynthetic-Reinforced Asphalt Overlays:

- The developed methodology provides a step-by-step procedure for predicting the field performance of geosynthetic-reinforced asphalt overlays, thus offering a practical framework for transportation agencies to optimize pavement performance, extend service life, and enhance the cost-effectiveness of their maintenance and rehabilitation strategies.

Limitations and Future Work:

- The accuracy of the predictive models is limited by the availability and reliability of data from the PMS.
- Further research and data collection efforts are recommended to refine and improve the predictive models, ensuring their robustness and applicability across various pavement conditions and scenarios.
- Ongoing validation and refinement of the developed guidelines using a large number of geosynthetic-reinforced pavement sections with varying degrees of cracking are crucial to maintain their relevance and accuracy in predicting pavement life extensions due to geosynthetic interlayer systems.

Overall, this research project has made significant contributions to the understanding and implementation of geosynthetic interlayers in asphalt overlays. The developed guidelines and predictive models offer a comprehensive and practical approach to enhancing pavement performance, extending service life, and optimizing maintenance and rehabilitation strategies for transportation agencies worldwide.

REFERENCES

AASHTO. 2017a. *Bulk Specific Gravity (Gmb) and Density of Compacted Hot Mix Asphalt (HMA) Using Automatic Vacuum Sealing Method*. Standard. Washington DC, USA: American Association of State and Highway Transportation Officials.

AASHTO. 2017b. *Standard Method of Test for Determining the Fatigue Life of Compacted Asphalt Mixtures Subjected to Repeated Flexural Bending*. Standard. Washington DC, USA: American Association of State and Highway Transportation Officials.

AASHTO. 2019. *Provisional Standard Method of Test for Determining the Dynamic Modulus for Asphalt Mixtures Using Small Specimens in the Asphalt Mixture Performance Tester (AMPT)*. Standard. Washington DC, USA: American Association of State and Highway Transportation Officials.

AASHTO. 2020a. *Standard Method of Test for Theoretical Maximum Specific Gravity (Gmm) and Density of Asphalt Mixtures*. Standard. Washington DC, USA: American Association of State and Highway Transportation Officials.

AASHTO. 2020b. *Standard Practice for Recovering Residue from Emulsified Asphalt Using Low-Temperature Evaporative Techniques*. Standard. Washington DC, USA: American Association of State and Highway Transportation Officials.

AASHTO. 2020c. *Standard Method of Test for Determining the Rheological Properties of Asphalt Binder Using a Dynamic Shear Rheometer (DSR)*. Standard. Washington DC, USA: American Association of State and Highway Transportation Officials.

AASHTO. 2021. *Standard Practice for Preparation of Cylindrical Performance Test Specimens Using the Superpave Gyratory Compactor (SGC)*. Standard. Washington DC, USA: American Association of State and Highway Transportation Officials.

Al-Qadi, I. L., S. H. Carpenter, Z. Leng, H. Ozer, and J. Trepanier. 2008. *Tack coat optimization for HMA overlays: Laboratory testing*. Technical Report. Rantoul, IL, USA: Illinois Center for Transportation.

Amini, F. 2005. *Potential applications of paving fabrics to reduce reflective cracking.* 45. Technical Report. Jackson, MS, USA: Jackson State University.

Asphalt Institute (Ed.). 1991. *Thickness Design-Full depth Asphalt Pavement Structures for Highways and Streets*. Manual Series. College Park, MD, USA: The Asphalt Institute.

ASTM. 2010. *Test Method for Determining Fatigue Failure of Compacted Asphalt Concrete Subjected to Repeated Flexural Bending*. Standard. West Conshohocken, PA, USA: American Standards for Testing Materials International.

Bae, A., L. N. Mohammad, M. A. Elseifi, J. Button, and N. Patel. 2010. “Effects of Temperature on Interface Shear Strength of Emulsified Tack Coats and Its Relationship to Rheological

Properties.” *Transportation Research Record*, 2180 (1): 102–109. SAGE Publications Inc. https://doi.org/10.3141/2180-12.

Baek, J. 2010. “Modeling reflective cracking development in hot-mix asphalt overlays and quantification of control techniques.” *ProQuest Dissertations and Theses*. Ph.D. Urbana-Champaign, IL, USA: University of Illinois at Urbana-Champaign.

Benedetto, H. D., C. de L. Roche, H. Baaj, A. Pronk, and R. Lundström. 2004. “Fatigue of bituminous mixtures.” *Mat. Struct.*, 37 (3): 202–216. https://doi.org/10.1007/BF02481620.

Blankenship, P., N. Iker, and J. Drbohlav. 2004. “Interlayer and Design Considerations to Retard Reflective Cracking.” *Transportation Research Record*, 1896 (1): 177–186. SAGE Publications Inc. https://doi.org/10.3141/1896-18.

Bognacki, C. J., A. Frisvold, and T. Bennert. 2007. “Investigation of asphalt pavement slippage failures on runway 4R-22L, Newark International Airport.” *New Directions in Airport Technology*, 14. Atlantic City, NJ, USA: Federal Aviation Administration.

Boulangé, L., and F. Sterczynskia. 2012. “Study of Interfacial Interactions between Bitumen and Various Aggregates Used in Road Construction.” *null*, 26 (1–3): 163–173. Taylor & Francis. https://doi.org/10.1163/016942411X569372.

BS EN. 2019. *Specimen prepared by roller compactor*. Bituminous mixtures. Test methods., 22. Standard No. EN 12697-33. London, UK: British Standards Institution.

Button, J. W., and R. L. Lytton. 1987. “Evaluation of fabrics, fibers and grids in overlays.” *Structural Design of Asphalt Pavements Vol 1*, 925–934. Ann Arbor, MI, USA.

Button, J. W., and R. L. Lytton. 2007. “Guidelines for Using Geosynthetics with Hot-Mix Asphalt Overlays to Reduce Reflective Cracking.” *Transportation Research Record*, 2004 (1): 111–119. SAGE Publications Inc. https://doi.org/10.3141/2004-12.

Canestrani, F., A. Grilli, F. Santagata, and A. Virgili. 2006. “Interlayer shear effects of geosynthetic reinforcements.” Qubec City, Canada.

Canestrari, F., G. Ferrotti, M. Abuaddous, and E. Pasquini. 2016. “Geocomposite-Reinforcement of Polymer-Modified Asphalt Systems.” *8th RILEM International Symposium on Testing and Characterization of Sustainable and Innovative Bituminous Materials*, F. Canestrari and M. N. Partl, eds., 383–395. Dordrecht: Springer Netherlands.

Chakroborty, P., and A. Das. 2017. *Principles of Transportation Engineering*. Delhi, India: Prentice Hall India Pvt., Limited.

Cho, S. H. 2016. “Evaluation of interfacial stress distribution and bond strength between asphalt pavement layers.” Ph.D Dissertation. Raleigh, NC, USA: North Carolina State University.

Cho, S. H., A. Karshenas, A. A. Tayebali, M. N. Guddati, and Y. R. Kim. 2017a. “A mechanistic approach to evaluate the potential of the debonding distress in asphalt pavements.” *International Journal of Pavement Engineering*, 18 (12): 1098–1110. Taylor & Francis. https://doi.org/10.1080/10298436.2016.1149837.

Cho, S. H., S. A. Safavizadeh, and Y. R. Kim. 2017b. “Verification of the applicability of the time–temperature superposition principle to interface shear stiffness and strength of GlasGrid-reinforced asphalt mixtures.” *Road Materials and Pavement Design*, 18 (4): 766–784. Taylor & Francis. https://doi.org/10.1080/14680629.2016.1189350.

Cho, S.-H., and Y. R. Kim. 2016. “Verification of Time–Temperature Superposition Principle for Shear Bond Failure of Interlayers in Asphalt Pavements.” *Transportation Research Record*, 2590 (1): 18–27. SAGE Publications Inc. https://doi.org/10.3141/2590-03.

Christensen, D. W., and D. A. Anderson. 1992. “Interpretation of dynamic mechanical test data for paving grade asphalt cements (with discussion).” *Journal of the Association of Asphalt Paving Technologists*, 61: 67–116. Association of Asphalt Paving Technologists (AAPT).

Collop, A. C., M. H. Sutanto, G. D. Airey, and R. C. Elliott. 2011. “Development of an automatic torque test to measure the shear bond strength between asphalt.” *Constr. Build. Mater.*, Composite Materials and Adhesive Bonding Technology, 25 (2): 623–629. https://doi.org/10.1016/j.conbuildmat.2010.07.030.

Ferrotti, G., F. Canestrari, E. Pasquini, and A. Virgili. 2012. “Experimental evaluation of the influence of surface coating on fiberglass geogrid performance in asphalt pavements.” *Geotextiles and Geomembranes*, 34: 11–18. https://doi.org/10.1016/j.geotexmem.2012.02.011.

Ferrotti, G., F. Canestrari, A. Virgili, and A. Grilli. 2011. “A strategic laboratory approach for the performance investigation of geogrids in flexible pavements.” *Construction and Building Materials*, 25 (5): 2343–2348. https://doi.org/10.1016/j.conbuildmat.2010.11.032.

FHWA. 2016. *Tack Coat Best Practices*. 17. Technical Bulletin. Washington DC, USA: Federal Highway Administration.

Hachiya, Y., S. Umeno, and K. Sato. 1997. “Effect of tack coat on bonding characteristics at interface between asphalt concrete layers.” *Doboku Gakkai Ronbunshu*, 1997 (571): 199–209. Japan Society of Civil Engineers.

Huesker. 2015. “HaTelit® Asphalt Reinforcement Grid Installation Guideline.” <https://www.huesker.com.au/fileadmin/Media/Brochures/AUS/HaTelit_C_Installation_Guidelines_AUS.pdf>.

Joel Sprague, C., S. Allen, and W. Tribbett. 1998. “Tensile Properties of Asphalt Overlay Geosynthetic Reinforcement.” *Transportation Research Record*, 1611 (1): 65–69. SAGE Publications Inc. https://doi.org/10.3141/1611-08.

Khodaei, A., and SH. Falah. 2009. “Effects of geosynthetic reinforcement on the propagation of reflection cracking in asphalt overlays.” *International Journal of Civil Engineering*, 7 (2): 131–140.

Khweir, K., and D. Fordyce. 2003. “Influence of layer bonding on the prediction of pavement life.” *Proceedings of the Institution of Civil Engineers - Transport*, 156 (2): 73–83. https://doi.org/10.1680/tran.2003.156.2.73.

Kim, Y. R., S. R. Ranjithan, J. D. Troxler, and B. Xu. 2000. *Assessing Pavement Layer Condition Using Deflection Data*. 198. Technical Report. Raleigh, NC, USA: North Carolina State University.

Kim, Y. R., A. A. Tayebali, G. N. Murthy, A. Karshenas, and S.-H. Cho. 2015. *Surface Layer Bond Stress and Strength*. 289. Technical Report. Raleigh, NC, USA: North Carolina State University.

Kruntcheva Mariana R., Collop Andrew C., and Thom Nicholas H. 2005. “Effect of Bond Condition on Flexible Pavement Performance.” *Journal of Transportation Engineering*, 131 (11): 880–888. American Society of Civil Engineers. https://doi.org/10.1061/(ASCE)0733-947X(2005)131:11(880).

Kuai, H. D., H. J. Lee, J. H. Lee, and S. Mun. 2010. “Fatigue Crack Propagation Model of Asphalt Concrete Based on Viscoelastic Fracture Mechanics.” *Transportation Research Record*, 2181 (1): 11–18. https://doi.org/10.3141/2181-02.

Lytton, R. L. 1989. “Use of geotextiles for reinforcement and strain relief in asphalt concrete.” *Geotextiles and Geomembranes*, 8 (3): 217–237. https://doi.org/10.1016/0266-1144(89)90004-6.

Makowski, L., D. L. Bischoff, P. Blankenship, D. Sobczak, and F. Haulter. 2005. “Wisconsin Experiences with Reflective Crack Relief Projects.” *Transportation Research Record*, 1905 (1): 44–55. SAGE Publications Inc. https://doi.org/10.1177/0361198105190500105.

Mohammad, L. N., M. A. Elseifi, A. Bae, and N. Patel. 2012. *Optimization of Tack Coat for HMA Placement*. NCHRP 9-40, 146. Technical Report. Washington, D.C., USA: The National Academies Press.

Mohammad, L. N., M. A. Elseifi, R. Das, and W. Cao. 2018. *Validation of the Louisiana Interlayer Shear Strength Test for Tack Coat*. 25458. Technical Report. Washington, D.C., USA: Transportation Research Board.

Mohammad, L. N., M. Hassan, and N. Patel. 2011. “Effects of Shear Bond Characteristics of Tack Coats on Pavement Performance at the Interface.” *Transportation Research Record*, 2209 (1): 1–8. https://doi.org/10.3141/2209-01.

Mohammad, L. N., M. Raqib, and B. Huang. 2002. “Influence of Asphalt Tack Coat Materials on Interface Shear Strength.” *Transportation Research Record*, 1789 (1): 56–65. https://doi.org/10.3141/1789-06.

Monismith, C. L., J. A. Epps, and F. N. Finn. 1985. “Improved asphalt mix design (with discussion).” *Association of Asphalt Paving Technologists Proc,* 340–406. Minnesota, USA.

Mukhtar, M. T., and B. J. Dempsey. 1996. *Interlayer Stress Absorbing Composite (ISAC) for Mitigating Reflection Cracking in Asphalt Concrete Overlays*. Technical Report. Urbana-Champaign, IL, USA: University of Illinois at Urbana-Champaign.

NCDOT. 2018. *Asphalt Quality Management System*. 364. Guide. NC, USA: North Carolina Department of Transportation.

Park, S. W., Y. Richard Kim, and R. A. Schapery. 1996. “A viscoelastic continuum damage model and its application to uniaxial behavior of asphalt concrete.” *Mechanics of Materials,* 24 (4): 241–255. Elsevier. https://doi.org/10.1016/S0167-6636(96)00042-7.

Pasquini, E., M. Bocci, G. Ferrotti, and F. Canestrari. 2013. “Laboratory characterisation and field validation of geogrid-reinforced asphalt pavements.” *null*, 14 (1): 17–35. Taylor & Francis. https://doi.org/10.1080/14680629.2012.735797.

Pasquini, E., G. Giacomello, M. Pasetto, and F. Canestrari. 2015. “Laboratory evaluation of the effect of low-temperature application of warm-mix asphalts on interface shear strength.” *Construction and Building Materials,* 88 (Complete): 56–63. https://doi.org/10.1016/j.conbuildmat.2015.04.009.

Peattie, K. R. 1980. “The incidence and investigation of slippage failures.” *The performance of rolled asphalt road surfacings*. The institution of Civil Engineers.

Petersen, D., R. Link, M. Wagoner, W. Buttlar, and G. Paulino. 2005. “Development of a Single-Edge Notched Beam Test for Asphalt Concrete Mixtures.” *J. Test. Eval.,* 33 (6): 12579. https://doi.org/10.1520/JTE12579.

Raab, C., and M. N. Partl. 2004. “Interlayer shear performance: experience with different pavement structures.” *Proceedings of the 3rd Eurasphalt and Eurobitume Congress*. Vienna, Austria.

Raposeiras, A. C., D. Castro-Fresno, A. Vega-Zamanillo, and J. Rodriguez-Hernandez. 2013. “Test methods and influential factors for analysis of bonding between bituminous pavement layers.” *Construction and Building Materials,* 43: 372–381. https://doi.org/10.1016/j.conbuildmat.2013.02.011.

Rigo, J.-M., R. Degeimbre, and L. Francken. 2014. *Reflective cracking in pavements: state of the art and design recommendations*. CRC Press.

Safavizadeh, S. A. 2015. “Fatigue and fracture characterization of GlasGrid® reinforced asphalt concrete pavement.” Ph.D Dissertation. Raleigh, NC, USA: North Carolina State University.

Safavizadeh, S. A., and Y. R. Kim. 2017. “DIC Technique to Investigate Crack Propagation in Grid-Reinforced Asphalt Specimens.” *Journal of Materials in Civil Engineering,* 29 (6):

04017011. American Society of Civil Engineers. https://doi.org/10.1061/(ASCE)MT.1943-5533.0001839.

Schapery, R. A. 1962. *A simple collocation method for fitting viscoelastic models to experimental data*. GALCIT, 15. Technical Report. Pasadena, CA, USA: California Institute of Technology.

Seo, Y., Y. Kim, M. W. Witczak, and R. Bonaquist. 2002. "Application of Digital Image Correlation Method to Mechanical Testing of Asphalt-Aggregate Mixtures." *Transp.Res.Rec.*, 1789 (1): 162–172. SAGE Publications Inc. https://doi.org/10.3141/1789-18.

Shell International Petroleum Company. 1978. *Shell pavement design manual: Asphalt pavements and overlays for road traffic*. London, UK: Shell International Petroleum Company.

Si, Z., Little D. N., and Lytton R. L. 2002. "Characterization of Microdamage and Healing of Asphalt Concrete Mixtures." *Journal of Materials in Civil Engineering*, 14 (6): 461–470. American Society of Civil Engineers. https://doi.org/10.1061/(ASCE)0899-1561(2002)14:6(461).

Su, K., L. Sun, Y. Hachiya, and R. Maekawa. 2008. "Analysis of shear stress in asphalt pavements under actual measured tire-pavement contact pressure." *Proceedings of the 6th ICPT, Sapporo, Japan*, 11–18.

Sudarsanan, N., R. Karpurapu, and V. Amirthalingam. 2019. "Investigations on fracture characteristics of geosynthetic reinforced asphalt concrete beams using single edge notch beam tests." *Geotextiles and Geomembranes*, 47 (5): 642–652. https://doi.org/10.1016/j.geotexmem.2019.103461.

Sudarsanan, N., R. Karpurapu, and V. Amrithalingam. 2015. "State-of-the Art Summary of Geosynthetic Interlayer Systems for Retarding the Reflective Cracking." *Indian Geotech J*, 45 (4): 472–487. https://doi.org/10.1007/s40098-015-0161-7.

Sudarsanan, N., R. Karpurapu, and V. Amrithalingam. 2016. "Critical review on the bond strength of geosynthetic interlayer systems in asphalt overlays." *Japanese Geotechnical Society Special Publication*, 2 (67): 2296–2301. https://doi.org/10.3208/jgssp.IGS-09.

Sudarsanan, N., R. Karpurapu, and V. Amrithalingam. 2018a. "An investigation on the interface bond strength of geosynthetic-reinforced asphalt concrete using Leutner shear test." *Construction and Building Materials*, 186: 423–437. https://doi.org/10.1016/j.conbuildmat.2018.07.010.

Sudarsanan, N., S. R. Mohapatra, R. Karpurapu, and V. Amirthalingam. 2018b. "Use of Natural Geotextiles to Retard Reflection Cracking in Highway Pavements." *Journal of Materials in Civil Engineering*, 30 (4): 04018036. American Society of Civil Engineers. https://doi.org/10.1061/(ASCE)MT.1943-5533.0002195.

Sutanto, M. H. 2009. "Assessment of bond between asphalt layers." Ph. D Dissertation. Nottingham, UK: University of Nottingham.

Tashman, L., K. Nam, and A. T. Papagiannakis. 2006. *Evaluation of the influence of tack coat construction factors on the bond strength between pavement layers*. 91. Technical Report. Pullman, WA, USA: Washington State Department of Transportation Olympia.

Tayebali, A. A., G. M. Rowe, and J. B. Sousa. 1994. *Fatigue response of asphalt-aggregate mixtures*. Technical Report. Washington DC, USA: National Research Council.

Tencate. 2019. “Installation Guidelines for Tencate Mirafi® MPG Composite Paving Grids.” <https://www.tencategeo.us/media/4feb9b04-41fe-4e4b-a78a-0656ab1318f7/3NVyZw/TenCate%20Geosynthetics/Documents%20AMER/Installation%20Guidelines/Pavement%20Solutions/IG_MPG010720>.

Tozzo, C., N. Fiore, and A. D’Andrea. 2014. “Dynamic shear tests for the evaluation of the effect of the normal load on the interface fatigue resistance.” *Construction and Building Materials*, 61: 200–205. https://doi.org/10.1016/j.conbuildmat.2014.03.010.

Uzan, J., M. Livneh, and Y. Eshed. 1978. “Investigation of adhesion properties between asphaltic-concrete layers.” *Association of Asphalt Paving Technologists Proc*, 495–521. Lake Buena Vista, FL, USA.

Vanelstraete, A., and A. De Bondt. 2004. “Crack prevention and use of overlay systems.” *Prevention of Reflective Cracking in Pavements*, 53–67. CRC Press.

Vismara, S., A. A. A. Molenaar, M. Crispino, and M. R. Poot. 2012. “Toward a Better Understanding of Benefits of Geosynthetics Embedded in Asphalt Pavements.” *Transportation Research Record*, 2310 (1): 72–80. SAGE Publications Inc. https://doi.org/10.3141/2310-08.

Wargo, A. D. 2015. “Laboratory and field investigation of reflective crack mitigation in layered asphalt concrete pavements.” Ph.D Dissertation. Raleigh, NC, USA: North Carolina State University.

Wilkins, E. W. C. 1956. “Cumulative damage in fatigue.” *Colloquium on Fatigue / Colloque de Fatigue / Kolloquium über Ermüdungsfestigkeit*, 321–332. Springer, Berlin, Heidelberg. https://doi.org/10.1007/978-3-642-99854-6_35.

Wilson, B., A. Chowdhury, S. Hu, S.-S. Kim, M. Nazzal, and A. R. Abbas. 2017. *Tack Coat Performance and Materials Study*. Technical Report. College Station, TX, USA: Texas Transportation Institute, Texas A&M University System.

Witczak, M. A., M. W. Mamlouk, M. S. Kaloush, and K. E. Kaloush. 2007. “Validation Of Initial and Failure Stiffness Definitions in Flexure Fatigue Test for Hot Mix Asphalt.” *JTE*, 35 (1): 95–102. ASTM International. https://doi.org/10.1520/JTE100102.

Zhiming, T. 1997. “Mechanistic Analysis for Reflective Cracking in Asphalt Overlay.” *Journal of Tongji University Natural Science*, 25 (6).

Zhou, F., and L. Sun. 2000. "Mechanistic analysis of reflective cracking and validation of field test." *Fourth International RILEM Conference on Reflective Cracking in Pavements-Research in Practice*, 81–91. RILEM Publications SARL.

Zofka, A., M. Maliszewski, A. Bernier, R. Josen, A. Vaitkus, and R. Kleizienė. 2015. "Advanced shear tester for evaluation of asphalt concrete under constant normal stiffness conditions." *Road Materials and Pavement Design*, 16 (sup1): 187–210. Taylor & Francis. https://doi.org/10.1080/14680629.2015.1029690.

Appendix A. Literature Review

A.1. Reflective Cracking

Reflective cracking is the common distress after overlay placed over the old, cracked Portland cement concrete (PCC) or the hot mix asphalt (HMA) pavement. The existing crack on the underlaying old pavement causes the crack form at the bottom of the overlay and propagates through itself. Reflective cracking breaks the continuity of overlay and allows the water to enter the pavement. This will further reduce the soil-bearing capacity and deteriorate the entire pavement structure. Also, the prevalence of this distress would significantly influence the travel safety, driving comfortability, and service life of the pavement (Rigo et al. 2014). Figure A- 1 shows the mechanism of reflective cracking. The temperature variation and repeated traffic loading can induce the stress concentration adjacent to discontinuities tip in the existing pavement. The initial crack forms and propagates through the overlay due to the bending, shear, and thermal contraction effects (Lytton 1989).

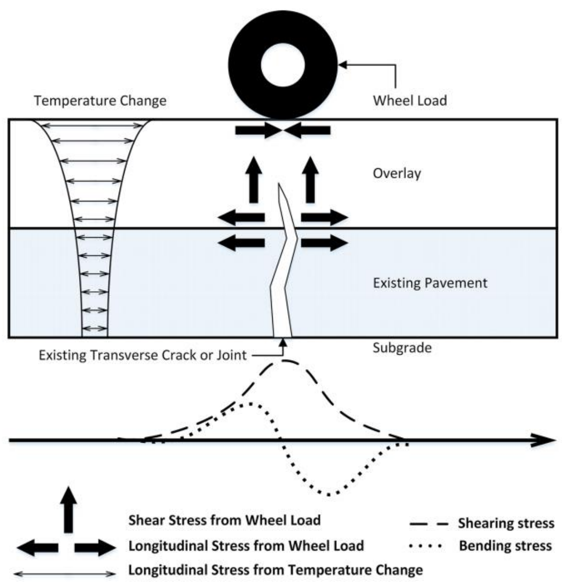

Figure A- 1. Mechanism of reflective cracking (Sudarsanan et al. 2015).

There are many ways to mitigate the reflective cracking, such as rubblization, milling, chip seal, sealing, increasing overlay thickness, and installing the stress absorbing membrane interlayer (SAMI) (Blankenship et al. 2004; Makowski et al. 2005; Zhiming 1997; Zhou and Sun 2000). Properly selected and constructed geosynthetic interlayer is one of the promising ways to effectively mitigate or control the reflective cracking (Baek 2010; Khodaei and Falah 2009; Mukhtar and Dempsey 1996).

A.2. Function of Geosynthetics

A.2.1 Reinforcing

Reinforcing function requires the geosynthetic products, such as paving fabric or paving grid, at the interface have significantly greater modulus (more than five times) than the asphalt mixture layer of which its embedded in (Lytton 1989). Sprague et al. (1998) also found the geosynthetic products with the stiffness greater than 200 kN/m at a strain between 2% to 5% develop sufficient reinforcement to overlay. When the reflective cracking reaches the reinforced-interlayer, the original perpendicular crack propagation will transfer to horizontal direction and travel below the reinforced-interlayer. The properly installed reinforcing-geosynthetic interlayer can indefinitely delay the prevalence of the reflective cracking (Button and Lytton 1987). The sufficient overlay thickness is also required to achieve the reinforcing function. The common thickness, recommended by the geosynthetic manufacture, to install geosynthetic interlayer is at least 3.81 cm (1.5 in) (Huesker 2015; Tencate 2019).

A.2.2 Stress Relieving

Common stress-relieving geosynthetic has lower stiffness and stalls the reflective cracking at interlayer, though crack could still form at the top of the interlayer system and propagate through the overlay. The stress-relieving geosynthetic can store strain at low stress level and mitigate the reflective cracking (Joel Sprague et al. 1998; Lytton 1989).

A.2.3 Water Barrier

While the crack penetrates through the overlay, the geosynthetic products act as a barrier to prevent water infiltration and protect the underlying structure (Lytton 1989). The fully impregnated geosynthetic can significantly reduce the water permeability. However, extra care should be taken when compacting the overlay; the permeable overlay would allow more water to trap at the reinforced layer. This will cause the rapid failure of overlay because of moisture damage (Bognacki et al. 2007).

A.3. Debonding Problem

The interlayer bonding between the asphalt surface and the underlying course is significantly influencing asphalt pavement performance (Khweir and Fordyce 2003; Kruntcheva Mariana R. et al. 2005; Sudarsanan et al. 2016). Different pavement layers act as a monolithic structure that efficiently transfer stress and strain caused by temperature change and repeated traffic loading. This requires adequate interlayer bonding. However, insufficient interlayer bonding leads to stress concentration and may result in debonding (Su et al. 2008). Debonding causes the slippage or delamination of the surface course; the premature distress significantly decreases the service life of the pavement (Hachiya et al. 1997; Peattie 1980; Sutanto 2009). Stress at interlayer caused by the moving traffic is shown in Figure A- 2. Raab and Partl (2004) found the tension mode, shear mode, or a mix of tension and shear mode phenomenon in fracture mechanic could characterize the debonding.

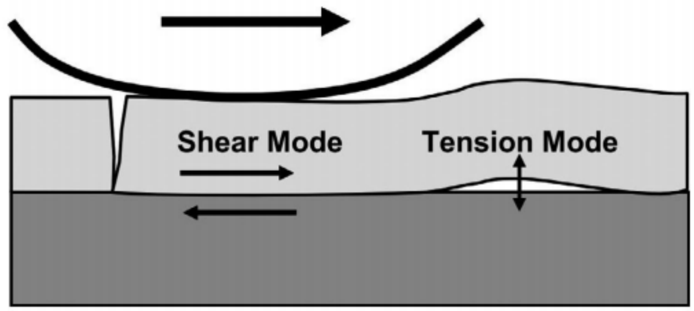

Figure A- 2. Stress at interlayer caused by moving traffic (Raab and Partl 2004).

A.4. Factors Influencing the Bonding

A.4.1 Tack Coat Type

Asphalt emulsion is widely used in tack coat application in the field. Base on the emulsion curing time, it can be categorized into rapid setting (e.g., CRS-2), medium setting, and slow setting (e.g., SS-1, CSS-1) conditions. Based on the survey conducted by Mohammad et al. (2012), slow-setting emulsions are widely used in the world due to its easy to spray and low cost. The selection of the asphalt emulsion type highly depends on the construction window, traffic condition, and environment temperature. If it fails to meet the construction conditions, the interlayer bonding strength cannot be guaranteed. Thereby, leading to premature distress happens in the asphalt pavement. Asphalt emulsions are not commonly used in the geosynthetic-reinforced interlayer installation. Button and Lytton (2007) claimed the most emulsions have less viscosity compared with asphalt binder, which may not provide enough bonding. Also, geosynthetic-reinforced interlayer requires high application rate for emulsions depends on its binder content. However, this will increase the curing time and difficulty in construction.

Asphalt binder is one of tack coat material that could generate higher interlayer bond strength compared with the most asphalt emulsion. The application of the asphalt binder does not require curing time, thereby asphalt binder is recommended to use in geosynthetic-reinforced interlayer construction (Button and Lytton 2007). However, due to high viscosity compared with the asphalt emulsion, it requires to heat binder to a high temperature to spray evenly.

Cutback asphalt should not be used for the polymeric type of geosynthetic because the solvent will remain in the geosynthetic layer and further deteriorate the polymer (Button and Lytton 2007).

A.4.2 Tack Coat Application Rate

Tack coat application rate impacts the interlayer bonding performance. Excessive or lack of tack coat induces premature distress in the pavement. However, the current researchers have the debate over whether there is an optimum tack coat application rate (Al-Qadi et al. 2008; Bae et al. 2010; Mohammad et al. 2002; Raposeiras et al. 2013). Table A- 1 and Table A- 2 list the NCHRP report 712 and FHWA Tech Brief recommended tack coat application rate for different surface conditions, respectively (Mohammad et al. 2012).

Table A- 1. NCHRP Report 712 Tack Coat Application Rate (Mohammad et al. 2012).

Surface type	Residual application rate (gal/yd^2)
New asphalt mixture	0.035
Old asphalt mixture	0.055
Milled asphalt mixture	0.055
PCC	0.045

Table A- 2. FHWA Tech Brief Tack Coat Application Rate (FHWA 2016).

Surface type	Residual application rate (gal/yd^2)
New asphalt mixture	0.02-0.05
Old asphalt mixture	0.04-0.07
Milled asphalt mixture	0.04-0.08
PCC	0.03-0.05

The asphalt retention rate of geosynthetic material should be taken into consideration when applying tack coat for the geosynthetic-reinforced interlayer. Amini (2005) suggested the practice tack coat application rate for geosynthetic is tack coat application rate for particular pavement surface type plus asphalt retention rate. However, excessive tack coat application may cause difficulty during geosynthetic installation (Button and Lytton 2007).

A.4.3 Curing Time

There is a discrepancy in the effect of the curing time. WDOT found the curing time is not a significant factor in influencing shear strength (Tashman et al. 2006). However, it is commonly reported in the field that the uncured asphalt emulsion was lifted by the wheels of a haul truck, which failed to achieve the design tack coat application rate in the field. Trackless tack coat solves the problem of tracking. The setting time for trackless tack is from 5 to 15 min and a good bond strength can be provided (Bae et al. 2010; Mohammad et al. 2011).

A.4.4 Surface Texture

Wilson et al. (2017) found a higher interlayer bond strength for milled pavement; however, in their recent research, the milled specimens cored from the field did not show shear strength difference with the unmilled specimens. They claimed this phenomenon might occur due to the moisture damage to the milled specimens. WDOT extracted the field core from both the unmilled and milled surface and found the milled surfaced texture provided a better shear resistance ability (Tashman et al. 2006).

A.5. Test Methods

Various assessment methods in the field or laboratory shed light on interface shear properties. For laboratory assessment conditions, various tests can be performed on field-core or laboratory-prepared specimens. It should be noted that the laboratory test can accurately control the experiment setting and obtain better repeatability and reproducibility.

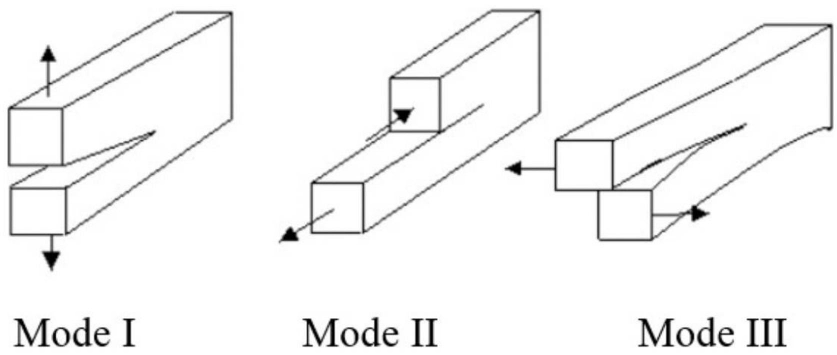

Figure A- 3. Fracture mechanics crack mode

Typically, using fracture mechanics interlayer bonding assessment tests are categorized as Mode I tension opening test, Mode II in-plane shear test, and Mode III out-of-plane shear test (Collop et al. 2011), as shown in Figure A- 3. The tests cover a wide range of methods and conditions to capture interface shear properties. Different test protocols correspond to various test equipment. Due to the multiple factors contributing to interface shear properties, the selection of the test method is closely related to the mode of loading, failure mode, and experiment accuracy. Mode II in-plane shear test mode is commonly used to characterize interface shear properties because it could test easily and highly mimic the in-situ condition, which is helpful to understand the mechanism of interface shear properties. In the Mode II in-plane shear test, it can further divide into a direct shear test and simple shear test. The interface shear property is controlled by various factors such as test temperatures, loading rates, material types, tack coat application rates, and interaction among those factors (Boulangé and Sterczynskia 2012).

The prototype of the pavement interface shear test was established on the soil mechanics principle, Leutner shear test was developed in Germany, and its counterpart was built in the U.S. by Uzan (1978). Mode II in the plane shear mode test can categorize into guillotine type direct shear test or shear box type simple shear test. Figure A- 4 shows the stress distribution for the direct shear test and simple shear test. It should note that the direct shear tests have significant shear stress concentration and the simple shear tests have a parabolic shear stress distribution.

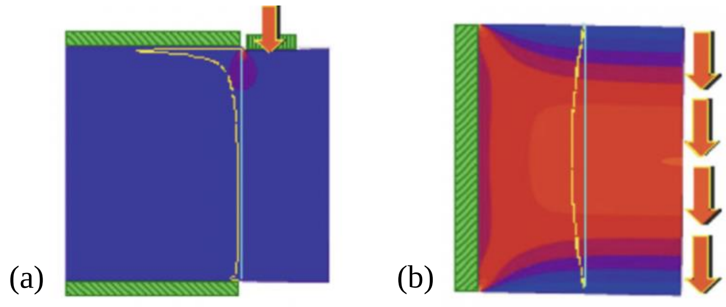

Figure A- 4. Shear stress distribution (a) Direct Shear Test; (b) Simple Shear Test (Raab et al. 2009).

Generally, the direct shear test lacks the confining pressure apparatus, in order to arrest precise interface shear properties normal stress plays a critical role in dictating the interface asphalt mixture interlock and friction behavior. Therefore, some research institutes use an extra load cell or an actuator to induce normal stress. The shear test devices usually are installed in the servo-hydraulic loading system (e.g., Material Testing System/MTS), which controls the mode of loading, with an extra environment chamber to maintain the testing temperature. The typical laboratory-prepared specimen is a double-layer cylindrical or cubical shape. In order to solve the interface alignment issue, a gap is introduced between the shear device's shearing ring.

A.5.1 Ancona Shear Testing Research and Analysis (ASTRA) Device

The Ancona Shear Testing Research and Analysis (ASTRA) Device was developed in Italy in 2005 by Universita Politecnica delle Marche in Ancona, as shown in Figure A- 5. ASTRA is a simple shear tester and can perform shear tests on double-layer specimens. This shear box bears the cylindrical specimen with a 95 mm diameter. During the test, a constant vertical normal load is maintained on the specimen. Also, a linear variable displacement transducer (LVDT) is used in the ASTRA system to record the specimen deformation. The measuring system of the ASTRA records the interface shear stress and vertical direction displacement. Conducting ASTRA test at different deformation rates and temperatures can obtain the adhesion and friction parameters for constructing the Mohr-Coulomb type envelope (Pasquini et al. 2015).

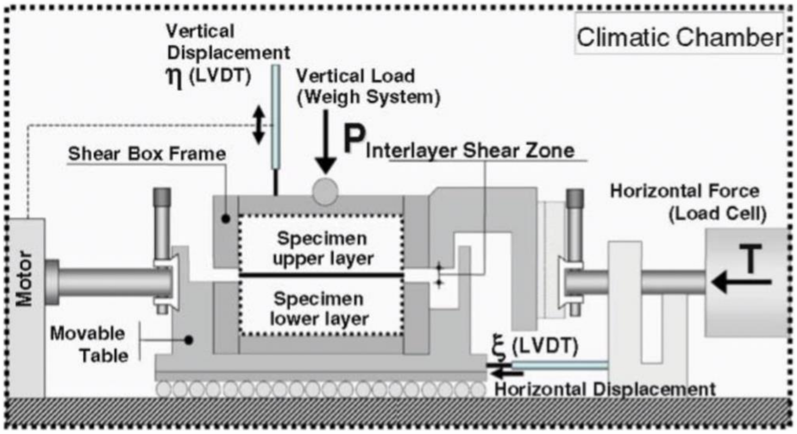

Figure A- 5. Ancona Shear Testing Research and Analysis (ASTRA) device (Pasquini et al. 2015).

A.5.2 Louisiana Interlayer Shear Strength Tester (LISST)

Louisiana interlayer shear strength tester is developed by Louisiana state university, as shown in Figure A- 6. The test could perform on 100 mm or 150 mm diameter double-layer specimens. The tester is composed of a shearing frame and reaction frame; during the test, the shearing frame is connected to the loading system while the reaction frame remains stationary. This test controls the displacement rate of 2.54 mm/min and test temperature of 25 ± 1°C, the normal confining pressure is capable of applying up to 206.84 kPa (30 psi) (Mohammad et al. 2018).

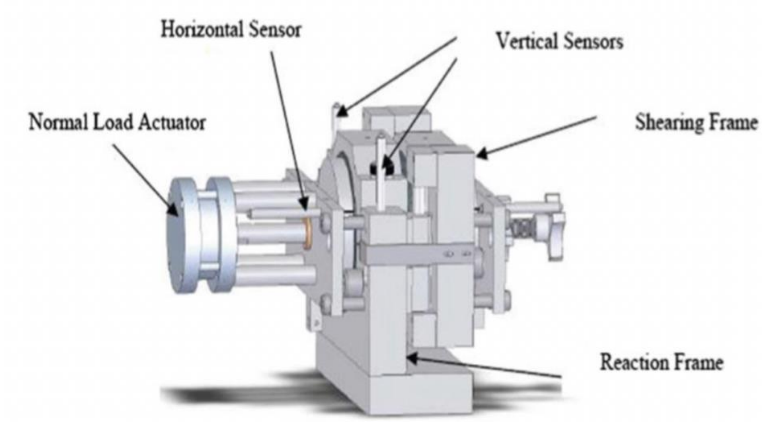

Figure A- 6. Louisiana interlayer shear strength tester (LISST) (Mohammad et al. 2018).

A.5.3 Sapienza Direct Shear Testing Machine (SDSTM)

Sapienza Direct Shear Testing Machine is developed by the research team in Sapienza University of Roma (Tozzo et al. 2014), as shown in Figure A- 7. The tests perform on 100 mm diameter double-layer specimen. The gap between the two molds is 10 mm. This test controls the load with the frequency of 5 Hz and the testing temperature is 21 ± 1°C. The study found normal pressure plays an important role in interface fatigue property. The monotonic shear tests have the same trend on the influence of the normal pressure with the cyclic fatigue shear test.

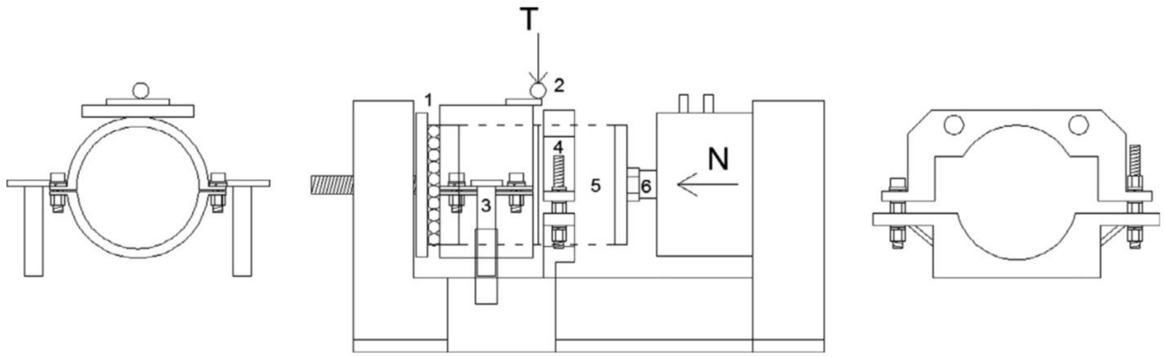

Figure A- 7. Sapienza Direct Shear Testing Machine (SDSTM) (Tozzo et al. 2014).

A.5.4 Advanced Shear Tester (AST)

The advance shear tester (AST) was designed in 2015 by Zofka et al. (2015), as shown in Figure A- 8. The shear test devices could be installed in a servo-hydraulic loading system with an extra environment chamber. The AST laboratory-prepared specimen is a double-layer 150 mm diameter cylindrical shape.

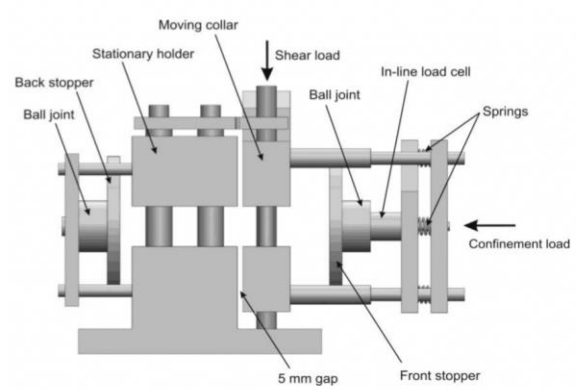

Figure A- 8. Advanced Shear Tester (AST) (Zofka et al. 2015).

Zofka stated that the boundary condition for the shear test can be divided into the constant normal load, constant normal stiffness, and constant volume. Though the constant normal load condition is used by most of the shear devices, he proposed the constant normal stiffness condition has its edge. Constant normal stiffness condition mimics the low-speed heavy track on the thin layer condition. Also, the dilation property at interlayer cannot be comprehensively explained by constant normal load condition. Therefore, constant normal stiffness could be a suitable candidate for constant normal load condition to use in the shear device. Also, using a constant normal load should install a vertical actuator to maintain the load. However, the constant normal stiffness shear device uses die springs to maintain the confining pressure, which largely decreases the cost of the device.

A.5.5 Modified Asphalt Shear Tester (MAST)

The North Carolina State University (NCSU) research team developed the modified asphalt shear tester (MAST) shown in Figure A- 9 by modifying AST (Cho 2016). MAST is capable of conducting the shear tests in both monotonic and fatigue modes of loading under confining pressure. The cylindrical specimen with a diameter of 101.6 mm (4 in.) extracted from a 152.4 mm (6 in.) gyratory samples or square-shape specimen with widths of 152.4 mm (6 in.) and 101.6 mm (4 in.) trimmed from a slab sample can be used for the MAST shear tests, whereas AST allows to use only cylindrical gyratory specimens of 150 mm (6 in.) in diameter. It is a well-known fact that air void gradient exists along the periphery of gyratory specimens (Chehab et al. 2000), thereby using a 101.6 mm (4 in.) specimen cored from a 150 mm (6 in.) gyratory sample in MAST nullifies the uncertainties of air void effect on the test outcomes.

The initial confining pressure is controlled by the in-line load cell through tightening the bolts on the side panel. The technique employed to apply confining pressure remains same for both AST and MAST devices. However, approaches of fastening the specimens to both machines vary vastly. AST allows the user to tie the specimen directly to the device’s upper and lower jaw of the moving and stationary collar by tightening the threaded bolt and nut arrangement. The specimens during shear testing typically expand due to the aggregate rearrangement along the interface. Thereby, the frictional forces between the collar walls and the specimen could not hold the specimen in place that leads to slippage. This influences the shear and the confining load cell readings during the test. MAST test device addresses this issue by gluing the specimen firmly to a four-set shoe arrangement. The shoe is fastened to a stationary portion of the jig that is free to move horizontally (along the confining pressure load cell) with the aid of linear tracks. Thus, MAST device allows the free expansion of specimen during testing without any slippage along the walls of the shoe. Figure A- 10 shows the typical confining pressure during a MAST monotonic shear test. The confining pressure recorded from the in-line load cell varies from initial stress by 5% and stabilizes after reaching peak shear. The gap between the fixed and movable side platens is 8 mm. Even though the specimen is fastened using shoes to the jig firmly, the large bending moment generated during the test causes rocking motion to the shoe. MAST device has the provision to monitor the on-specimen displacements during such events with the aid of non-contact digital image correlation (DIC) technique. MAST is designed to have the opening on one side, which allows the DIC system to track on-specimen displacement. All the aforementioned factors make MAST a superior device over AST.

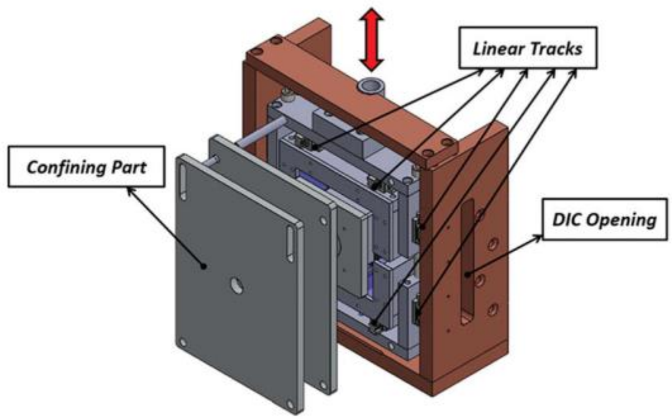

Figure A- 9. Modified asphalt shear tester (MAST) (Cho et al. 2017b).

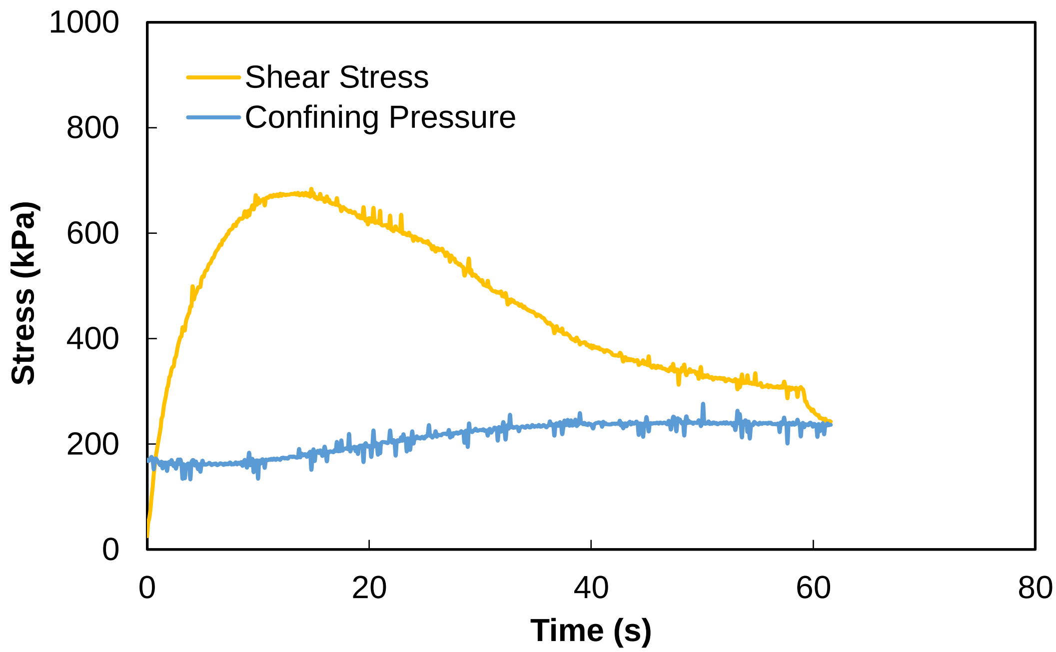

Figure A- 10. Typical MAST test result.

Cho and Kim (2016) verified the time-temperature superposition principle on shear failure of double-layered asphalt concrete specimens with different tack coats and GlasGrid interlayer. A shear strength prediction model was proposed to predict shear strength at various confining pressures, temperatures, and shear strain rates. Furthermore, FlexPAVE™ analysis was conducted to determine the potential debonding state. Shear ratio (SR), as shown in Figure A-11, was calculated by the ratio of the FlexPAVE™ computed shear stress to the model predicted shear bond strength. The maximum shear ratio was presented as an index parameter to determine the pavement debonding potential (Cho et al. 2017a).

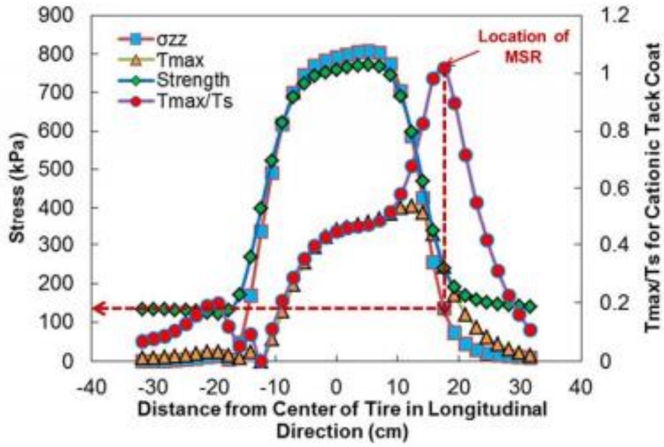

Figure A- 11. Shear ratio concept.

A.6. Bonding of Geosynthetic-Reinforced Interlayer

Baek (2010) found the interface shear bond strength is a good indicator to reflect the potential of reflective cracking. The lower interface bond strength could increase the possibility of developing reflective cracking. The geosynthetic reinforcement at the interlayer could decrease the interlayer bonding (Canestrari et al. 2016; Pasquini et al. 2013). The Adequate bonding in geosynthetic-reinforced interlayer sufficiently distributes the stress and guarantees the functionality of geosynthetic-reinforced interlayer. The improper installation of the geosynthetic could not stall or mitigate the reflective cracking propagation, which will influence the durability of the pavement (Ferrotti et al. 2012; Vanelstraete and De Bondt 2004).

Canestrari et al. (2006) used ASTRA to conduct the shear test on two types of glass geogrids (GG), polyester geogrid (PG), and geomembrane (GM) reinforced specimens. The reinforced the double-layer system controlled top layer as dense graded mix; the bottom layer was either dense graded mix or open grade mix. The result shows a higher mesh dimension (25×25 mm^2) of the paving grid has better shear resistance ability than lower mesh dimension product (12.5×12.5 mm^2). With the decrease of the mesh size, the residual friction angle from the friction envelope also reduces. The research shows the bottom layer surface condition does not have an impact on the shear strength of GM reinforced specimens. In another paper, Canestrari et al. (2016) found geosynthetic with a higher thickness could significantly decrease the interlayer shear strength.

Vismara et al. (2012) conducted monotonic shear tests to investigate the performance of the geosynthetic-reinforced interlayer. Polypropylene nonwoven and fiberglass grid composite reinforced slab specimens were subjected to the Leutner shear tester at 5°C and 25°C with a constant deformation rate at 0.85 mm/s (2 in./min). An average 70% reduction in shear strength compared with the control specimen is found in geosynthetic-reinforced specimens.

Ferrotti et al. (2011) performed the monotonic shear test on both paving grid reinforced and unreinforced specimens at 20°C. During the tests three confining pressures (0, 0.2 and 0.4 MPa) were selected at the constant displacement rate of 2.5 mm/min (0.1 in./min). The shear strength and friction envelopes were obtained by the shear tests. Under unconfinement conditions, the shear strength decreases with the presence of the paving grid, however with the increase of the confining pressure, the trend reverses. Between grid reinforced specimen, the polymer-modified emulsion specimens show a higher shear resistance performance than conventional emulsion type under all three confining pressures. He found a similar residual friction angle for both grid reinforced and unreinforced specimens. He reported due to the poor interlayer bonding, one condition of slab compactor compacted double-layer specimen separated during the specimen coring process, this type of the specimen did not apply any tack coat. The author claimed this problem was contributing to the poor quality when asphalt loose mix fabricated in mix plant. Also, the same reason explained the unreinforced specimen shows higher variability in monotonic shear tests.

Sudarsanan et al. (2018a) using Leutner shear tester to conduct the shear test on three different (Jute, Coir, and Synthetic GlasGrid) geosynthetic materials. He found with the presence of the geosynthetic the interlayer shear strength has a certain reduction. The reduction is in conjunction with the tensile modulus of corresponding geosynthetic products, the geosynthetic with higher modulus results in experiencing less shear strength reduction. The shear tests are reported to have more variability at lower temperatures and high deformation rates. When the temperature increases from 10°C to 30°C the shear strength decreases by nearly 80%.

A.7. Critical Summary

There are many ways to mitigate the reflective cracking, such as rubblization, milling, chip seal, sealing, increasing overlay thickness, and installing stress absorbing membrane interlayer (SAMI). Geosynthetic interlayer is one of the promising ways to effectively mitigate or control the reflective cracking.

The primary functions of the geosynthetic are reinforcing, stress-relieving, and waterproofing. The reinforcing function requires the geosynthetic material to have significantly greater modulus than the surrounded asphalt layer. It could redirect crack propagation at interlayer, which can indefinitely delay or mitigate reflective cracking. Stress-relieving geosynthetic products have lower stiffness and can store strain at low stress level. The fully impregnated geosynthetic could significantly reduce the water permeability. The proper installation, controlling overlay thickness, and overseeing compaction quality are also required to achieve the functions of geosynthetic.

Tack coat is required to use in geosynthetic-reinforced interlayer construction. Cutback asphalt should not be used for the polymeric type of geosynthetic because the solvent will remain in the geosynthetic layer and further deteriorate the polymer. Geosynthetic-reinforced interlayer requires high application rate for emulsions depends on its binder content. However, this will increase the curing time and difficulty in construction. The application of the asphalt binder does not require curing time and application rate is satisfied for the construction requirement. Thereby, asphalt binder is recommended to use in the geosynthetic-reinforced interlayer. Some researchers suggest the practice tack coat application rate for geosynthetic is tack coat application rate for a pavement surface type plus asphalt retention rate. However, excessive tack coat application may cause difficulty during geosynthetic installation.

The direct shear test is helpful in understanding the mechanism of interface shear properties. The geosynthetic material installing at the interlayer decreases the interlayer shear bonding. The improper installation of the geosynthetic could not stall or mitigate the reflective cracking propagation. The lower interface bond strength could increase the possibility of developing reflective cracking. Geosynthetic with a higher thickness significantly decreases the interlayer shear strength.

Appendix B. Beam Bending Theory and Four-Point Beam Bending Stress/Strain

Classical beam bending theory is an essential consideration for nearly all structural designs and analyses. To evaluate the bending stress or strain in a four-point bending beam test, consider a small element cut from the middle one-third of the beam, as shown in Figure B- 1 (a). Due to the bending action, the element will be deformed, as shown in Figure B- 1 (b). The amount by which a layer increases or decreases in length depends upon the position of the layer with respect to the neutral axis (N-N). The layers above the N-N axis will reduce the layer length when subjected to compressive stress whereas the layer length will increase for layers below the N-N axis under tensile stress. This theory of bending is known as the theory of simple bending.

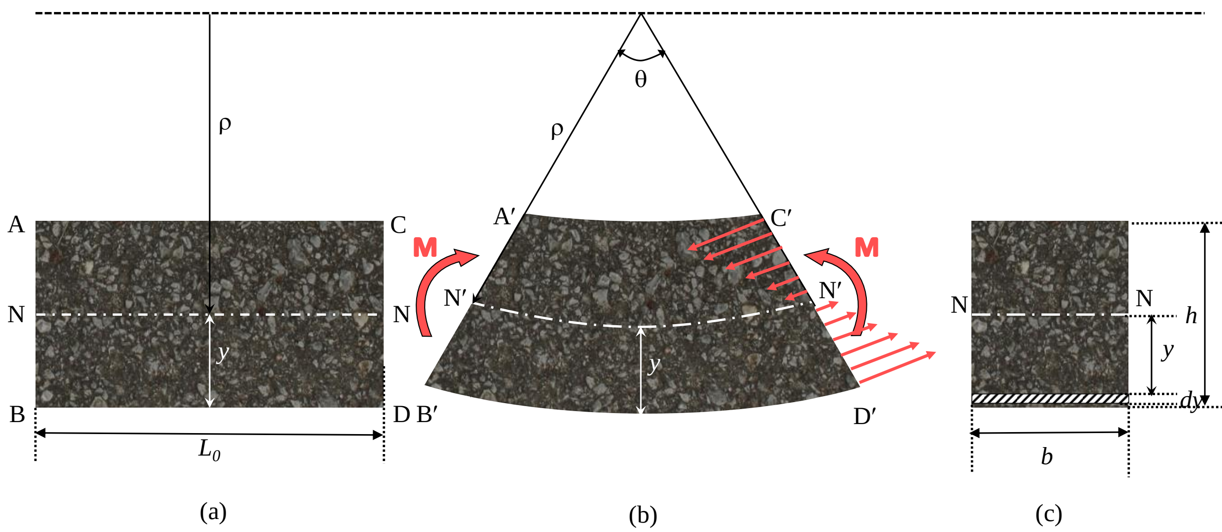

Figure B- 1. Beam bending of a small element: (a) before bending, (b) after bending, and (c) sectional view.

B.1. Bending strain

The arc length, L, is related to the radius of the curvature, ρ, through $L = \rho\theta$, where θ is the bending angle. In Figure B- 1, an object of initial length L_0 is bent as shown. Because the object has a finite thickness, different portions of it are stretched or compressed by different degrees. The outer portion of the beam is extended the most because it is farthest from the center. Mathematically, all portions are bent to the same angle, θ, but ρ varies throughout the thickness. Thus, the quantity $\rho\theta$ varies too, and therefore, L varies as well.

The next step is to avoid the confusion of having different radii of curvatures through the thickness of the bent object. This step is accomplished in two steps. First, find the one ρ that satisfies $\rho\theta = L_0$. Note that ρ is the computed result here, and θ and L_0 are the inputs. Note also that the length in the equation is L_0, which is the original undeformed length, not the deformed length. This step establishes one unique value of ρ for the cross-section rather than multiple values that could lead to much confusion. The second step is to introduce the variable y as the distance from the neutral axis to any other radius in the cross-section. Here, we consider the strain in the farthest layer, i.e., the tensile strain at the bottom of the beam.

The basic definition of normal strain is shown in Equation (10-1).

$$\varepsilon = \frac{\Delta L}{L} \tag{10-1}$$

Using the line segment, *BD*, the before bending [Figure B- 1 (a)] length and the after bending [Figure B- 1 (b)] length, $B'D'$, are used to measure the tensile strain, as shown in Equation (10-2).

$$\varepsilon = \frac{\overline{B'D'} - \overline{BD}}{\overline{BD}} \tag{10-2}$$

The line length *BD* is the same for all locations in the same element before bending. However, $B'D'$ lengthens as it is below the neutral axis for positive moment. The lines *BD* and $B'D'$ can be described using the radius of curvature ρ, and the bending angle θ, as shown in Equations (10-3) and (10-4), respectively.

$$\overline{BD} = \rho\theta \tag{10-3}$$

$$\overline{B'D'} = (\rho + y)\theta \tag{10-4}$$

Substituting Equations (10-3) and (10-4) into Equation (10-2) yields Equation (10-5).

$$\varepsilon = \frac{(\rho + y)\theta - \rho\theta}{\rho\theta} \Rightarrow \varepsilon = \frac{y}{\rho} \tag{10-5}$$

Equation (10-5) is a key result of the strain in the beam. It shows that the strain is zero at $y = 0$, the neutral axis, and varies linearly from it. If the object is thick, then *y* can take on large values, but for thin objects, it cannot. This phenomenon is the fundamental reason that thick objects have more bending stiffness (resistance to bending) than thin objects.

Also, the radius of the curvature in the denominator accounts for many effects of bending. When the object is not bent, then ρ is infinite and the strains are naturally zero. As the object bends, ρ decreases, and the equation shows that the strain values will increase.

Finally, note that the strain is normal strain and is, in fact, longitudinal along the length of the beam. It is common to align the *x*-axis along the beam's length, defining the strain, ϵ_x, as shown in Equation (10-6).

$$\varepsilon_x = \frac{y}{\rho} \tag{10-6}$$

B.2. Bending stress

Applying Hooke's Law, $\sigma_x = E \times \epsilon_x$, in Equation (10-6) to obtain stress, σ_x, yields Equation (10-7).

$$\sigma_x = \frac{Ey}{\rho} \tag{10-7}$$

Hooke's Law also states that each normal stress component is dependent on all three normal strain components. But here, the strain is multiplied by E to obtain the stress, assuming that no lateral loads/stresses are acting on the beam (like in uniaxial tension). This phenomenon occurs in most beams because they are thin relative to their length.

Measuring the radius of curvature is difficult and, hence, establishing a relationship with the bending moment would facilitate the measurements. Bending induces stress in the beam layers, thereby generating both compressive and tensile forces. These forces will have a moment about the neutral axis. The total moment of these forces about the neutral axis for a section is known as the moment of resistance of that section. Consider a cross-section of a beam, as shown in Figure B- 1 (c), where the thin layer at the bottom of the section has an area dA at distance y, as described by Equation (10-8).

$$\text{Force on layer} = \frac{E}{\rho} \times y \times dA \tag{10-8}$$

Moment of this force about the neutral axis

$$\begin{aligned} &= \text{Force on layer} \times \text{y} \\ &= \frac{E}{\rho} \times y \times dA \times y \\ &= \frac{E}{\rho} \times y^2 \times dA \end{aligned}$$

The total moment of the forces on the section of the beam (or moment of resistance):

$$\therefore M = \int \frac{E}{\rho} \times y^2 \times dA = \frac{E}{\rho} \int y^2 \times dA$$

Note that the integral is the area moment of inertia, I_{zz}, or the second moment of the area.

$$\because I_{zz} = \int y^2 \times dA$$

Using the area moment of inertia gives Equation (10-9).

$$M_z = \frac{EI_{zz}}{\rho} \tag{10-9}$$

Substituting Equation (10-9) into Equation (10-7) gives Equation (10-10).

$$\sigma_x = \frac{M_z y}{I_{zz}} \tag{10-10}$$

Equation (10-10) gives the normal bending stress and is commonly called the flexure formula.

All these relationships, i.e., Equations (10-7) through (10-10), lead to the Euler-Bernoulli bending equation, shown here as Equation (10-11).

$$\frac{M}{I} = \frac{\sigma}{y} = \frac{E}{\rho} \tag{10-11}$$

The fatigue test involves the application of load or displacement in both the compression and tension direction. Consider compression loading in a four-point bending beam test with a deflection δ (negative for compression) generated by a load application of P, as shown in Figure B-2.

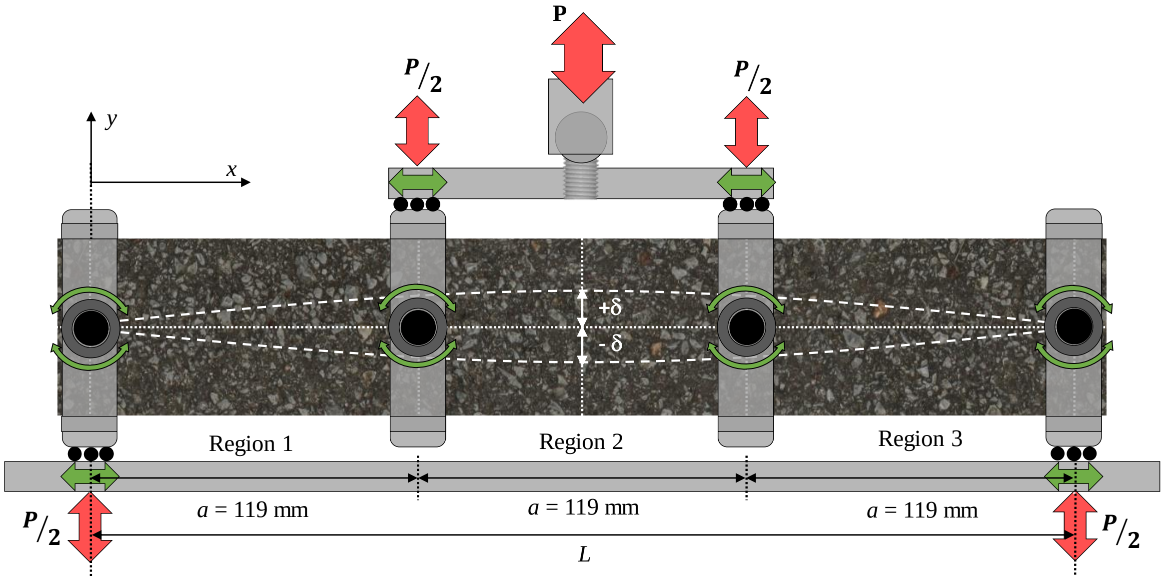

(a)

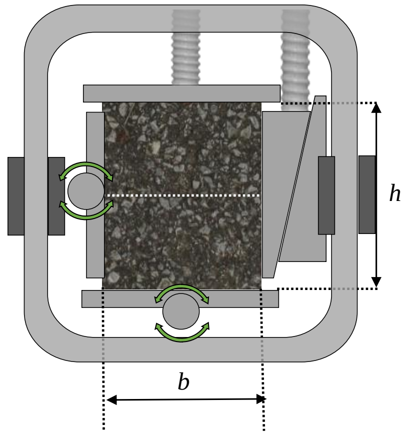

(b)

Figure B- 2. Four-pont bending beam fatigue test configuration: (a) front view and (b) sectional view.

From Equation (10-10), two factors, I_{zz} and M, should be represented in known terms, i.e., specimen dimensions and applied loads for the easy evaluation of tensile stress.

A rectangular cross-section of height h and width b has a moment of inertia shown in Equation (10-12).

$$I_{zz} = \frac{bh^3}{12} \tag{10-12}$$

The maximum moment is at the center of the beam, i.e., @ $x = L/2$, and is derived as Equation (10-13).

$$\begin{aligned} M_{z-\max} &= \frac{-P}{2}x + \frac{P}{2}(x-a) \\ \Rightarrow M_{z-\max} &= \frac{Pa}{2} \end{aligned} \tag{10-13}$$

Substituting Equations (10-12) and (10-13) into Equation (10-10) to calculate the maximum tensile stress at the extreme depths of beam sections gives Equation (10-14).

$$\sigma_{x-\max} = \frac{M_{z-\max}\, y_{bottom}}{I_{zz}} = \frac{{}^{Pa}\!/_{2} \times {}^{h}\!/_{2}}{{}^{bh^3}\!/_{12}}$$

$$\sigma_{x-\max} \text{ or } \sigma_t = \frac{3aP}{bh^2} \tag{10-14}$$

In order to derive the tensile strain at the bottom of the beam, the differential equations for the prismatic beams that establish the bending moment relationship, known as the bending moment equation, are as follows, i.e., Equations (10-15) through (10-31).

$$EI\frac{d^2y}{dx^2} = M \tag{10-15}$$

Region 1: x < a

$$M_1 = \frac{-Px}{2} \tag{10-16}$$

Substitute Equation (10-16) into Equation (10-15):

$$EI\frac{d^2y}{dx^2} = \frac{-Px}{2} \tag{10-17}$$

Integrate both sides of Equation (10-17):

$$EI\frac{dy}{dx} = \frac{-Px^2}{4} + C_1 \tag{10-18}$$

$$EI\theta_1 = \frac{-Px^2}{4} + C_1$$

$$\theta_1 = \frac{-Px^2}{4EI} + C_1 \tag{10-19}$$

Integrate both sides of Equation (10-18):

$$EI\delta_1 = \frac{-Px^3}{12} + C_1x + C_2$$

$$\delta_1 = \frac{-Px^3}{12EI} + C_1x + C_2 \tag{10-20}$$

Region 2: a < x < 2a

$$M_2 = \frac{-Px}{2} + \frac{-P(x-a)}{2} \Rightarrow M_2 = \frac{-Pa}{2} \tag{10-21}$$

Substitute Equation (10-21) into Equation (10-15):

$$EI\frac{d^2y}{dx^2} = \frac{-Pa}{2} \tag{10-22}$$

Integrate both sides of Equation (10-22):

$$EI\theta_2 = \frac{-Pax}{2} + C_3$$

$$\theta_2 = \frac{-Pax}{2EI} + C_3 \tag{10-23}$$

Integrate both sides of Equation (10-23):

$$\delta_2 = \frac{-Pax^2}{4EI} + C_3x + C_4 \tag{10-24}$$

Boundary conditions

BC1	@x=0	δ_1=0	BC3	@x=a	δ_1=δ_2
BC2	@x=L/2	θ_2=0	BC4	@x=a	θ_1=θ_2

Applying the boundary conditions at different regions:

BC2 on Region 2, BC2: @x = L/2, θ_2 = 0 in Equation (10-23).

$$C_3 = \frac{PaL}{4EI} \tag{10-25}$$

BC4 in region 1 and 2, BC4: @x = a, θ_1 = θ_2, Equation (10-19) = Equation (10-23).

$$\frac{-Px^2}{4EI} + C_1 = \frac{-Pax}{2EI} + C_3 \Rightarrow \frac{-Px^2}{4EI} + C_1 = \frac{-Pax}{2EI} + \frac{PaL}{4EI}$$

$$\therefore C_1 = \frac{Pa}{4EI}(L-a) \tag{10-26}$$

BC1 in Region 1, BC1: @x = 0, δ_1 = 0 in Equation (10-20).

If δ_1 = 0, then C_2 should be zero:

$$\therefore C_2 = 0 \tag{10-27}$$

BC3 in Region 2, BC3: @x = a, δ_1 = δ_2, Equation (10-20) = Equation (10-24), substituting C_1, C_2, and C_3.

$$\frac{-Pax^2}{4EI}+\frac{PaL}{4EI}x+C_4=\frac{-Px^3}{12EI}+\frac{Pa}{4EI}(L-a)x$$

$$C_4=\frac{-Pa^3}{12EI} \tag{10-28}$$

After solving for all the constants, find the maximum tensile strain by finding the maximum deflection and moment @x = L/2 in Equation (10-24).

$$\delta_2=\frac{-Pax^2}{4EI}+\frac{PaL}{4EI}x-\frac{Pa^3}{12EI}\Rightarrow\frac{Pa}{48EI}(3L^2-4a^2) \tag{10-29}$$

Consider Equation (10-10) and apply Hooke's law.

$$\varepsilon_{x-\max}=\frac{M_{\max}y_{bottom}}{EI_{zz}}$$

$$\text{where } M_{\max}=\frac{Pa}{2}, y=\frac{h}{2}$$

$$\therefore \varepsilon_{x-\max}=\frac{Pah}{4EI} \tag{10-30}$$

$$\delta_2=\frac{Pa}{48EI}(3L^2-4a^2)=\frac{\varepsilon_{x-\max}}{12h}(3L^2-4a^2)$$

$$\varepsilon_{x-\max}\text{ or }\varepsilon_t=\frac{12\delta h}{(3L^2-4a^2)} \tag{10-31}$$

The maximum tensile stress (MPa) and maximum tensile strain in four-point bending beam fatigue tests were calculated using Equation (10-14) and Equation (10-31), respectively (ASTM D7460).

Appendix C. Sinusoidal Fitting Procedure

The procedure for analyzing the tensile strain utilizes a least-squares regression technique that first assumes that the stress and strain are represented by the functional form presented in Equation (11-1).

$$y(t) = A_0 + C_1 \cos(2\pi ft + \theta) \tag{11-1}$$

If the addition law for cosines is applied to Equation (11-1), then the function may be written as Equation (11-2).

$$y(t) = A_0 + A_1 \cos(2\pi ft) + B_1 \sin(2\pi ft) \tag{11-2}$$

where A_1 and B_1 are given by Equations (11-3) and (11-4), respectively.

$$A_1 = C_1 \cos(\theta) \tag{11-3}$$

$$B_1 = -C_1 \sin(\theta) \tag{11-4}$$

The angle, theta, can be calculated through Equations (11-3) and (11-4) as Equation (11-5).

$$\theta = \tan^{-1}\left(\frac{-B_1}{A_1}\right) \tag{11-5}$$

Note that, if θ is larger than π, then A_1 will be less than one, but from Equation (11-5), θ will be calculated as less than π. Therefore, presenting Equation (11-5) in a piecewise form, as shown in Equation (11-6), provides more accuracy.

$$\theta = \begin{Bmatrix} \tan^{-1}\left(\frac{-B_1}{A_1}\right), A_1 > 0 \\ \tan^{-1}\left(\frac{-B_1}{A_1}\right) + \pi, A_1 < 0 \end{Bmatrix} \tag{11-6}$$

The amplitude of the function, C_1, can similarly be calculated from Equations (11-3) and (11-4), from which Equation (11-7) is derived.

$$C_1 = \sqrt{A_1^2 + B_1^2} \tag{11-7}$$

Applying a least-squares model to Equation (11-2), the solution for coefficients A_0, A_1, and B_1 is given by Equation (11-8).

$$\begin{bmatrix} N & \sum\cos(2\pi ft) & \sum\sin(2\pi ft) \\ \sum\cos(2\pi ft) & \sum\cos^2(2\pi ft) & \sum\cos(2\pi ft)\sin(2\pi ft) \\ \sum\sin(2\pi ft) & \sum\cos(2\pi ft)\sin(2\pi ft) & \sum\sin^2(2\pi ft) \end{bmatrix} \begin{Bmatrix} A_0 \\ A_1 \\ B_1 \end{Bmatrix} = \begin{Bmatrix} \sum y \\ \sum y\cos(2\pi ft) \\ \sum y\sin(2\pi ft) \end{Bmatrix} \tag{11-8}$$

If the number of data points, N, is such that whole cycles can be analyzed, then Equation (11-8) may be written as Equation (11-9).

$$\begin{bmatrix} N & 0 & 0 \\ 0 & N/2 & 0 \\ 0 & 0 & N/2 \end{bmatrix} \begin{Bmatrix} A_0 \\ A_1 \\ B_1 \end{Bmatrix} = \begin{Bmatrix} \sum y \\ \sum y\cos(2\pi ft) \\ \sum y\sin(2\pi ft) \end{Bmatrix} \tag{11-9}$$

Then, coefficients A_0, A_1, and B_1 are easily given by Equations (11-10),(11-11), and (11-12) respectively.

$$A_0 = \frac{\sum y}{N} \tag{11-10}$$

$$A_1 = \frac{2}{N}\sum y\cos(2\pi ft) \tag{11-11}$$

$$B_1 = \frac{2}{N}\sum y\sin(2\pi ft) \tag{11-12}$$

Applying this methodology for tensile strain necessitates centering the stress (ε_t) so that the mean value is zero, as shown in Equation (11-13). Equations (11-6), (11-7), (11-10), (11-11), and (11-12) are then applied to the centered stress using Equations (11-13) through (11-18).

$$\sigma' = \sigma_i - \frac{\sum_{i=1}^{N}\sigma_i}{N} \tag{11-13}$$

$$A_{\sigma_0} = \frac{\sum_{i=1}^{N}\sigma_i'}{N} \tag{11-14}$$

$$A_{\sigma_1} = \frac{2}{N}\sum_{i=1}^{N}\sigma_i'\cos(2\pi ft_i) \tag{11-15}$$

$$B_{\sigma_1} = \frac{2}{N} \sum_{i=1}^{N} \sigma_i' \sin(2\pi f t_i) \tag{11-16}$$

$$\theta_\sigma = \left\{ \begin{array}{l} \tan^{-1}\left(\dfrac{-B_{\sigma_1}}{A_{\sigma_1}} \right), A_{\sigma_1} > 0 \\ \tan^{-1}\left(\dfrac{-B_{\sigma_1}}{A_{\sigma_1}} \right) + \pi, A_{\sigma_1} < 0 \end{array} \right\} \tag{11-17}$$

$$|\varepsilon_t| = \sqrt{A_{\sigma_1}^2 + B_{\sigma_1}^2} \tag{11-18}$$

The results of these equations then can be used with Equation (11-2) to verify the fitting procedure. The same methodology is used to measure the tensile stress $|\sigma_t|$.

The flexural or tensile stiffness of a beam specimen is measured as shown in Equation (11-19).

$$S = \frac{|\sigma_t|}{|\varepsilon_t|} \tag{11-19}$$

The phase angle (φ) is calculated using Equation (11-6) to yield Equation (11-20).

$$\phi = \theta_\sigma - \theta_\varepsilon \tag{11-20}$$

Appendix D. Laboratory Fabrication of Beam Specimens

Step 1. Compact the slab sample using a roller compactor.

A pneumatic steel roller compactor with a vibrator that complies with EN 12697-33 (BS EN 2019) was used to make beam specimens for this project. The slab compactor model CRT-RC2S, manufactured by James Cox and Sons and shown in Figure E- 1, was employed to perform the compaction. The compactor allows the user to select the number of passes and compaction load levels to reach the target height and thus the desired density. The metal mold provided with the compactor can make 400-mm (15.75-in.) long, 305-mm (12-in.) wide, and 100-mm (3.94-in.) tall slab samples.

Figure E- 1. Pneumatic roller compactor with vibrator (CRT-RC2S).

For this study, the CRT-RC2S compactor was used to make double-layered slabs, with each layer 50-mm (1.97-in.) thick. The compaction process was carried out in two stages. The first stage consists of bottom layer fabrication and the second stage consists of a hot asphalt tack coat application, geosynthetic placement, and top layer compaction. The two stages commence with measuring and placing the required weight of loose mix for the respective layer (top/bottom) along with batching spatulas in the oven at the compaction temperature of 145°C (293°F) for an hour. After completing the separation procedure (homogenization of the loose mix obtained from the hot mix plant), each cloth bag was found to weigh around 8.5 kg (18.7 lb). Each slab layer was estimated to require 13 kg (28.7 lb), which could vary depending upon the target air void content; hence, two cloth bags of loose mix were used. Figure E- 2 (a) shows weighing one of the cloth bags of loose mix and Figure E- 2 (b) shows two pans of loose mix in the oven.

(a) (b)

Figure E- 2. (a) Weighing loose mix in cloth bag and (2) two pans of loose mix obtained from two cloth bags in the oven at the compaction temperature (145°C).

After an hour in the oven at 145°C (293°F), the two bags of loose mix were separated into six equal parts, each around 2.1 kg (4.6 lb) spread evenly over each pan (three pans from each cloth bag are considered a set) for uniform heating. Then the six pans were placed in the oven at the mix temperature of 155°C (311°F) for an hour. The slab compaction mold, separation compartment, and necessary accessories (a spatula for spreading and plowing, the collar used during top layer compaction, etc.) were placed in the oven along with the pans. The reason to keep the batch pans at the mix temperature is that waiting to move the six pans to the compaction mold until the compaction process is completed takes nearly ten minutes. Hence, the mix temperature is selected for conditioning in order to prevent the material's temperature from cooling below the compaction temperature. Thermocouples inserted in the loose mix showed that, even though the oven was set at the mix temperature, the loose mix took around 55 minutes to reach the target temperature after batching. In essence, the loose mix should stay at the mix temperature for five minutes, thus mitigating the likelihood of aging. Figure E- 3 shows the batching procedure used for slab compaction.

(a) (b)

(c) (d)

Figure E- 3. (a) Batching the necessary quantity of loose mix into pans, (b) spreading loose mix in the pans for uniform heating, (c) batched pans, and (d) batched pans, mold, and necessary accessories in the oven at mix temperature.

After one hour at the mixing temperature, the hot mold was moved near the compactor, and 'black magic' lubricant was applied to the mold. This lubricant causes the solvent to vaporize, which can irritate the eyes and throat. Therefore, proper masks and safety glasses should be worn during this process. Figure E- 4 (a) through (j) present the steps taken immediately prior to compaction. Once the lubricant is applied, the separation compartment is placed in the middle one-third of the mold, as shown in Figure E- 4 (a), so that the loose mix can be spread evenly within the slab. The first set of three pans is placed in each compartment, followed by the second set, as shown in Figure E- 4 (b). This procedure is recommended to be performed by two persons to reduce the delay for compaction and avoid cooling the loose mix. Figure E- 4 (c) shows the heaps of loose mix in each compartment after placing the AC in the mold. Figure E- 4 (d) shows the loose mix being evenly distributed with the help of a flexible spatula. Figure E- 4 (e) and (f) respectively show the separation compartment removed from the mold and the loose mix further leveled. Figure E- 4 (g) and (h) respectively show the mix being plowed at regular intervals (1.5-in. wide) along the slab length and width using the flexible spatula. Next, an infrared heat gun is used to verify the mix temperature, as shown in Figure E- 4 (i), and the slab mold is then pushed to the compacting platform to begin the compaction process. Figure E- 4 (j) shows the slab mold loaded onto the compaction platform.

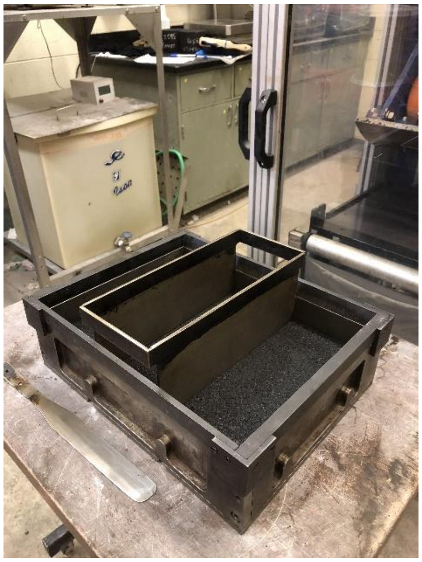

(a)

(b)

(c)

(d)

(e)

(f)

(g)

(h)

(i)

(j)

Figure E- 4. (a) Separation compartment in mold with collar, (b) pouring loose mix into each compartment, (c) heaps of loose mix in each compartment, (d) leveling the heaps in the compartment, (e) removing separation compartment, (f) leveling slab surface, (g) plowing contents of slab in length direction, (h) plowing contents of slab in width direction, (i) measuring surface temperature of loose mix before compaction using an infrared heat gun, and (j) loading mold onto compaction platform.

The initial task at the actual compaction stage is to set up the compactor, as described in Figure E- 5. This set-up is initiated immediately after the six batch pans are placed in the oven for conditioning. Figure E- 5 (a) shows the height adjustment scale in the compactor, which is set to the required height that corresponds to the thickness of the layer to be compacted. Even after setting the scale, the chances of visual errors in precision measurements are high, so relying solely on the compactor scale may lead to erroneous outcomes. Hence, as shown in Figure E- 5 (b), channel sections, 50.8 mm (1.97 in.) in height, were placed above an aluminum plate with the same thickness as that of the mold base, i.e., 10 mm (0.39 in.), with the compactor placed just above the channel. A small gap, less than a millimeter, is recommended to ensure that the compactor face is not set below the target height, which is accomplished by fine-tuning the scale lock. Figure E- 5 (c) shows the compactor face about to abut the channels.

(a) (b)

(c)

Figure E- 5. (a) Height adjustment scale in compactor, (b) channel sections set above aluminum plate for precision measurements, and (c) compactor face about to abut channels.

Six compaction levels were set according to the numerous compaction iterations that were carried out on the slab samples. Each level consisted of a certain number of cycles and applied pressure on the material. As shown in Figure E- 6, the number of cycles and the applied pressure were increased gradually to compact the slab to the target height. All the compaction cycles were performed with vibration. Once the mold, filled and leveled with the loose mix, was loaded into the compactor, the preset compaction set-up was triggered for compaction. After the compaction was completed, the slab was left at ambient temperature to cool.

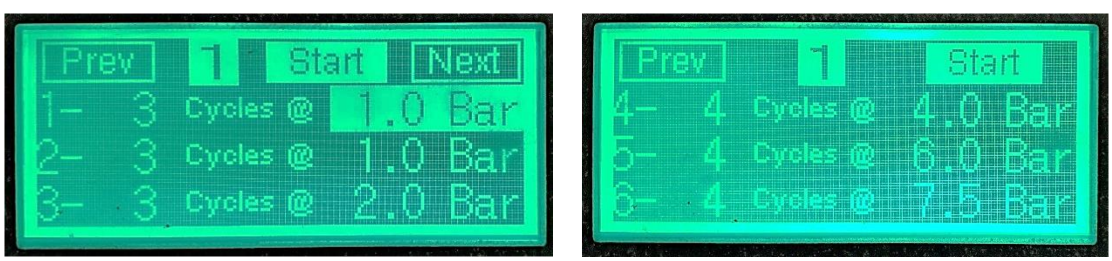

Figure E- 6. Details of each compaction level and number of cycles at respective applied pressure.

Step 2. Prepare the geosynthetic product for slab samples.

Geosynthetic products with the rectangular dimensions of 400 mm (15.7 in.) × 300 mm (11.8 in.) are required to fabricate geosynthetic-reinforced slab samples using a roller compactor. The geosynthetic products typically are unrolled in the traffic direction. Therefore, for this study, the products were cut into the rectangular dimensions such that the MD of the product matched the slab compaction direction. The geosynthetic samples were extracted diagonally within the rolled-out footprint to avoid manufacturing defects in the MD and xMD. Figure E- 7 (a) illustrates the diagonal pattern used for cutting the product. Figure E- 7 (b) shows the template tracing process over PC#2, where outlines were drawn using a template and china pencil. A cloth cutter (Reliable 1500 FR) that can cut up to 2.54-cm (1-in.) thick fabric bundles was then used to cut the geosynthetic sample shapes from the rolls. The cutter was run through the trace marks to extract the geosynthetic samples.

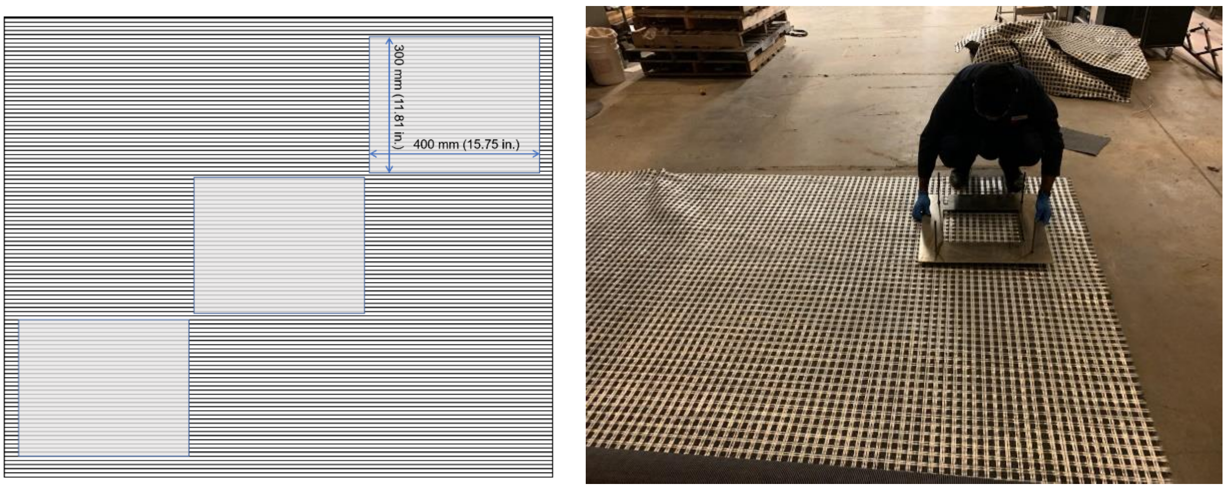

(a) (b)

Figure E- 7. (a) Template used for cutting pattern and (b) tracing the template over PC#2.

Step 3. Apply the tack coat using a hot spray gun.

A hot spray gun was used to apply tack coat on the bottom layer of a beam specimen. Tack coat application rate was controlled by measuring the weight of tack coat applied on the specimen using a scale. A spatula was used to evenly spread the tack coat on the specimen surface after the spraying. Figure E- 8 depicts (a) the laboratory test set-up and (b) applying the tack coat to a beam sample.

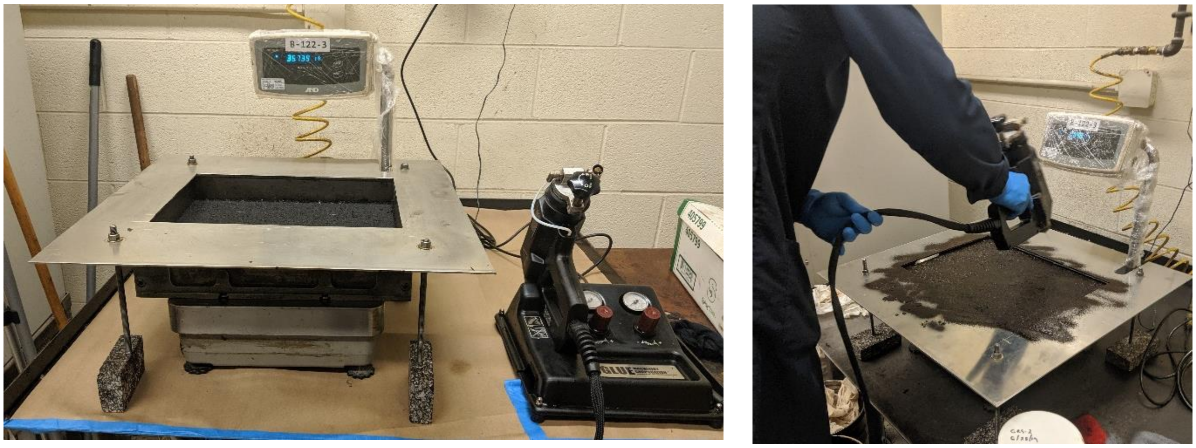

(a) (b)

Figure E- 8. (a) Tack coat application test set-up and (b) applying tack coat using hot spray gun.

Step 4. Place the geosynthetic product on the slab sample.

After applying tack coat on the bottom layer of a beam specimen, the geosynthetic product was placed as per the manufacturer's guidelines. Note that, before placing the geosynthetic, the bottom layer was heated to 145°C (293°F) for two minutes to liquify the asphalt binder so that proper impregnation of the asphalt and glue were achievable. Following the geosynthetic placement, a set pressure was applied by rolling a metal rod over the sample to ensure adequate bonding throughout the contact area (interface) between the product and bottom layer, as shown in Figure E- 9 (a) and (b) before and after placement, respectively.

(a) (b)

Figure E- 9. Placement of geosynthetic product above bottom layer: (a) before and (b) after placement.

Care was taken to ensure the same footprint of the grids among the beam specimen replicates so that the effect of different footprint of the grids on the test results could be minimized. Figure E-10 (a), (b), and (c) show the footprints that are shared between each of the paving composites, PC#1, PC#2, and PaG, respectively, and the paving grid. Even though the grid layout is oriented symmetrically over the slab's bottom layer, the grid's footprint is asymmetric with reference to the beam's plan view center. However, such an asymmetric layout is typical for replicates. Modifying the cutting pattern to obtain a symmetric grid footprint in specimen replicates invites additional labor. Therefore, the DIC capture faces for the replicate specimens were chosen in a way that those faces have the same footprint of the grids. For example, in Figure E- 10(a), the cut through the beam's center divides the strip of PC#1 grid into two halves (square-shaped individual grids are divided into two halves). Thus, the two beam faces that face away from the beam's center [64-mm (2.52-in.)] are cut along the rib in the transverse direction. Hence, the DIC camera is set to capture the beam face from the sides that are marked by the red triangles such that the grid's footprint is identical among the replicates. In Figure E- 10, the capture faces are marked by triangular markers at the faces of the beam's middle one-third portion that will be oriented towards the DIC camera.

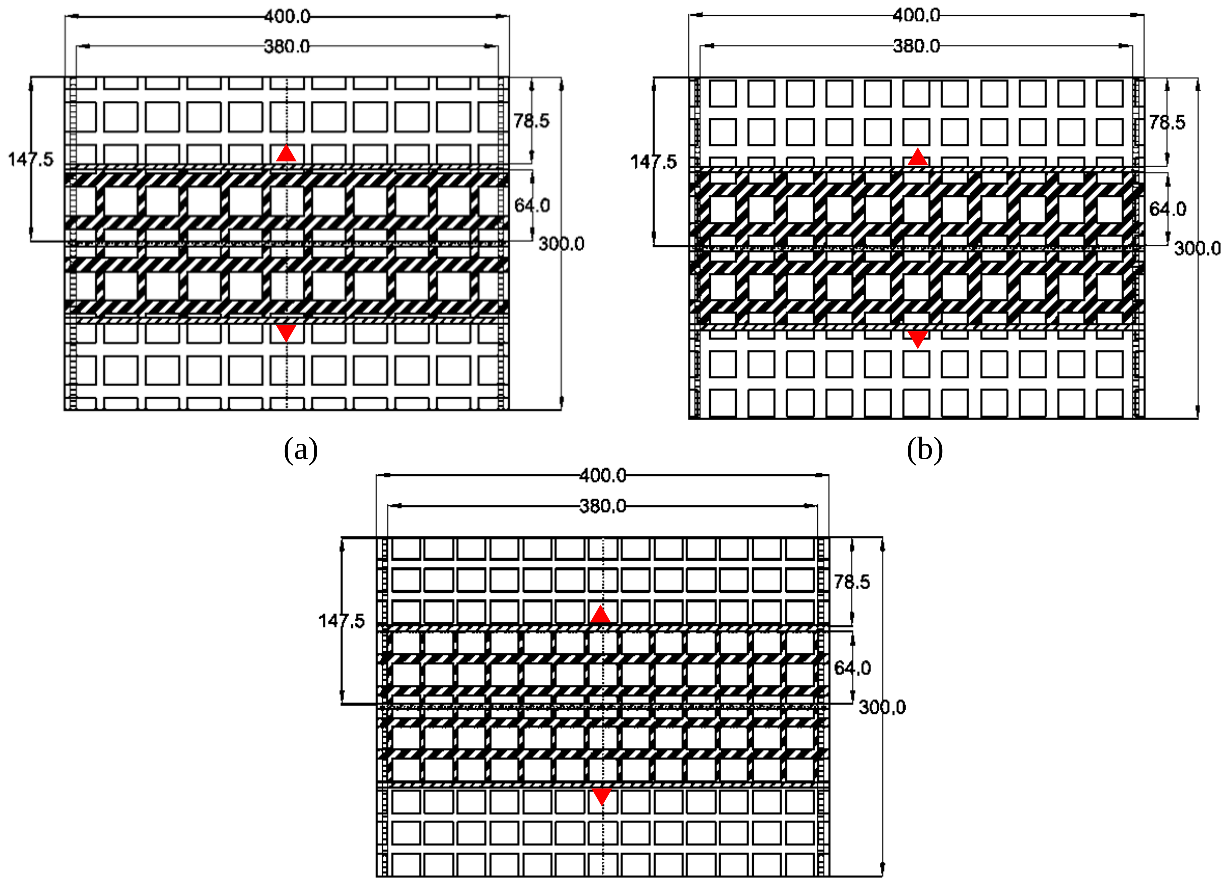

(c)

Figure E- 10. Layout pattern of grid for (a) PC#1, (b) PC#2, and (c) PaG.

Step 5. Prepare the beam specimens from slab samples.

In order to obtain beam specimens 400-mm (15.75-in.) long, 54-mm (2.12-in.) wide, and 64-mm (2.52-in.) in height, lab samples 400-mm (15.75-in.) wide to 305-mm (12-in.) long in the plan dimensions were cut into five pieces (four cuts) along the width. The outer two beam pieces were discarded to avoid the effect of the air void gradient. Figure E- 11 shows the slab-cutting process to create the beam specimens. Figure E- 11 (a) shows the slab-cutting dimensions and the slab just prior to being cut by the masonry saw. Three beam specimens were extracted from each slab and then cut from the slabs using the saw. First, beams 64-mm (2.52-in.) wide were cut out of the slab, and then the bottom and top layers of each beam were trimmed to retain thicknesses of 18 mm (0.71 in.) and 36 mm (1.42 in.), respectively, as illustrated in Figure E- 11 (b). That is, after cutting and trimming the specimens, the interlayer was located at one-third depth from the bottom of the beam.

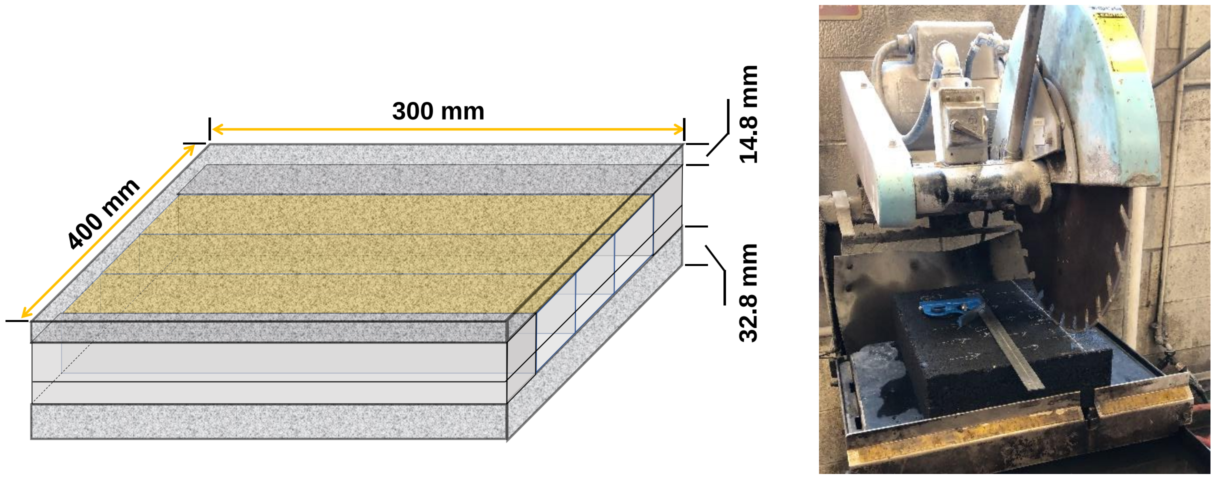

(a)

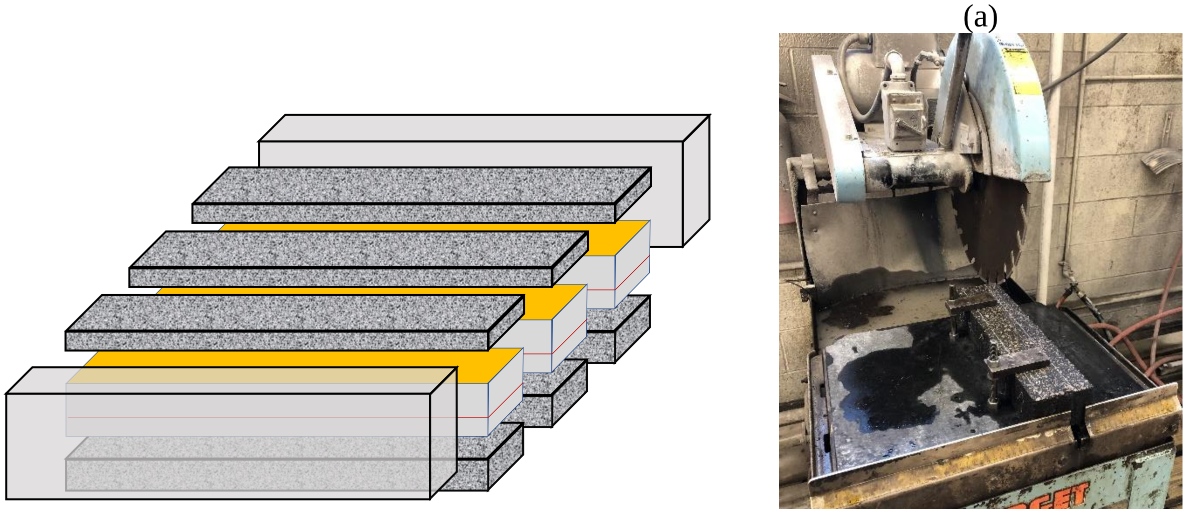

(b)

Figure E- 11. Procedure for cutting beam specimens: (a) slab dimensions and slab prior to sawing beam specimens and (b) before trimming top and bottom layers.

Step 6. Prepare the beam holding jig.

A jig to hold the beams can be used to store and transport the finished beam specimens to different laboratories and workshops. Placing a beam specimen on an uneven surface will cause creep deformation, especially if the beam has been stored for an extended period. Moreover, moving a finished beam specimen (just after cutting it from the slab) using bare hands within the different rooms in a laboratory also could cause creep deformation, and the chance of such deformation is high at elevated room temperatures (> 30°C). These uncertainties in sample handling need to be avoided and can be mitigated using the holding jig shown in Figure E- 12. The same jig can be easily mounted onto a milling machine so that no additional fasteners are required during the notch-cutting process. The research team strongly recommends using a holding jig after preparing the beam specimens until the beams are loaded into the NBFT apparatus.

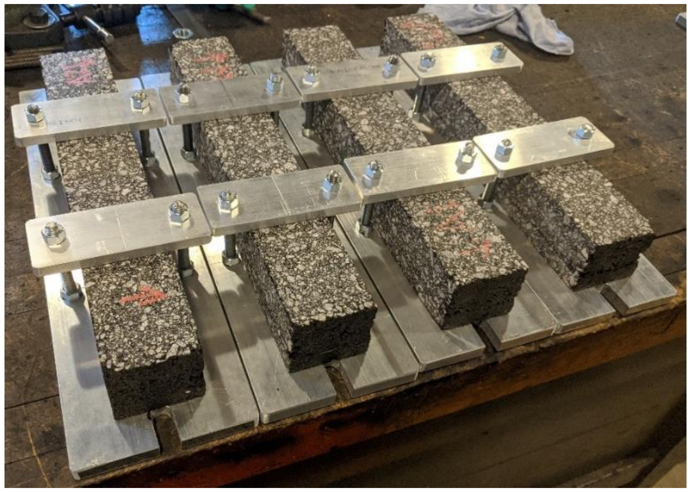

Figure E- 12. Beam specimens fastened in a holding jig.

Step 7. Cut a notch into the beam specimens.

Two methods typically are employed to make notches in AC beam specimens. The first method is to place a metal insert inside the compaction mold and the second method is to create a mechanical notch cut. The former method affects the mixture compaction effort by disturbing the aggregate alignment, thus leading to mixture segregation. The mechanical method results in a blunt notch compared to the sharper notch obtained using a metal insert. An alternative approach is to produce a well-defined pre-crack by applying a small cycle load. Previous studies of notched AC specimens (disk-shaped compacted specimens, single-edge notched beams) have led researchers to recommend a pre-crack or sharp notch on the specimen to eliminate the effects of different notch sizes for different specimens (Kuai et al. 2010; Petersen et al. 2005).

In the case of a single-edge notched beam, a mechanical notch to a depth ratio (a/W) of 0.19 is recommended over the standardized fracture test requirement of the a/W ratio between 0.45 and 0.55. However, using deep-notched specimens made with AC may produce undesirable test results, such as large statistical variations and crack initiation under self-weight (Petersen et al. 2005; Sudarsanan et al. 2019). For notched disk-shaped compacted specimens, a notch length of 27.5 mm serves as a pre-crack and is preloaded until the initial crack length reaches 30 mm (Kuai et al. 2010). Wargo (2015) recommends the use of stiff notching saw to produce repeatable notches, as any flexibility of the saw could cause a variation in notch depth.

The recommended two steps needed to create a sharp notch make the procedure cumbersome. The first cut involves making a notch using a 5-mm wide blade to create a half-notch depth, followed by a 1-mm wide blade to make a full-notch depth. Inducing a well-defined pre-crack is possible for the current study but requires additional measurement gauges to develop an accurate crack. Therefore, a tapered notch could help the stress concentration and improve the likelihood that the crack will initiate from the same point. In order to make a consistent notch that could produce repeatable results, a drill was chosen as the tool in this study. Figure E- 13 shows two sizes of drill bits and Table E- 1 presents details regarding the drill bits that were used to make consistent notches.

Figure E- 13. Drill bits used for making tapered notches.

Table E- 1. Material and Dimensions of Drill Bits Used for Current Study

Finish		Titanium aluminum nitride (TiAlN) -coated
Material		Carbide
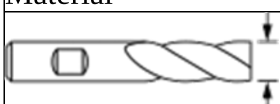	Mill diameter	2.381 – 23.8 mm (3/32 – 0.937 in.)
	Mill diameter tolerance	-0.003 in. to 0.000 in.
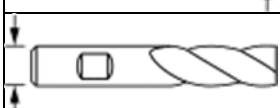	Shank type	Straight
	Shank diameter	3.175 mm (1/8 in.)
Length of Cut		9.525 mm (3/8 in.)
Overall Length		38.1 mm (1 1/2 in.)
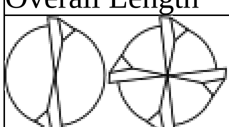	Flute Type	Spiral
	Number of Flutes	2 or 4
	Flute Spacing	Equal
Point Angle		90°
Helix Angle		30°

Figure E- 14 presents images of the tapered notches cut into the beam specimens used in the notch study. Three equidistant deep drilling steps achieved the desired notch depth of 5 mm. Two approaches were followed for drilling. The first approach allowed the unidirectional movement of the drill along the width of the beam specimen during each depth step. Figure E- 14

(a) and (b) show that the aggregate chipped near the edge of the beam during the process. This outcome is common at the edges where the drill bit exits the beam. However, such chipping was not evident when the drill bit entered the beam specimen. Therefore, the second approach was adopted whereby the drill bit enters the beam from one edge, and drilling is stopped when the bit reaches the middle of the beam. The drill bit then is repositioned on the other edge, and drilling commences to reach the center of the beam to conclude each depth step. This method significantly reduced the problem of chipping the aggregate. However, the problem persisted when large aggregate particles were present at the edges. Nonetheless, a tapered notch was sustained throughout the width of the beam, and chipping was found only at the edges. In short, a careful procedure is needed to produce consistent tapered notches. This process is more time-consuming than saw cutting: 30 minutes using a drill versus 30 seconds using a saw.

(a) (b) (c)

Figure E- 14. Tapered notches made by drilling: (a) and (b) chipped edges under a unidirectional pass, and (c) non-chipped edge under a bidirectional pass.

Step 8. Speckle the beam specimen for DIC testing.

In order to track the crack propagation through a beam specimen using the DIC technique, the surface of the beam specimen should be speckled. The speckling procedure allows the surface to have sufficient contrast throughout the area of interest so that consistently sized speckle subsets may be tracked with certainty. Therefore, the certainty of the results is often defined by the quality of the speckle pattern.

A new speckle kit was procured for this study to obtain a consistent speckle pattern. Different sizes of speckle/dot sizes could be selected depending on the region of interest. Table E- 2 shows the different roller sizes that can be selected depending on the camera used and the region of interest. Based on Table E- 2, the dot sizes of 0.007 in. and 0.013 in. could work for the beam specimen’s field-of-view. Typically, the smaller of the two provides better resolution. Figure E-15 shows the roller stamp used for speckling the beam specimens.

Table E- 2. Dot Size Selection Table for Speckling Process in DIC Testing.

Camera / Dot size	Field-of-View 0.007" (0.18 mm)	0.013 in. (0.33 mm)	0.026 in. (0.66 mm)	0.05 in. (1.27 mm)	0.10 in. (2.54 mm)	0.20 in. (5.08 mm)
1 MP camera 1024 pixels across	0.9 in. - 2.4 in. 2.3 - 6.1 cm	1.7 in. - 4.4 in. 4.2 - 11 cm	3.3 in. - 8.9 in. 8.4 - 23 cm	6.4 in. - 17.1 in. 16 - 43 cm	12.8 in. - 34.1 in. 33 - 87 cm	26.6 in. - 68.3 in. 65 - 173 cm
2.3 MP camera 1920 pixels across	1.7 in. - 4.5 in. 4.3 - 11 cm	3.1 in. - 8.3 in. 7.9 - 21 cm	6.2 in. - 16.6 in. 16 - 42 cm	12.0 in. - 32.0 in. 31 - 81 cm	24.0 in. - 64.0 in. 61 - 163 cm	48.0 in. - 128.0 in. 122 - 325 cm
5 MP camera 2448 pixels across	2.1 in. - 5.7 in. 5.4 - 15 cm	4.0 in. - 10.6 in. 10 - 27 cm	8.0 in. - 21.2 in. 20 - 54 cm	15.3 in. - 40.8 in. 39 - 103 cm	30.6 in. - 81.6 in. 78 - 207 cm	61.2 in. - 163.2 in. 155 - 415 cm
16 MP camera 4872 pixels across	4.3 in. - 11.4 in. 11 - 29 cm	7.9 in. - 21.1 in. 20 - 54 cm	15.8 in. - 42.2 in. 40 - 107 cm	30.5 in. - 81.2 in. 77 - 206 cm	60.9 in. - 162.4 in. 155 - 413 cm	121.8 in. - 324.8 in. 309 - 825 cm

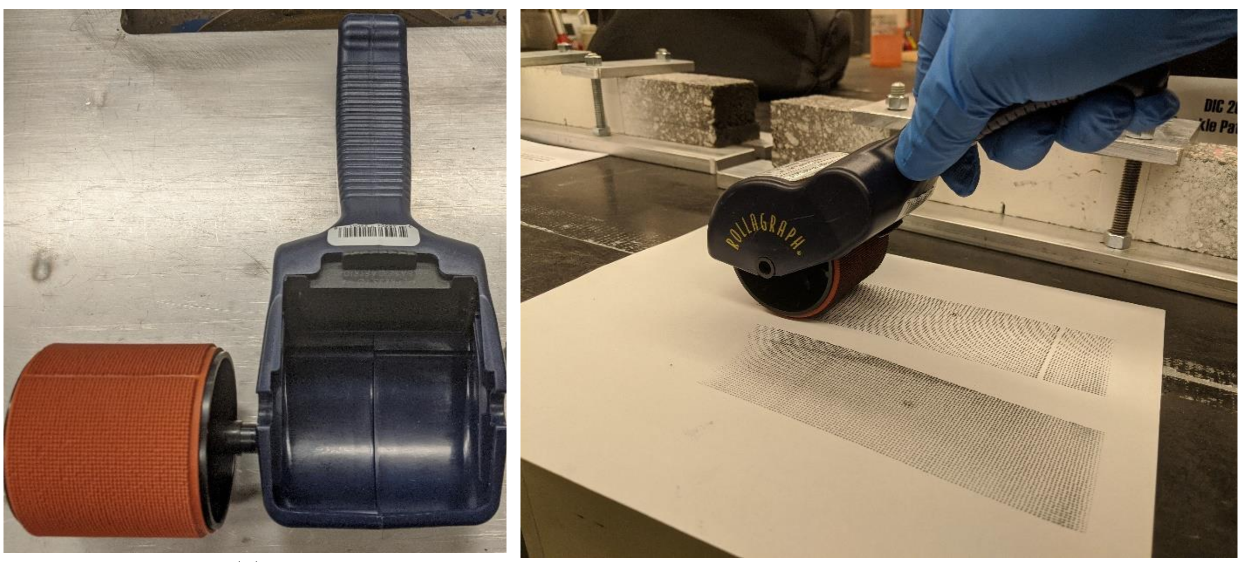

(a) (b)

Figure E- 15. (a) Components of roller stamp and (b) using roller stamp for speckling.

Figure E- 16 depicts the procedure for speckling the beam specimens. The first step is to apply a base coat of paint on the beam specimen, as shown in Figure E- 16 (a). The purpose of the base coat is to create as much contrast as possible. Speckle patterns may have a white base coat and black speckles. For the roller stamps, black ink is used, so the base coat must be white. When using stamps, the paint must be dry to the touch. Typically, about five to ten minutes is sufficient for drying to the touch. A Krylon chalky finish matte clear spray paint was used as the base coat in this study. Figure E- 16 (b) shows the different speckle patterns on beam specimens.

(a)

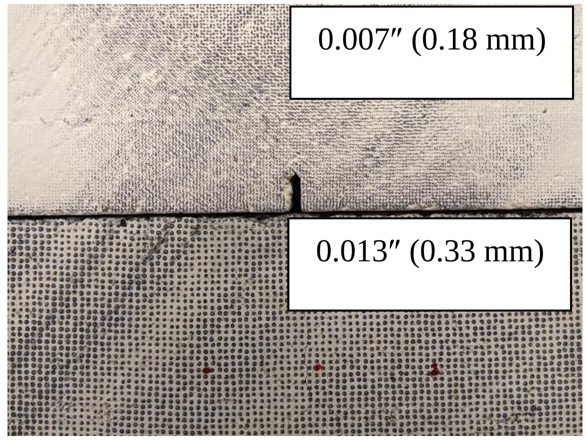

(b)

Figure E- 16. (a) Spraying the base coat on a beam specimen and (b) speckle patterns with different dot sizes on beam specimens.